



TECHNISCHE
UNIVERSITÄT
WIEN
Vienna University of Technology

DIPLOMARBEIT

Electronic correlations at the two-particle level

ausgeführt am Institut für
Festkörperphysik
der Technischen Universität Wien

unter Anleitung von
Privatdoz. Dr. Alessandro Toschi
Projektass.(FWF) Dipl.-Ing. Georg Rohringer

durch
Thomas Schäfer, BSc.

Missongasse 9
A-3550 Langenlois

Ort, Datum

Unterschrift

Abstract

The theoretical analysis of two-particle quantities for correlated electron systems is a valuable task. Not only can one compare some of these quantities directly to a large number of experiments (from optical to neutron and Raman spectroscopy), but they also serve as essential inputs for diagrammatic extension of one of the most famous method for studying the physics of correlated materials, i.e. the dynamical mean field theory (DMFT), such as the dynamical vertex approximation (D Γ A) and the dual fermion approach. Hitherto, two-particle vertex quantities have been investigated rather sporadically in the literature and very often approximated by the value of the bare interaction. This thesis aims at filling this gap, providing a systematic analysis, in which the investigation of both local and non-local vertices is conducted and has lead to particularly interesting, and, in some sense, surprising results.

In the first part of this thesis, the context of contemporary many body quantum mechanics is recalled and the notion of (electronic) correlations is illustrated (chapter 1). Chapter 2 gives a brief introduction in the methods of many body quantum theory for describing strongly correlated electron systems, particularly one- and two-particle Green functions, as well as DMFT and its extensions. The numerical results for the purely local and the momentum dependent vertex functions are presented and interpreted in chapters 3 and 4 respectively and conclusions are drawn and an outlook to future research is given in chapter 5.

Deutsche Kurzfassung

Die Analyse von Zweiteilchengrößen ist von großer Bedeutung für die moderne Festkörperphysik. Dafür gibt es im Wesentlichen zwei Gründe: zum Einen können theoretisch (also numerisch oder analytisch) berechnete Zweiteilchengrößen meist direkt mit einer großen Zahl an experimentellen Daten verglichen werden (beispielsweise Ergebnisse von optischer, Neutronen- oder Raman-spektroskopie), zum Anderen sind sie essentielle Größen für diagrammatische Erweiterungen der dynamischen Molekularfeldnäherung (dynamical mean field theory, DMFT), eine der erfolgreichsten Näherungsmethoden zur Beschreibung von stark korrelierten Elektronensystemen. Zu nennen wären hier die dynamische Vertexapproximation (D Γ A) oder der Dual Fermion Ansatz. Da eine Analyse dieser wichtigen Zweiteilchengrößen in der Literatur nur sehr sporadisch (beispielsweise nur für bestimmte Parameterwerte) durchgeführt wurde, versucht die vorliegende Diplomarbeit mit einer systematischen Untersuchung von sowohl lokalen als auch nicht-lokalen Zweiteilchengrößen - die teilweise unerwartete und erstaunliche Ergebnisse an den Tag legt - diese Lücke zu schließen.

Der erste Teil dieser Diplomarbeit ist einer Einführung in das Gebiet der modernen Vielteilchentheorie gewidmet, in deren Rahmen auch der Begriff der Korrelationen erläutert wird (Kapitel 1). Nach einer Zusammenfassung von bekannten Theorien und Methoden zur Behandlung von stark korrelierten Elektronensystemen (Kapitel 2) werden Ergebnisse für lokale (Kapitel 3) und nicht-lokale Zweiteilchengrößen (Kapitel 4) vorgestellt und analysiert. Die Arbeit

iv

schließt mit Schlussfolgerungen aus den Ergebnissen und Perspektiven für künftige Forschungsprojekte zu diesem Thema in Kapitel 5.

Dedication and acknowledgements

A huge amount of people played an important role for making my studies (and, in most of the cases, not only that) a success. The biggest thanks I want to give to my parents, who always supported me unboundedly with their time, their advice and, as well, financially and I do not know what I shall give them in return, that could really appreciate what they did for me. I also want to thank Katharina, whose presence is so important to me and which I enjoy more and more everyday. I am blessed, I have met you! Thanks also to Manfred Stiglitz, without whom the analogy of correlations and Viennese Waltz would not ever have come to my mind.

Luckily, both for my personal and scientific development, I got to know my current supervisor for this thesis, Alessandro Toschi, whose permanent advise and support made writing this thesis not only a success but also a lot of fun (I will definitely revisit Rome, I promise!). Furthermore, I want to thank Karsten Held for his scientific advice and the warm welcome in his working group. A big "thank you" also goes to Giorgio Sangiovanni (I will never forget l'enobottega Vincanta), Joachim Burgdörfer and Iva Brezinova, in whose group I had the honour of writing the most physical of my three project works and Joao Pela, with whom I had the privilege to work at CERN. Also I want to thank Olle Gunnarsson, whose code was the basis of this thesis and who kindly invited me to the Max-Planck institute in Stuttgart and Sergio Ciuchi for insightful discussions. Last, but not least, I want to thank Georg Rohringer for many inspiring discussions and his strong support. A lot of the results in this thesis depend on the work previously conducted by him.

I acknowledge financial support from the Austrian Science Fund (FWF). The numerical calculations have been performed on the MZ4 cluster at the Max-Planck institute for solid state research in Stuttgart and the HCLM cluster in Vienna.

Hoping, that I have not forgotten anyone, I am really looking forward to many years of high-quality scientific research and, hence, a lot of fun.

Contents

Title page	i
Abstract	iii
Dedication and acknowledgements	v
Table of contents	vii
1 Introduction: What is electronic correlation?	1
1.1 The physics of many particle systems	1
1.2 Correlations in physics and in life	3
1.2.1 An example in every day's life: the ballroom dancer	3
1.2.2 Correlation in the solid state: fascinating but challenging physics	4
1.3 From the full many body Hamiltonian to the Hubbard model	6
2 Theory and methods: from the one-particle propagator to the fully irreducible vertex	11
2.1 Many-body Green function: the one-particle propagator	12
2.1.1 Definition of the Green function	12
2.1.2 Reducibility at the one-particle level: the self-energy	14
2.1.3 Breakdown of perturbation theory	17
2.2 The dynamical mean field theory (DMFT)	17
2.2.1 The diagrammatic content of DMFT	18
2.2.2 Self-consistency cycle and impurity solvers	18
2.2.3 Successes and limitations of the DMFT	22
2.3 Going beyond DMFT	23
2.3.1 Cluster extensions of DMFT	23
2.3.2 Diagrammatic extensions of DMFT	25
2.3.3 Two-particle quantities: crucial ingredients	26
2.4 Two-particle quantities	26
2.4.1 The two-particle Green function and the generalized susceptibility	26
2.4.2 Reducibility at the two-particle level and the Parquet equation	28
2.4.3 The Bethe-Salpeter equation	28
2.4.4 Spin-dependence of the two-particle quantities	29
2.4.5 Approximations at different vertex levels	30

3	Results: Local two-particle vertex functions in DMFT	33
3.1	Frequency dependencies of the local two-particle quantities: DMFT results	33
3.1.1	Literature results in exact diagonalization	34
3.1.2	Comparison of ED and QMC results	37
3.2	Divergencies of the local irreducible vertices and their physical interpretation	40
3.2.1	Divergencies of the vertex at the Mott-transition	40
3.2.2	Divergencies in the metallic phase	41
3.2.3	Phase diagram	44
3.3	Possible interpretations	46
3.3.1	The atomic limit	46
3.3.2	NRG calculations for zero temperature and kinks in the specific heat	49
3.3.3	Coherent potential approximation for the Falicov-Kimball model	50
3.3.4	A link to non-equilibrium properties of the Hubbard model	51
3.4	Summary of the local results	52
4	Results: Dynamical cluster approximation for the vertex functions	55
4.1	An existing DCA calculation of vertex quantities	56
4.2	Perturbation theory	57
4.2.1	Perturbation theory for the full vertex	58
4.2.2	Perturbation theory for the irreducible vertices	59
4.2.3	Perturbation theory for the fully irreducible vertex	60
4.3	Momentum dependence of two-particle quantities	61
4.3.1	Weak coupling regime and comparison with perturbation theory	62
4.3.2	Intermediate coupling regime and comparison with DMFT	65
4.4	Summary of the non-local results	69
5	Conclusions and outlook	71
	List of Figures	73
	List of Tables	75
	Bibliography	77
	Index	83

Chapter 1

Introduction: What is electronic correlation?

"The whole is greater than the sum of the parts."
- Aristotle

In this chapter, an introduction to one of the most fascinating topics in contemporary physics is presented: the quantum mechanics of many particle systems and, specifically, of electronic correlations. In section 1.1 the relevance of some of the most fascinating phenomena to many particle physics is briefly recalled, in section 1.2 the notion of electronic correlations is introduced and illustrated by an example from every day's life and in section 1.3 one of the most basic and famous models for the description of electronic correlations, i.e. the Hubbard model, is introduced.

1.1 The physics of many particle systems

The typical path followed by natural scientists is to unravel the elementary laws of their discipline and deduct or predict every behaviour and evolution of the phenomena they are interested in. Significant examples of this deductive method and its building bricks or "microscopic" laws can be found in every discipline. As a mere example, one may just recall

- the equations of the fundamental interactions of the standard model in physics,
- the deoxyribonucleic acid (DNA) in biology,
- the senses, emotions and cerebration in psychology.

This attitude of natural scientists is expressed fabulously in two famous German literary lines

*"Dass ich erkenne, was die Welt
Im Innersten zusammenhält"*

- Goethe, Faust - Der Tragödie erster Teil

However, such a fundamental description of a given scientific discipline by means of elementary governing laws may sometimes seem to be, at the first glance, inconsistent with the observed complex and often still unpredictable behaviour of “real”¹ systems. For instance, understanding the second law of thermodynamics, which governs much of the behaviour of physically macroscopic systems, on a microscopic level is not at all trivial and still stimulates hot debates among physicists nowadays [1]. More generally, this challenging approach of natural sciences can be summarized in the following, thrilling question that immediately arises:

What new principles and laws emerge as we make the journey from the microscopic to the macroscopic? [2]

In fact, each stage of the path connecting the microscopic and the macroscopic cosmos is paved by entirely new concepts and laws. Their understanding is crucial for the description of what one really observes at the (macroscopic) level, among which **emergent phenomena** that are non-trivial, complex results of elementary fundamental interactions of the constituents of the system, stand out.

The fascinating travel towards the understanding of the macroscopic complexities has been brilliantly described by P. W. Anderson in his article “More is different” [3]:

“The behaviour of large and complex aggregations of elementary particles, it turns out, is not to be understood in terms of a simple extrapolation of the properties of a few particles. Instead, at each level of complexity entirely new properties appear, and the understanding of the new behaviours requires research which I think is as fundamental in its nature as any other.” - P. W. Anderson

In other words: even if one could establish a “theory of everything“, including all known fundamental interactions and constituents of matter, the mission of describing every single phenomenon of the universe would still be far from being accomplished. The ultimate goal would be, instead, an accurate description at every stage between microscopic and macroscopic.

Exactly this situation is the cause why (even non-relativistic) many body quantum mechanics in solid state physics holds that fascinating phenomena. The basic building blocks here are the **Coulomb interaction** and the fundamental constituents in form of **electrons** and **protons**. Out of these ingredients (and the basic laws of quantum mechanics, of course), non-trivial, fascinating and, in most cases, completely unexpected phenomena emerge in condensed matter physics, among which one may recall

- the Mott metal-insulator transition (MIT) in vanadates [4, 5, 6],
- the high-temperature superconductivity in cuprates [7] and iron-pnictides [8],
- the formation of quantum critical points in heavy fermion compounds [9, 10] and

¹specifically in physics the suitable expression would be “macroscopic” or “complex”

- the colossal magnetoresistance in the manganites [11, 12].

Quite remarkably, some of the most fascinating and, at present, still not understood physics is found in a special class of systems, namely the class of **strongly correlated electron systems**. In view of this, in the next section the notion of correlation will be explicitly introduced and illustrated with examples coming from physics and "real life"².

1.2 Correlations in physics and in life

The term "correlation" stems from Latin "cum + relatio" and describes the situation in which two (or more) objects are in relationship with each other. Mathematically the fact that two observables A and B are correlated with each other is reflected in the the expectation value of their product:

$$\langle AB \rangle \neq \langle A \rangle \langle B \rangle \quad (1.1)$$

which, in the correlated case, cannot be trivially decomposed into a product of expectation values of the two observables separately. Hence, correlation is the summation of all effects that are not described by factorization (i.e. mean field) approximations. Before describing the application of this concept in physics and specifically to the condensed matter problems which are investigated in this thesis, to gain further insight in the meaning of what correlation really is, one may take a step into real life and discuss correlations on the parquet floor.

1.2.1 An example in every day's life: the ballroom dancer

Who does not know the following situation: after you have practised several months the Viennese Waltz in dancing school you want to take out the woman of your choice to the university's ball. However, while in the dancing school's practice, there where only three to four couples beside you on the floor, the situation with which you are confronted at the ball will be quite different as depicted in Fig. 1.1. Naturally, if you are an experienced dancer, you will not move without taking into account the movement of the other couples which are also dancing at the same time on the same floor. The technical term for this situation is **spatial correlation** among the dancing couples. In particular, if the floor is occupied that much, the interaction between the couples increases dramatically and, correctly taking into account all spatial correlations becomes essential for retrieving a good result (i.e. no bruises). Furthermore, if you keep in mind that the technique of dancing the Viennese waltz, which is danced in three-four time (i.e. 123 123), requires rising at 1 and lowering at 3³ you and all other dancers are bound to the music (the "clock" of your system). Hence, evidently, there also exists a **time correlation**. Of course, the situation gets more and more complicated if more couples are joining the dance from the sides of the ballroom (in fact, in the spirit of the physics that will be described in section 1.3, you can view these couples at the sides as an **auxiliary bath** and the probability of joining or leaving the dance floor the **hopping amplitude**). Even more

²"real life" emerges from physics, but in a non-trivial way

³actually, the timing and technique of the Viennese Waltz is much more subtle than that, but this example of correlations should be illustrative for physics' purposes



Figure 1.1: Correlation of the movements of ballroom dancers at the ball of the University of Technology in Vienna's Hofburg. No measurement of the positions of the couples can be considered as independent from the movement of the rest (taken from [13]).

dramatically, a **repelling principle** is also active, preventing the dancers from occupying exactly the same position on the floor, or at least the lady who wears the same ballroom dress (or **quantum number**) as your woman of choice from joining the dance (in physics the - less dangerous - situation corresponds to the **Pauli principle**).

1.2.2 Correlation in the solid state: fascinating but challenging physics

Although the example of correlation of ballroom dancers is quite intriguing, this is obviously not the actual motivation why physicists (and particularly solid state physicists) put so much effort in describing and understanding correlation effects. Generally speaking, situations of high electron correlation occur in systems whose electrons are obliged to reside in very narrow orbitals. This usually happens for materials containing elements with partially filled narrow orbitals, e.g. $3d$ - or $4f$ -orbitals, as it is the case for transition metal oxides or lanthanides. The reason why these orbitals are particularly narrow is, that for an orbital with fixed angular momentum l there do not exist other orbitals with the same angular momentum with lower radial quantum number n . This orbital is orthogonal to all the other ones due to the angular momentum part of its wave function. So the radial part of its wave function does not need to have any node localizing the corresponding electron much closer to the atomic ion with respect to the other orbitals [14, 15].

One of the most famous examples of the behaviours that emerge out of electronic correlations is the Mott-Hubbard metal-insulator transition.

The Mott-Hubbard metal-insulator transition

Many materials, such as V_2O_3 , exhibit a transition from the insulating to the metallic state if pressure is applied or the system is doped [5, 6, 16] (see Fig. 1.2). In V_2O_3 one can track down this behaviour to correlation effects stemming

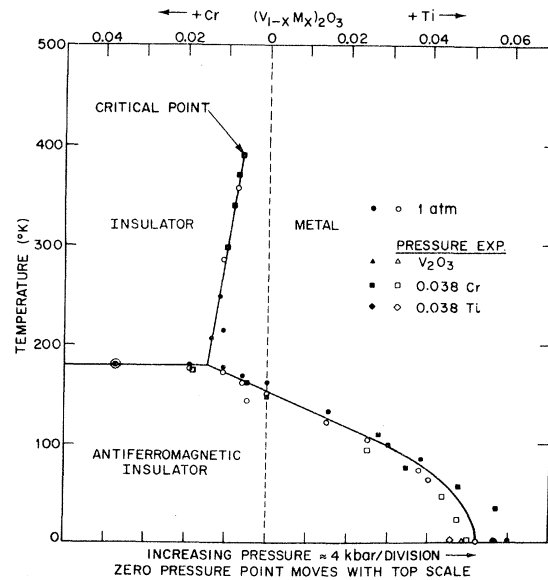


Figure 1.2: Mott metal-insulator transition in V_2O_3 . Although, according to band theory considerations, these materials should always be metals, the system presents a transition from an insulating to a metallic phase when pressure is applied or the doping level with Cr is changed (taken from [5]).

from the mutual electron-electron interactions among the $3d - t_{2g}$ electrons of the partially filled outer shell of V . If one considers a half-filled lattice, the reason why it undergoes a MIT is, that for very strong on-site interaction between the electrons the situation that two electrons occupy exactly the same lattice site becomes energetically too expensive since the movement of the electron, naturally, generates a given amount of double occupancies for a high enough value of the local Coulomb or Hubbard interaction (see section 1.3). The system is driven into an insulating state, even if according to the band theory it should be a metal. This kind of transition is called **Mott-Hubbard transition** (MIT, [4, 16]).

In DMFT (see section 2.2) one can calculate the phase diagram of the two-dimensional Hubbard model in the sense of determining the metallic and insulating regions in the temperature vs. interaction plane (T/U -plane). Fig. 1.3 shows this MIT phase diagram from [17]. One can note that there is a coexistence region of both metallic and insulating solution between the interaction values U_{c1} and U_{c2} . The coexistence region, which is the numerical hallmark for a first-order transition, vanishes at a critical end point at a finite temperature,

which is the lower tip of a crossover region, where a smooth and continuous change of the physical properties is found by increasing U . Note that this situation closely recalls the well-known one of the liquid-gas transition.

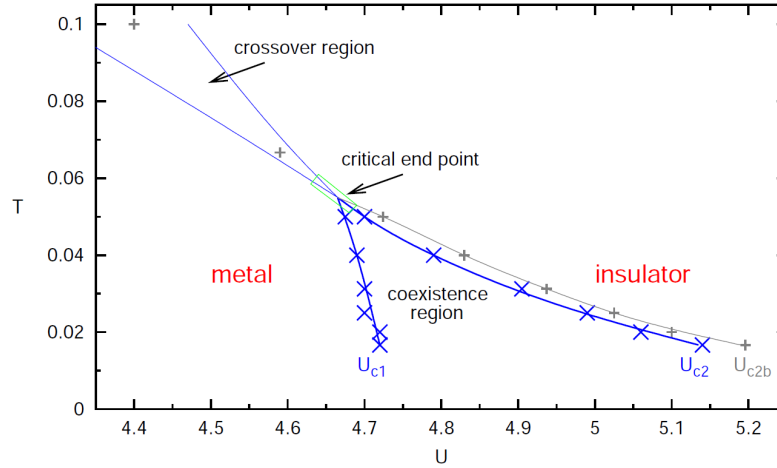


Figure 1.3: DMFT phase diagram (taken from [17]) showing the MIT of the two-dimensional half-filled Hubbard model. One can note that there is a coexistence region of both metallic and insulating solution between the interaction values U_{c1} and U_{c2} . The coexistence region vanishes at a critical end point at a finite temperature, which is the lower tip of a crossover region.

The full treatment of electronic correlations for realistic systems still represents a difficult task. Hence, it is often worth to break those systems down to model systems. One of the most famous model Hamiltonians will be considered in the next section.

1.3 From the full many body Hamiltonian to the Hubbard model

In solid state theory it is actually quite easy to write down a general Hamiltonian which contains the only relevant fundamental interaction (i.e. the Coulomb interaction) in the non-relativistic limit in its second quantized form:

$$H = H_0 + V_{ee} \quad (1.2)$$

with

$$H_0 = \sum_{\sigma=(\uparrow,\downarrow)} \int d^3r \Psi_{\sigma}^{\dagger}(\vec{r}) \left[-\frac{\hbar^2}{2m} \partial^2 - \sum_l \frac{e^2}{4\pi\epsilon_0} \frac{Z_l}{|\vec{r} - \vec{R}_l|} \right] \Psi_{\sigma}(\vec{r})$$

$$V_{ee} = \frac{1}{2} \sum_{\sigma,\sigma'} \int d^3r d^3r' \Psi_{\sigma}^{\dagger}(\vec{r}) \Psi_{\sigma'}^{\dagger}(\vec{r}') \frac{e^2}{4\pi\epsilon_0} \frac{1}{|\vec{r} - \vec{r}'|} \Psi_{\sigma'}(\vec{r}') \Psi_{\sigma}(\vec{r})$$

where $\Psi_{\sigma}^{\dagger}(\vec{r})$ and $\Psi_{\sigma}(\vec{r})$ are field operators which create or respectively destroy an electron of charge $-e$ and spin σ at position \vec{r} and l are the lattice ions with charge Z_l at the positions \vec{R}_l . The electron's mass is denoted by m , \hbar is the Planck constant and ϵ_0 is the dielectric constant in vacuum. However, it is impossible to solve this problem in its whole generality. The situation is Janus-faced: On the one hand, in solid state physics one usually has to deal with problems which involve a number of particles which is of the order of the Avogadro constant $N_A \approx 10^{23}$. On the other hand, in many situations, for interpreting (or predicting) the experimental results, it is not necessary to calculate the general solution to this problem (i.e. the wave function for the $\approx 10^{23}$ particle problem). One way retrieving valuable informations about the system and, at the same time, at least approximately, explaining and predicting experimental results is paved by simplifying Eq. 1.2 in order to build up **model Hamiltonians** and treat them with **functional methods** (see chapter 2).

If one considers a lattice of ions which are separated by a distance larger than the Bohr radius, a good approximation for this class of systems is the **tight-binding approximation** (see e.g. [18]). In a first step the Hamiltonian is represented by a superposition of atomic orbital states or **Wannier states**. Those Wannier states constitute an orthonormal basis of the one-particle Hilbert space, meaning that there exists a (unitary) transformation from real to Wannier space. This implies that the field operators in real space in 1.2 can be written in terms of field operators at each lattice site i :

$$\Psi_{\sigma}^{\dagger}(\vec{r}) = \sum_{i=1}^N \psi_{\vec{R}_i}^*(\vec{r}) c_{i\sigma}^{\dagger} \quad (1.3)$$

Furthermore one can Fourier transform the Wannier state operators $c_{i\sigma}^{\dagger}$ to momentum space

$$c_{k\sigma}^{\dagger} = \frac{1}{\sqrt{N}} \sum_{i=1}^N e^{i\vec{k}\cdot\vec{R}_i} c_{i\sigma}^{\dagger} \quad (1.4)$$

so that the single particle part of the Hamiltonian in Eq. 1.2 becomes (see [18])

$$H_0 = \sum_{\vec{k}} \epsilon_k c_{k\sigma}^{\dagger} c_{k\sigma} = \sum_{ii'} t_{ii'} c_{i\sigma}^{\dagger} c_{i'\sigma} \quad (1.5)$$

where

$$t_{ii'} = \frac{1}{N} \sum_{\vec{k}} e^{i\vec{k}(\vec{R}_i - \vec{R}_{i'})} \epsilon_k = \int d^d r \psi_{\vec{R}_i}^* \frac{\hbar^2 \partial^2}{2m} \psi_{\vec{R}_j}$$

denotes the **hopping amplitude** for a particle to transit from site i to site i' . Similarly one can apply this procedure to the electron-electron interaction term in Eq. 1.2 and finally obtains for the fully transformed Hamiltonian:

$$H = \sum_{ii'} t_{ii'} c_{i\sigma}^\dagger c_{i'\sigma} + \sum_{ii'jj'} U_{ii'jj'} c_{i\sigma}^\dagger c_{i'\sigma}^\dagger c_{j\sigma} c_{j'\sigma} \quad (1.6)$$

If the overlap of neighbouring orbitals becomes weak, the dominant electronic interaction is the on-site Coulomb interaction, or **Hubbard interaction**. In this limit one finally arrives at the simplest model for the description of electronic correlation in solid state physics, i.e. the **Hubbard model** [19, 20, 21]. For the single band case (and only considering nearest neighbour hopping), the Hamiltonian of the Hubbard model reads

$$H = -t \sum_{(i,j),\sigma} c_{i,\sigma}^\dagger c_{j,\sigma} + U \sum_{i=1}^N n_{i\uparrow} n_{i\downarrow} \quad (1.7)$$

where $-t$ is the hopping amplitude of the electron to hop from lattice site i to j , $c_{i,\sigma}^\dagger$ and $c_{j,\sigma}$ are the creation and annihilation operators for creating or destroying an electron with spin σ on site i or j respectively, N is the number of lattice sites and (i,j) denote nearest neighbour sites. The Coulomb energy (or Hubbard interaction) U has to be paid whenever a single site is occupied by two electrons. The interpretation of the two ingredients of this model is quite transparent as they correspond to the two competing energy scales of a correlated electron system, i.e. the kinetic and the potential energy.

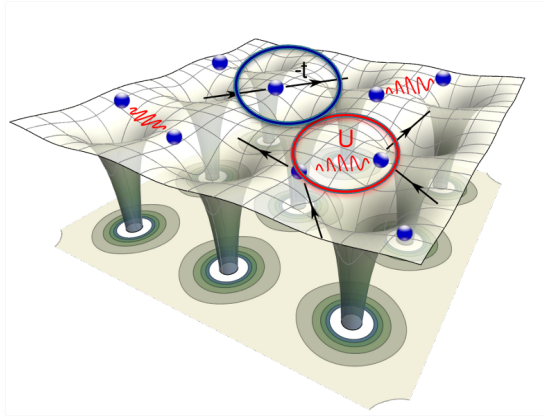


Figure 1.4: Illustration of the Hubbard model as a description of correlated electrons in solids from [22]. The electron can hop from one site to another with the hopping amplitude $-t$. An energy U has to be paid whenever a double occupation occurs.

It is worth noting at this point that, although this model represents already a great simplification compared to real material systems described by Eq. 1.2, it is still not solvable except for trivial or quite specific (e.g. one-dimensional) cases. However, the challenging task of working with the Hubbard model is

highly rewarding, since most of the interesting physics in highly correlated electron systems is indeed originated by the (direct or indirect) result of the **competition of kinetic and potential energy**, which is well captured by this model Hamiltonian.

On the basis of the discussions above, it is evident that any improvement of the theoretical description of the physics described by the Hubbard model represents a highly desirable goal in contemporary solid state physics, with significant possible impact on the understanding of the phenomena mentioned at the end of section 1.1. At the present stage, one of the most powerful tools for treating the Hubbard model is the dynamical mean field theory (DMFT) as well as its extensions, which, hence, will be examined in sec. 2.2, as they will be extensively used to produce the desired results of this thesis.

Chapter 2

Theory and methods: from the one-particle propagator to the fully irreducible vertex

In this chapter a concise introduction to quantum field theory concepts and to the methods used to obtain the results of this thesis is given. In section 2.1 the concepts of the (one-particle) Green function and the self-energy are illustrated. In section 2.2 the fundamentals of the dynamical mean field theory (DMFT) are presented: DMFT provides a self-consistent description at the one-particle level of the major contributions of electronic correlations, i.e. the local ones. Subsequently, the most famous extensions of DMFT which include non-local electronic correlations are discussed in section 2.3. As some of these extensions require a self-consistent treatment beyond the one-particle level, in section 2.4 the general quantum field theory formalism for calculating two-particle quantities is also discussed.

As already explained in section 1.3, solving the full many-body Hamiltonian in equation 1.2 is neither possible nor necessary. Rather, one wants to access quantities of physical relevance¹. A possible strategy, as presented in section 1.3, is to build up model Hamiltonians (such as the Hubbard Hamiltonian in Eq. 1.7 for strongly correlated electron systems), which are easier to deal with, but, at the same time, still capture the essence of the underlying physics. There is a variety of theories available that are able to provide at least some of the interesting physical informations (such as the charge density, magnetization, susceptibilities, etc.) without referring to wave functions and they can be summarized by the umbrella term functional theories.

If one essentially neglects electronic correlations² an extremely good treatment can be obtained from the **density functional theory (DFT)**, within which the

¹which means expectation values of operators, spectral and response functions to be compared with experiment

²which is usually a good approximation for s- and p-electron materials

electronic and correlation part of the energy functional is typically approximated by the **local density approximation (LDA)** or the **generalized gradient approximation (GGA)** for instance (see, e.g., [23]).

On the other hand, if electronic correlations have to be considered explicitly as it is the case in this thesis, many body perturbation theory (MBPT) or the **theory of Green functions** has to be used. Technically, an infinite hierarchy of many-particle Green functions (i.e. the one-particle, two-particle, etc. Green function) has to be included. But for conventional problems, usually regarding one- and two-particle Green functions in the calculations represents an adequate approximation. In the following sections, therefore, the one- and two-particle Green functions will be discussed in more detail.

2.1 Many-body Green function: the one-particle propagator

2.1.1 Definition of the Green function

One of the central quantities of many-body electron theory is the Green function. The causal one-particle fermionic Green function³ can be defined in Heisenberg notation as

$$\begin{aligned} G(\vec{r}, t; \vec{r}', t') &= -i \langle \mathcal{T} \Psi(\vec{r}, t) \Psi^\dagger(\vec{r}', t') \rangle = \\ &= -i [\theta(t - t') \langle \Psi(\vec{r}, t) \Psi^\dagger(\vec{r}', t') \rangle \mp \theta(t' - t) \langle \Psi^\dagger(\vec{r}', t') \Psi(\vec{r}, t) \rangle] \end{aligned} \quad (2.1)$$

where \mathcal{T} denotes the time-ordered product and the angle brackets either the expectation value with respect to the ground state or the expectation value in the corresponding thermodynamic ensemble in case of finite temperature, and the plus (minus) sign is applied for bosons (fermions). The definition of the Green function has a clear and easy physical interpretation, namely the propagation of one electron being added to the system at time t' at \vec{r}' and being removed at time t at \vec{r} , or the analogous propagation of a hole (see also Fig. 2.1).

When performing calculations for finite temperatures T , in order to avoid time-evolution operators with complex time arguments (of the form $e^{iH(t \pm i\beta)}$ with inverse temperature $\beta = \frac{1}{T}$), it is technically preferable to use imaginary instead of real times, by performing a so called “Wick rotation”:

$$t \rightarrow \tau = it \quad (2.2)$$

If one then Fourier transforms the Green function of a time-translational system, it reads [25]

$$G(\vec{r}, \vec{r}'; i\omega_m) = \int_0^\beta d\tau e^{i\omega_m \tau} G(\vec{r}, \vec{r}'; \tau) \quad (2.3)$$

³sometimes also called two-point function, because it relates the space-time coordinate (\vec{r}', t') to that of (\vec{r}, t)

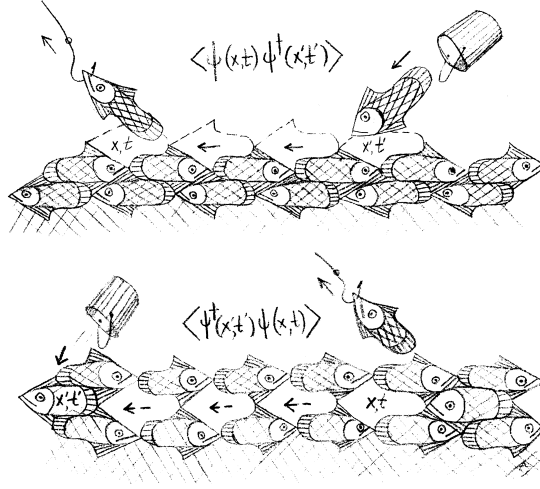


Figure 2.1: Physical interpretation of the one-particle Green function in terms of "fishing": propagation of one electron (hole) being added to the system at time t' (t) at x' (x) and being removed at time t (t') at x (x') (taken from [24]).

in the imaginary frequency space where $\beta = 1/T$ is the inverse temperature and the ω_m are the so-called **Matsubara frequencies**. As a consequence of the commutation (anti-commutation) rules for bosonic (fermionic) field operators, the Fourier spectrum of the Matsubara-frequencies is **discrete** ($m \in \mathbb{Z}$) [26]:

$$\omega_m = \begin{cases} (2m+1)\frac{\pi}{\beta} & \text{in case of fermions} \\ 2m\frac{\pi}{\beta} & \text{in case of bosons} \end{cases} \quad (2.4)$$

In momentum-space the field operators can be constructed via

$$\Psi(\vec{r}, t) = \frac{1}{(2\pi)^3} \int d^3k e^{-i\vec{k}\vec{r}} a_{\vec{k}}(t) \quad (2.5)$$

$$\Psi^\dagger(\vec{r}, t) = \frac{1}{(2\pi)^3} \int d^3k e^{i\vec{k}\vec{r}} a_{\vec{k}}^\dagger(t) \quad (2.6)$$

These equations can be directly used in the non-interacting case (e.g. $U = 0.0$ for the Hubbard model), to diagonalize the Hamilton operator:

$$H_0 = \frac{1}{(2\pi)^3} \int d^3k \epsilon_k a_{\vec{k}}^\dagger a_{\vec{k}} \quad (2.7)$$

Inserting this Hamiltonian into the definition of the Green function Eq. 2.2 and assuming that the imaginary time $\tau > 0$, the **non-interacting Green function** reads

$$G_0(\vec{k}, \tau) = -e^{-\epsilon_k \tau} (1 - f(\epsilon_k)) \quad (2.8)$$

where

$$f(\epsilon_k) = \frac{1}{e^{\beta \epsilon_k} + 1} \quad (2.9)$$

is the Fermi distribution function. As for the physical interpretation, one can reverse the Wick rotation, return to real times, and finally

$$G_0(\vec{k}, \tau) \approx e^{-i\epsilon_k \tau} \quad (2.10)$$

which exhibits the free (plane wave) propagation. From this, in turn, it can easily be understood that no scattering events with other electrons take place, so that infinite long-living electronic excitations define the spectral properties of the system. Finally, one can Fourier transform Eq. 2.14 in order to retrieve the non-interacting Green function in momentum space, yielding

$$G_0(\vec{k}, i\omega_m) = \frac{1}{i\omega_m - \epsilon_k} \quad (2.11)$$

From the point of view of **Feynman diagrams**, this non-interacting Green function is easily depicted as a (not interrupted) fermionic propagating line (see fig. 2.2):



Figure 2.2: Representation in terms of a Feynman diagram of the non-interacting Green function.

2.1.2 Reducibility at the one-particle level: the self-energy

In order to include the system's interactions systematically, it is very useful to introduce the concept of a **self-energy**. Diagrammatically speaking the self-energy is built up by all **one-particle irreducible** diagrams, i.e. all connected diagrams which cannot be separated in two by **cutting one internal fermionic line**. Fig. 2.3 shows an example of either a (one-particle) irreducible and reducible diagram. Following this concept, one obtains an implicit relation for

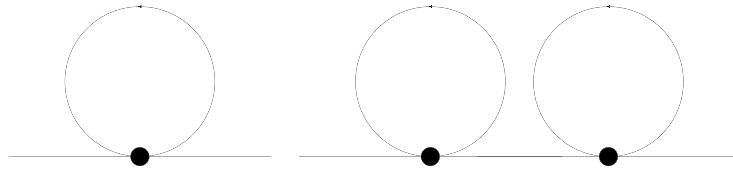


Figure 2.3: Left: one-particle irreducible diagram. Right: one-particle reducible diagram. The thick dot denotes the Coulomb interaction and the straight line the non-interacting Green function.

the interacting Green function out of the non-interacting one and the self-energy via

$$G(\vec{k}, i\omega_m) = G_0(\vec{k}, i\omega_m) + G_0(\vec{k}, i\omega_m)\Sigma(\vec{k}, i\omega_m)G(\vec{k}, i\omega_m) \quad (2.12)$$

which can also be expressed diagrammatically (see Fig. 2.4). Eq. 2.12 is the famous **Dyson equation**.



Figure 2.4: Diagrammatic representation of the Dyson equation. The interacting Green function is represented by a bold line, the non-interacting by a light one.

Solving this equation the **interacting Green function** for G can be expressed by

$$G(\vec{k}, i\omega_m) = \frac{1}{G_0^{-1}(\vec{k}, i\omega_m) - \Sigma(\vec{k}, i\omega_m)} \quad (2.13)$$

which also can be written explicitly as

$$G(\vec{k}, i\omega_m) = \frac{1}{i\omega_m - \epsilon_k - \Sigma(\vec{k}, i\omega_m)} \quad (2.14)$$

Making the connection with experiments: the spectral function

While Green function and self-energy are useful but quite abstract concepts, it is instructive to relate them to experimentally accessible quantities. the most direct link at the one-particle level is provided by the **spectral function** $A(\vec{k}, \omega)$ as

$$G(\vec{k}, i\omega_m) = \int_{-\infty}^{\infty} d\omega \frac{A(\vec{k}, \omega)}{i\omega_m - \omega} \quad (2.15)$$

Expressing the interacting spectral density in terms of the self-energy reveals [27]

$$A(\vec{k}, \omega) = -\frac{1}{\pi} \frac{\text{Im}(\Sigma(\vec{k}, \omega))}{[\omega - \epsilon_k - \text{Re}(\Sigma(\vec{k}, \omega))]^2 + [\text{Im}(\Sigma(\vec{k}, \omega))]^2} \quad (2.16)$$

From the experimental point of view, $A(\vec{k}, \omega)$ can be measured in photoemission spectroscopy, e.g. in an ARPES⁴ experiment one uses the photoelectric effect for probing the system by providing photons of certain energy and polarization to the system and analysing the energy and angle of the outgoing electrons released by the photoelectric effect (see Fig. 2.5 (a)).

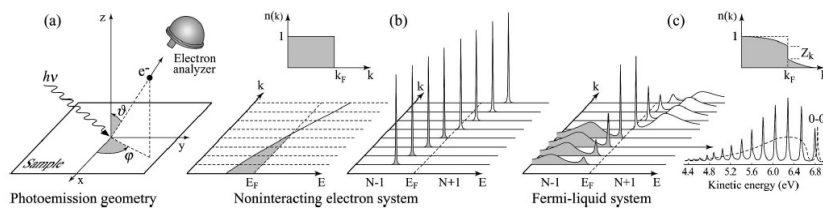


Figure 2.5: (a) Geometry of an ARPES experiment, (b) momentum resolved one-electron removal and addition spectra for the non-interacting electron system, (c) the same spectra for a Fermi-liquid system (taken from [27]).

Invoking the sudden approximation one can write the intensity measured in an ARPES experiment on a 2D single-band system as [27]

$$I(\vec{k}, \omega) = I_0(\vec{k}, \nu, \vec{\Pi}) f(\omega) A(\vec{k}, \omega) \quad (2.17)$$

⁴angle resolved photo emission spectroscopy

where $I_0(\vec{k}, \nu, \vec{\Pi})$ depends on the electron momentum \vec{k} and the energy ν and polarization $\vec{\Pi}$ of the incoming photon. In this way one can directly measure the spectral function by probing the sample with ARPES.

Self-energy and the Fermi liquid theory

In order to make the notion of a self-energy concrete, one can take a look at it in the case of the Fermi liquid. Most of the properties of metallic systems can be understood qualitatively by renormalization of non-interacting calculations, which means that the structure of the electronic excitations for $E \approx E_F$ (E_F is the Fermi-energy) qualitatively resembles that of the non-interacting case. The connection of the self-energy to the Fermi liquid can be established by Taylor expanding the self-energy at the Fermi level, so that $k \rightarrow k_F$ and $i\omega_m \rightarrow 0$:

$$\begin{aligned} \Sigma(k, i\omega_m) \cong & \underbrace{\text{Re}(\Sigma(k_F, i\omega_m \rightarrow 0))}_{\text{reabsorbed in chemical potential}} + \quad (2.18) \\ & + \underbrace{\frac{\partial}{\partial k} \text{Re}(\Sigma(k_F, 0))}_{\text{correction to } \epsilon_k} (k - k_F) + \\ & + \underbrace{i \text{Im}(\Sigma(k_F, 0))}_{-i\gamma} + \underbrace{\frac{\partial}{\partial \omega_m} \text{Im}(\Sigma(k_F, 0))}_{-i\alpha\omega_m} \end{aligned}$$

Introducing the renormalization factor⁵

$$Z = \frac{1}{1 + \alpha} < 1, \quad (2.19)$$

inserting Eq. 2.19 and 2.19 into 2.14 and setting $v_F = \left. \frac{\partial}{\partial k} \epsilon_k \right|_{k_F}$ the Green function of the Fermi liquid in the vicinity of the Fermi surface reads

$$G(\vec{k}, i\omega_m) = \frac{Z}{i\omega_m - Z(v_F + \left. \frac{\partial}{\partial k} \Sigma \right|_{k_F}) (k - k_F) + iZ\gamma} \quad (2.20)$$

so that in contrast to the non-interacting system the **quasiparticle excitations** of the interacting system become **renormalized** and their **life times become finite off the Fermi surface**. This becomes clear by performing the inverse Fourier transform on the interacting Green function which yields

$$G(k, t) \approx e^{-i(\epsilon_k + \text{Re}(\Sigma(k)))t} e^{-\gamma t} \quad (2.21)$$

so that the propagator is not a plane wave any more, but rather a decaying exponential function with the typical decay time of $t_{\text{dec}} = \frac{\hbar}{\gamma}$. The shape of the spectral function for the Fermi liquid can be seen in Fig. 2.5 (c).

⁵This factor represents the mass renormalization of the electron due to mutual electron-electron interactions, so that the elementary excitations of the system are not the bare electrons, but “dressed” electrons or **quasiparticles**.

⁶This is the quasiparticle’s lifetime.

Self-energy in the atomic limit

In contrast to the Fermi liquid case, in the atomic limit (for the Hubbard model, this limit means $t = 0.0$ while U and T stay finite) the self-energy cannot be Taylor expanded. Rather, the spectral function is given by the sum of two delta distributions

$$A^{\text{a.l.}}(\vec{k}, \omega) = \frac{1}{2} \left[\delta\left(\omega - \frac{U}{2}\right) + \delta\left(\omega + \frac{U}{2}\right) \right] \quad (2.22)$$

Using equation 2.15 one immediately obtains

$$\Sigma^{\text{a.l.}}(\vec{k}, i\omega_n) = \frac{U^2}{i4\omega_n} \quad (2.23)$$

for the self-energy on the Matsubara axis in the atomic limit. Performing the analytic continuation, for the retarded self energy one arrives at

$$\Sigma_{\text{ret}}^{\text{a.l.}}(\vec{k}, \omega) = \frac{U^2}{4\omega} - i \frac{U^2}{4} \delta(\omega) \quad (2.24)$$

in which expression a divergence in form of a delta distribution appears because of the spectral gap of the Mott phase.

2.1.3 Breakdown of perturbation theory

Differently from the case of quantum electrodynamics, where the reliability of the perturbative approach is guaranteed by the smallness of the coupling constant (i.e. the fine structure constant $\alpha_f = \frac{1}{137}$ [28]), in solid state physics the value of the on-site Coulomb interaction U , which should be treated as a perturbation, is often not small at all compared to other energy scales of the system. The breakdown of the perturbative description leads, in fact, to very important physical processes like the famous Mott-Hubbard metal-insulator transition (see sec. 1.2.2). This implies that straightforward approaches based on perturbation theory cannot be applied to such systems [29] and one has to find non-perturbative techniques to deal with them. One of the most successful among these techniques is the dynamical mean field theory (DMFT) which is covered in the next section.

2.2 The dynamical mean field theory (DMFT)

The essential of dynamical mean field theory (DMFT) is to map the whole many body problem of Eq. 1.2 onto a single site Anderson impurity model (AIM) to be determined self-consistently [30]. For retrieving physical quantities (e.g. via the calculation of the self-energy) one has to solve a self-consistency cycle based on the single-site (AIM) quantity and the local component of the same quantity of the original lattice. This corresponds to treating the spatial degrees of freedom of a given system at a mean field theory level (like in a classical mean or Weiss field theory), whereas fully retaining local temporal fluctuations⁷. The mapping becomes exact in the limit of infinite coordination number and DMFT

⁷ often referred to as “quantum fluctuations”

therefore is an exact theory in this asymptotic regime. More formally, for a fixed lattice geometry the limit of infinite coordination corresponds to the limit of high spatial dimensions or high temperatures.

2.2.1 The diagrammatic content of DMFT

If one considers the expectation value for the kinetic energy part of the Hubbard Hamiltonian including next neighbour (NN) hopping only

$$\langle H_{\text{kin}} \rangle = -t \sum_{(i,j),\sigma} \langle c_{i,\sigma}^\dagger c_{j,\sigma} \rangle \quad (2.25)$$

and the coordination number (i.e. the number of next neighbours for each lattice site) of the lattice being z , the probability (i.e. the absolute square of the hopping amplitude) that an electron hops from a site j to a next neighbour site of j is given by $P = \frac{1}{z}$. From this consideration one can conclude that in the limit of infinite coordination $z \rightarrow \infty$ the proper scaling of the kinetic energy in the Hubbard model (Eq. 1.7) is $t \propto \frac{1}{\sqrt{z}}$, whereas the proper scaling of the potential energy is trivial because it is purely local [31]. The crucial point, however, is, that with this scaling also all self-energy skeleton diagrams become purely local in the limit $z \rightarrow \infty$ (see Fig. 2.6) as it was shown by Metzner and Vollhardt [31, 32], and, hence:

$$\Sigma(\vec{k}, i\omega_m) \rightarrow \Sigma(i\omega_m) \quad (2.26)$$

Therefore, from the diagrammatic point of view, **DMFT** corresponds to regarding all completely **local one-particle irreducible diagrams** as the electron self-energy (see also Fig. 2.6), which physically corresponds to consider only the **local part** of the electronic correlation, but **without any perturbative restriction**.

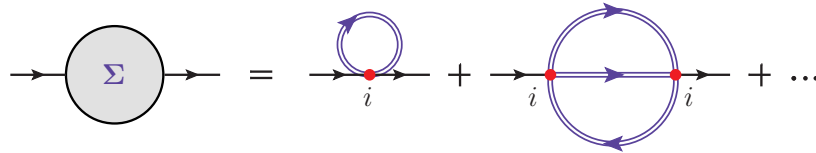


Figure 2.6: Diagrammatic content of the DMFT (taken from [33]). The thick red dot denotes the local interaction U , the single lines the non-interacting and the double lines the dressed Green functions. All local one-particle irreducible diagrams are regarded as the electronic self-energy.

2.2.2 Self-consistency cycle and impurity solvers

From the practical point of view, one of the keys for explaining the success of DMFT is the above mentioned mapping of the original lattice problem onto an Anderson impurity problem. Such a mapping is possible because the same diagrams which constitute the (as said: purely local) DMFT self-energy can also be obtained from the Anderson impurity model [3]

$$H = \sum_{\vec{k}l\sigma} \epsilon_l(\vec{k}) a_{\vec{k}l\sigma}^\dagger a_{\vec{k}l\sigma} + \sum_{\vec{k}l\sigma} V_{lm}(\vec{k}) a_{\vec{k}l\sigma}^\dagger c_{m\sigma} + h.c. + \sum_{i\sigma} U c_{i\sigma}^\dagger c_{i\sigma}^\dagger c_{i\sigma'} c_{i\sigma} \quad (2.27)$$

provided the on-site interaction U coincides with the one of the original Hubbard model in Eq. 1.7. In the definition of the Anderson impurity model, $a_{\vec{k}l\sigma}^\dagger$ and $a_{\vec{k}l\sigma}$ are the creation and annihilation operators of conduction band electrons with dispersion $\epsilon_l(\vec{k})$, $c_{im\sigma}^\dagger, c_{im\sigma}$ are the creation and annihilation operators of the impurity site and $V_{lm}(\vec{k})$ defines the hybridization between conduction band and impurity site electrons.

The DMFT self-consistency cycle

As pointed out by Georges and Kotliar [14], due to the equivalence of the (purely local) diagrams which constitute the self-energy of both DMFT and Anderson impurity model, one is able set up a self-consistency cycle for the Green function of the Anderson impurity model $G_{\text{AIM}}(i\omega_n)$ and the local DMFT Green function

$$G_{\text{loc}}(i\omega_n) = \frac{1}{V_{\text{BZ}}} \int_{\text{1st BZ}} \frac{1}{i\omega_n - \epsilon_k - \Sigma(\omega)} \quad (2.28)$$

where V_{BZ} is the volume of the first Brillouin zone. The local self-energy $\Sigma(i\omega_n)$, which defines the **local Green function** via the Dyson Eq. 2.12, can be obtained from the AIM via

$$\Sigma(i\omega_n) = \mathcal{G}_0^{-1}(i\omega_n) - G_{\text{AIM}}^{-1}(i\omega_n) \quad (2.29)$$

where the **electronic bath function** of the AIM

$$\mathcal{G}_0^{-1}(i\omega_n) = i\omega_n - t - \sum_{\vec{k}n} \frac{V_{nl}^\dagger(\vec{k})V_{nm}(\vec{k})}{i\omega_n - \epsilon_n(\vec{k})} \quad (2.30)$$

can be considered as the quantum (dynamical) counterpart of a classical Weiss mean field. Fig. 2.7 schematically shows all the steps for performing a self-consistency loop of DMFT. Among these steps one can note that the computational bottleneck of the algorithm is given by the solution of the impurity problem.

Common impurity solvers are based on exact diagonalization (ED) or Lanczos algorithms [30], numerical renormalization group (NRG, [34]), Quantum Monte Carlo (QMC) or semi analytical methods like iterated perturbation theory (IPT, see e.g. [35]). As in this work mainly ED and QMC will be used, those impurity solvers will be briefly discussed in the following sections.

Exact diagonalization (ED)

In exact diagonalization (ED) one solves the AIM by approximating the Hamiltonian of the AIM with a Hamiltonian built up by a finite number of orbitals n_S (**discretization of the bath**) [30]. The Hamiltonian is then diagonalized by standard algorithms.

More in detail, for solving the AIM in ED one has to perform essentially three steps:

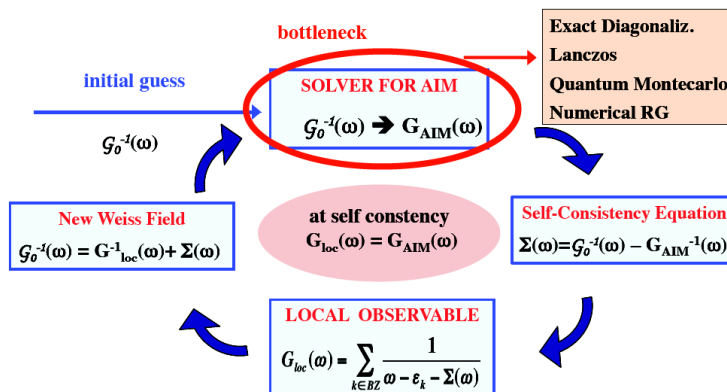


Figure 2.7: Self-consistency cycle of the DMFT (taken from [15]). The bottleneck of the algorithm is given by the solution of the impurity problem.

1. The Weiss function

$$\mathcal{G}_0(i\omega_n)^{-1} = i\omega_n - \int_{-\infty}^{\infty} d\omega' \frac{\Delta(\omega')}{i\omega_n - \omega'} \quad (2.31)$$

is approximated by a discretised version:

$$\mathcal{G}_0^{n_S}(i\omega_n)^{-1} = i\omega_n - \sum_{p=2}^{n_S} \frac{V_p^2}{i\omega_n - \tilde{\epsilon}_p} \quad (2.32)$$

2. The obtained Hamiltonian of Eq. 2.32 is **diagonalized exactly**. The corresponding Green function is calculated.
3. The DMFT self-consistency condition provides a new Weiss function \mathcal{G}_0 which is also approximated by a function $\mathcal{G}_0^{n_S}$ with a new set of V_p and $\tilde{\epsilon}_p$.

ED provides very accurate and stable numerical results on the Matsubara axis (see again [30]). However, the scaling of the ED algorithm with n_S is very costly, which makes the calculation of two-particle vertex quantities already quite challenging even for the single-band Hubbard model.

Hirsch-Fye Quantum Monte Carlo (QMC)

An efficient and well-established approach of an impurity model solver is the Hirsch-Fye Quantum Monte Carlo method [36, 37] which is also used to produce most of the numerical results in this thesis. Hirsch and Fye mapped the interacting Anderson impurity model of Eq. 2.27 onto a sum of non-interacting problems with a single particle under the influence of a time-dependent field, whereupon this sum is evaluated by Monte Carlo sampling. The most important steps of Hirsch-Fye QMC are summarized in the following, for more details see [32, 38, 17].

The Hamiltonian H for the (single or cluster) impurity is assumed to be expressed in two parts

$$H = \underbrace{H_0}_{\text{non-interacting}} + \underbrace{H_1}_{\text{interacting}} \quad (2.33)$$

and the interaction on the impurity cluster to be local. In a first step, the imaginary time interval $[0, \beta]$ is divided (**Trotter discretization**) into L steps of size

$$\Delta\tau = \frac{\beta}{L} \quad (2.34)$$

Now the thermodynamic partition function can be expressed in terms of these time slices

$$Z = \text{Tr}(e^{-\beta H}) = \text{Tr}\left(\prod_{i=1}^L e^{-\Delta\tau H}\right) \quad (2.35)$$

and one can apply the **Trotter-Suzuki decomposition** [39]

$$e^{-\Delta\tau H} = e^{-\frac{\Delta\tau H_0}{2}} e^{-\Delta\tau H_1} e^{-\frac{\Delta\tau H_0}{2}} + \mathcal{O}(\Delta\tau^3) \quad (2.36)$$

Using the cyclic property of the trace one arrives at

$$Z \approx \text{Tr}\left(\prod_{i=1}^L e^{-\Delta\tau H_0} e^{-\Delta\tau H_1}\right) \quad (2.37)$$

with an error of the order $\Delta\tau^2$. With the use of Hirsch's identity for a purely locally interacting Hamiltonian,

$$e^{-\Delta\tau U(n_{i\uparrow}n_{i\downarrow} - \frac{1}{2}(n_{i\uparrow} + n_{i\downarrow}))} = \frac{1}{2} \sum_{s_i = \pm 1} e^{as_i(n_{i\uparrow} - n_{i\downarrow})} \quad (2.38)$$

where

$$\cosh(a) = e^{\frac{\Delta\tau U}{2}} \quad (2.39)$$

one can introduce an auxiliary Ising field (so called **Hubbard-Stratonovich field**) so that the interacting problem has been mapped onto the sum over all possible configurations of the auxiliary field of non-interacting Ising-spins. The partition function becomes [30]

$$Z = \sum_{\{s_1, \dots, s_L\}} \det \left[G_{\uparrow}^{-1}(s_1, \dots, s_L) \right] \det \left[G_{\downarrow}^{-1}(s_1, \dots, s_L) \right], \quad (2.40)$$

which requires the summation over 2^L configurations. Therefore, in QMC, the interacting Green function is calculated by stochastic Monte Carlo sampling, where $\det \left[G_{\uparrow}^{-1}(s_1, \dots, s_L) \right] \det \left[G_{\downarrow}^{-1}(s_1, \dots, s_L) \right]$ is the stochastic weight and the configurations $\{s_1, \dots, s_L\}$ are the outcome of a Markov process which visits configurations of Ising variables with a single spin-flip dynamic. For a more rigorous derivation of the Hirsch-Fye QMC algorithm see Sec. VI. A1b in [30].

From the description and practical applications of the Hirsch-Fye QMC method three immediate drawbacks emerge [40]:

1. It requires an equally spaced time discretization.
2. At large interactions and low temperatures difficulties in managing the discretization and equilibration arise and particular care should be taken to treat the systematic errors introduced by the Trotter discretization (see [17]).
3. In the multi-orbital case, treating the SU(2)-invariant local interactions becomes very challenging.

At least parts of those drawbacks can be overcome by another QMC technique called **continuous time QMC** (CTQMC), whose fundamental concept is avoiding the time discretization by sampling in a diagrammatic expansion, instead of sampling the configurations in a complete set of states (see [40] and [41]).

2.2.3 Successes and limitations of the DMFT

DMFT nowadays is a well-established, successful and applicable technique in the field of strongly correlated electron systems. In this respect, one can mention here the famous statement of P. Anderson (Nobel prize for his “fundamental theoretical investigations of the electronic structure of magnetic and disordered systems” in 1977) [42]:

“In theory, the big news is the DMFT which gives us a systematic way to deal with the major effects of strong correlations. After nearly 50 years, we are finally able to understand the Mott transition, for instance, at last.”

- P. W. Anderson

In fact, the non-perturbative nature of DMFT has allowed, for the first time, for a coherent and general description of the Mott-Hubbard transition: In Fig. 2.8 one of the most known DMFT results is shown, i.e. the evolution of the local spectral function in the half-filled Hubbard model. This result demonstrates how the MIT occurs in the limit of high coordination number, as a result of purely local quantum fluctuations.

However, the success of this theory should not lead to forget that there exist some important limitations of DMFT:

1. While local quantum fluctuations are fully taken into account by DMFT, due to its mean field nature in space, spatial correlations are totally neglected. This has the immediate consequence that DMFT will perform poorly in all situations in which these correlations become crucial, e.g. in the vicinity of (second-order) phase transitions where the correlation length is diverging. Also for the description of low dimensional systems, such as layered, surface- and nano-systems non-local spatial correlations play an important role and have to be considered.
2. If DMFT is applied to not infinitely coordinated systems, its self-consistency is guaranteed at the one-particle level only. This means that for $d \neq \infty$

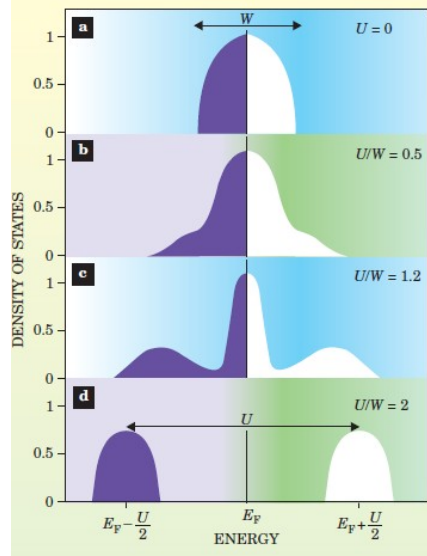


Figure 2.8: Illustration of the MIT by the density of states (DOS) resulting from DMFT-calculations for the half-filled Hubbard model (taken from [43]). In the case of independent electrons, the DOS is half-elliptically shaped (a). At intermediate coupling ((b) and (c)) one can observe the development of a three-peak structure (with a quasiparticle peak at the Fermi energy), whereas for strong coupling, the DOS splits into two Hubbard bands with a gap in between (d). This marks the occurrence of the MIT.

the momentum-integrated density-density correlation function of the lattice computed in DMFT is not equal to the corresponding quantity of the associated AIM:

$$\sum_{\vec{q}} \chi(\vec{q}) \neq \chi_{\text{loc}}^{\text{AIM}} \quad (2.41)$$

leading to an intrinsic ambiguity in the calculations at least of the local response functions.

To overcome these limitations, one has to take a step beyond DMFT, as it is discussed in the following section.

2.3 Going beyond DMFT

Among all existing extensions of DMFT, one can essentially individuate two classes: cluster extensions and diagrammatic extensions. In a nutshell the former are based on a simple generalization of the DMFT algorithm from a single site to a cluster of sites (either in real or in momentum space), whereas the later aim at including the most relevant non-local diagrams to the DMFT.

2.3.1 Cluster extensions of DMFT

Several methods of cluster extensions of DMFT have been proposed, for instance

- cellular dynamical mean field theory (CDMFT), based on clusters in real space and
- dynamical cluster approximation (DCA), based on clusters in momentum space.

This section will focus on the DCA as it has been used throughout this thesis for performing cluster calculations. More details on CDMFT (as well as on DCA) can be found in [44]. This introduction essentially follows [45].

Quantum cluster approaches systematically include non-local correlations to DMFT by mapping the infinite periodic lattice onto a finite sized cluster problem. This implies that spatial correlations are fully included up to the size of such a cluster, while spatial correlations on larger scales are treated still at a mean field level.

In the DMFT the Green function G_{loc} is **coarse grained** over the whole Brillouin zone

$$G_{\text{loc}}(\omega) = \sum_{\vec{k} \in 1^{\text{st}} \text{ BZ}} G(\vec{k}, \omega), \quad (2.42)$$

which results in a momentum independent self-energy. In the DCA, instead, the reciprocal lattice is divided into N_c cells of size Δk (see Fig. 2.9). Note that the coarse graining is only performed within each cell so that non-local spatial correlations up to a length of $\xi \approx \frac{\pi}{\Delta k}$ are taken into account. This new cluster problem can be solved again by techniques as Hirsch-Fye QMC [36] or CTQMC (especially in its weak-coupling version, [40]), until the (in this case DCA) self-consistency is reached.

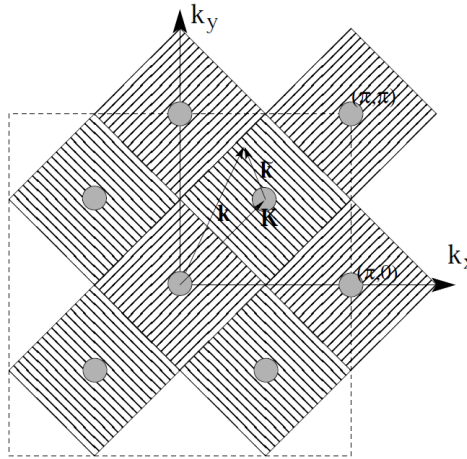


Figure 2.9: Coarse graining cells in DCA for $N_c = 8$ that partition the first Brillouin zone. The cells are centred at a cluster momentum \vec{K} . To construct the DCA cluster \vec{k} is mapped to the nearest cluster centre \vec{k} so that $\vec{k} = \vec{k} - \vec{K}$ remains in the cell around \vec{K} (taken from [45]).

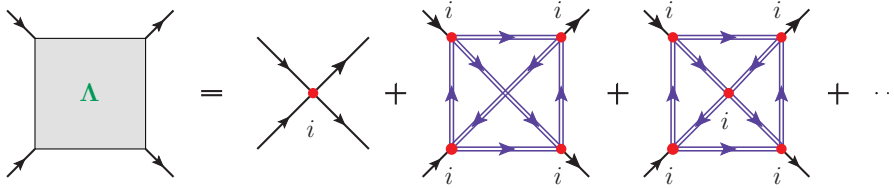


Figure 2.10: Diagrammatic content of the dynamical vertex approximation (D Γ A). The D Γ A claims the locality of the two-particle fully irreducible vertex Λ , which can, hence, be calculated directly from the single-site AIM. The (local) vertex Λ represents the crucial input for the D Γ A calculations, which can, in this way, include spatial correlations at all length scales beyond DMFT (taken from [33]).

DCA, as well as other cluster extensions of DMFT) has been successfully applied in many cases (see [44]). However, if the inclusion of spatial correlations on all length scales is needed, one has to abandon the cluster extension schemes and adopt the complementary treatment of the diagrammatic method described in the next section.

2.3.2 Diagrammatic extensions of DMFT

The dynamical vertex approximation

A different, complementary approach for including non-local correlations is the systematic inclusion of non-local Feynman diagrams beyond DMFT. Diagrammatically speaking, as discussed in section 2.2 and Fig. 2.6, the DMFT self energy consists of all connected one-particle irreducible local diagrams. A proposal advanced by A. Toschi, K. Held and A. Katanin in 2007 was to push the requirement of **locality** one level higher in the hierarchy of diagrams, namely at the two-particle level [46]. More specifically, the two-particle quantity corresponding to the self-energy for which the assumption of locality is made, is the so-called **two-particle fully irreducible vertex** Λ (Fig. 2.10), often also indicated by Γ_{irr} ⁸, from which the name **dynamical vertex approximation (D Γ A)** originally stems. Note that the locality at the two-particle level does not imply the locality at the one-particle level at all, so that spatial correlations at all length scales can now be included systematically and in a fully non-perturbative way.

As for the validity of the D Γ A, it is clear from the discussion above that it crucially depends on the properties of the fully irreducible vertex. Hence, a rigorous examination of this vertex function, which has hitherto never been performed, is indicated. Therefore, in chapter 3 the frequency structure of the local fully irreducible vertex (and other two-particle quantities introduced in section 2.4) is being analysed for the first time. Furthermore, in chapter 4, also the non-local structures of these objects are calculated and investigated, providing essential information for the applicability of the diagrammatic extensions of DMFT.

⁸For a definition of irreducibility at the two-particle level see subsection 2.4.2.

Other approaches

Another approach for including long-range spatial correlations in DMFT is the dual fermion (DF) method. In DF these correlations are treated systematically by introducing additional auxiliary degrees of freedom via a Hubbard-Stratonovich transformation for the non-local degrees of freedom, which are called **dual fermions**. A subsequent integration of the local degrees of freedom yields a new problem in terms of the dual fermions which interact via the reducible local 4-point full vertex F (see section 2.4) of the AIM⁹. For a detailed description of the DF approach and its application to the two-dimensional Hubbard model, see [48, 49] and also [50].

2.3.3 Two-particle quantities: crucial ingredients

Both diagrammatic extensions of DMFT, the DΓA and the DF method, are based on local two-particle quantities calculated at the level of the AIM. Furthermore, two-particle quantities are essential for the calculation of momentum-dependent response functions ([30, 40] and also [51] for an alternative method to compute momentum- and frequency-dependent response function from a DMFT or DCA input). As a detailed and systematic study of the DMFT (or DCA) vertex functions has never been performed so far (with the recent exception of [52]), it is definitely worth taking a look at general properties of non-local two-particle quantities, which are presented in the following section, before the corresponding numerical results are given in chapter 3 and 4.

2.4 Two-particle quantities

As the notation for and fundamental relations between two-particle quantities are expatiated in [52, 53], in this section I will explicitly recall the facts that are important to this work.

2.4.1 The two-particle Green function and the generalized susceptibility

The general n -particle Green function is defined as [26]:

$$G_{n;\sigma_1,\dots,\sigma_{2n}} = (-1)^n \langle \mathcal{T} c_{\sigma_1}^\dagger(\tau_1) \dots c_{\sigma_{2n}}(\tau_{2n}) \rangle \quad (2.43)$$

For $n = 1$ the one-particle Green function (Eq. 2.2) is recovered. In the two-particle case, however, the **generalized susceptibility** is typically used¹⁰, which is defined as follows [52]:

$$\chi_{\sigma_1,\sigma_2,\sigma_3,\sigma_4} = G_{2;\sigma_1,\sigma_2,\sigma_3,\sigma_4}(\tau_1, \tau_2, \tau_3, \tau_4) - G_{1;\sigma_1,\sigma_2}(\tau_1, \tau_2) G_{1;\sigma_3,\sigma_4}(\tau_3, \tau_4) \quad (2.44)$$

⁹Note, that in principle the exact integration of the local degrees of freedom would yield also higher vertex function (6-point, 8-point etc.) for the dual fermion interaction. These contributions are, however, usually neglected. In this context, see also the discussion in [47].

¹⁰because of its direct connection to physical susceptibilities and response functions

Similarly to the one-particle Green function, one can restrict the considered imaginary time interval to $[0, \beta]$ and take into account the time-translational invariance of the Hamiltonian which results in setting the time $\tau_4 = 0$:

$$\chi_{\sigma_1, \sigma_2, \sigma_3} = G_{2; \sigma_1, \sigma_2, \sigma_3, \sigma_4}(\tau_1, \tau_2, \tau_3, 0) - G_{1; \sigma_1, \sigma_2}(\tau_1, \tau_2)G_{1; \sigma_3, \sigma_4}(\tau_3, 0) \quad (2.45)$$

Then the Fourier transform of this quantity can be defined for convenience in two different ways:

$$\chi_{ph; \sigma, \sigma'}^{\nu, \nu', \omega} = \int_0^\beta d\tau_1 d\tau_2 d\tau_3 \chi_{\sigma, \sigma'}(\tau_1, \tau_2, \tau_3) e^{-i\nu\tau_1} e^{i(\nu+\omega)\tau_2} e^{-i(\nu'+\omega)\tau_3} \quad (2.46)$$

or

$$\chi_{pp; \sigma, \sigma'}^{\nu, \nu', \omega} = \int_0^\beta d\tau_1 d\tau_2 d\tau_3 \chi_{\sigma, \sigma'}(\tau_1, \tau_2, \tau_3) e^{-i\nu\tau_1} e^{i(\omega-\nu')\tau_2} e^{-i(\omega-\nu)\tau_3} \quad (2.47)$$

respectively. Here, $\nu = \frac{\pi}{\beta}(2n+1)$ and $\nu' = \frac{\pi}{\beta}(2n'+1)$ denote fermionic Matsubara frequencies whereas $\omega = \frac{\pi}{\beta}2n$ denotes a bosonic Matsubara frequency (see Eq. 2.4). Both conventions are illustrated and contrasted with each other in Fig. 2.11. Since there exist relations for expressing one convention in terms of

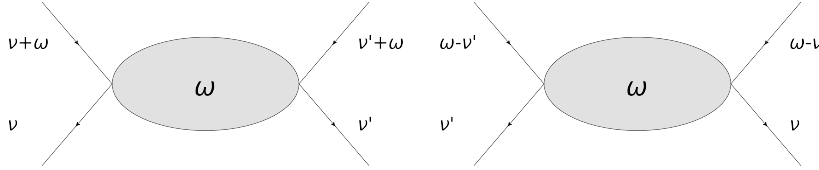


Figure 2.11: Illustration of particle-hole (left) and particle-particle (right) scattering convention according to [52].

the other one

$$\chi_{pp; \sigma, \sigma'}^{\nu, \nu', \omega} = \chi_{ph; \sigma, \sigma'}^{\nu, \nu', \omega - \nu - \nu'}, \quad (2.48)$$

one can stick to the particle-hole notation, which is therefore used mostly in this thesis.

Furthermore, it is useful to divide the general susceptibility into a part of bubble terms, which includes the independent propagation of two particles, and a part which stems from the explicit interaction among the two particles, i.e. the so called **vertex corrections**:

$$\chi_{\sigma, \sigma'}^{\nu, \nu', \omega} = \chi_0^{\nu, \nu', \omega} \delta_{\sigma\sigma'} - G_\sigma(\nu)G_\sigma(\nu + \omega)F_{\sigma, \sigma'}^{\nu, \nu', \omega}G_{\sigma'}(\nu')G_\sigma(\nu' + \omega) \quad (2.49)$$

with the (one-particle like) **bubble term**

$$\chi_0^{\nu, \nu', \omega} = -\beta G_\sigma(\nu)G_\sigma(\nu + \omega)\delta_{\nu\nu'} \quad (2.50)$$

The two terms are also illustrated diagrammatically in Fig. 2.12.

The second contribution, F , is called the **full vertex function** as it consists of all connected two-particle diagrams, and it can be physically interpreted as the scattering amplitude of two quasiparticles [26, 52].

$$\chi_{\sigma\sigma'}^{\nu\nu'\omega} = -\beta\delta_{\nu\nu'}\delta_{\sigma\sigma'} - \text{bubble diagram}$$

Figure 2.12: Illustration of the division of the general susceptibility into a bubble term and vertex corrections (taken from [52]).

2.4.2 Reducibility at the two-particle level and the Parquet equation

The concept of reducibility and irreducibility at the two-particle level is defined analogously to the one-particle level (see sec. 2.1.2): in fact, by simply extending the irreducibility definition of the self-energy diagrams at the one-particle level, one can say that all connected diagrams which cannot be separated in two parts by cutting **two** internal fermionic lines are “fully irreducible at the two-particle level” (this is the case, e.g. for the vertex function Λ shown in Fig. 2.13). However, when considering reducible diagrams the situation at this diagrammatic level is more subtle, because there are three different ways (often called **channels**) to establish such a cut, and, hence, a given diagram can be

1. reducible in the particle-particle channel (e.g., diagram Φ_{pp} in Fig. 2.13),
2. reducible in the transverse particle-hole channel (e.g., diagram Φ_{ph} in Fig. 2.13) and
3. reducible in the longitudinal particle-hole channel (e.g., diagram Φ_{ph}^- in Fig. 2.13).

In general, one can show¹¹ that a diagram is either **fully irreducible** (i.e. irreducible in every channel) or reducible in exactly one channel, so that a classification of every two-particle diagram appearing in F is possible via the so-called **parquet equation**:

$$F = \Lambda + \Phi_{pp} + \Phi_{ph} + \Phi_{ph}^- \quad (2.51)$$

where Λ denotes the **fully irreducible vertex** and the Φ_r denote the **reducible vertices in channel** $r = (pp, ph, \overline{ph})$. Lowest order examples for each class of these diagrams are depicted in Fig. 2.13.

2.4.3 The Bethe-Salpeter equation

A simpler, but important and more known way of dividing reducible and irreducible diagrams in one channel r and relating them with the full vertex is the

¹¹see reference 41 in [52]

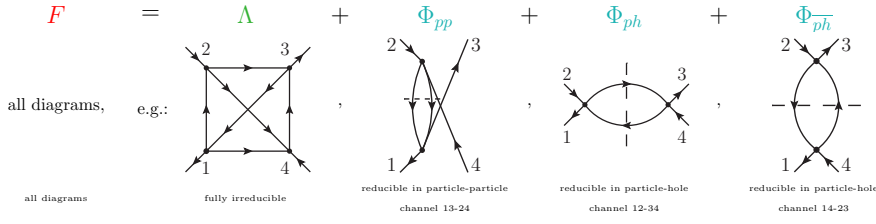


Figure 2.13: Visualization of the different parts of the Parquet equation (taken from [52]). Λ denotes the fully irreducible vertex and the Φ_r denote the reducible vertices in channel $r = (pp, ph, \bar{ph})$. Lowest order examples for each type of diagrams are shown.

following:

$$F = \Gamma_r + \Phi_r \quad (2.52)$$

where Γ_r denotes the (two-particle) **irreducible vertex in channel r** and Φ_r the corresponding reducible one. For instance, in Fig. 2.13 the diagrams on the right-hand side of the equation can be divided into “reducible in the particle hole-channel” (Φ_{ph}) and “irreducible in the particle-hole channel” (Λ , Φ_{pp} and $\Phi_{\bar{ph}}$):

$$F = \Lambda + \underbrace{\Phi_{pp} + \Phi_{\bar{ph}}}_{\Gamma_{ph}} + \Phi_{ph} \quad (2.53)$$

Expressing F via a Dyson-like equation one obtains the well-known **Bethe-Salpeter equation**

$$F = \Gamma_r + \int \Gamma_r G G F \quad (2.54)$$

where the integral is a compact way to indicate the summation over all internal degrees of freedom.

2.4.4 Spin-dependence of the two-particle quantities

As it is evident from the definitions in subsection 2.4.1, the spin dependence of the vertex functions can be reduced to the SU(2)-symmetric case, which will be always analysed here, there are three independent spin combinations: $\uparrow\uparrow, \uparrow\downarrow, \downarrow\downarrow$ (see also [52]). So with the three different channels $r = pp, ph, \bar{ph}$ of the irreducible vertex Γ_r there are only nine possible combinations, which can be reduced to four independent channels¹². These are called **density** or charge (d or c), **magnetic** or spin (m), **singlet** (s) and **triplet** (t) channels and are defined explicitly in the following way:

$$\Gamma_d^{\nu, \nu', \omega} = \Gamma_{ph, \uparrow\uparrow}^{\nu, \nu', \omega} + \Gamma_{ph, \uparrow\downarrow}^{\nu, \nu', \omega} \quad (2.55)$$

$$\Gamma_m^{\nu, \nu', \omega} = \Gamma_{ph, \uparrow\uparrow}^{\nu, \nu', \omega} - \Gamma_{ph, \uparrow\downarrow}^{\nu, \nu', \omega} \quad (2.56)$$

$$\Gamma_s^{\nu, \nu', \omega} = \Gamma_{pp, \uparrow\downarrow}^{\nu, \nu', \omega} - \Gamma_{pp, \downarrow\uparrow}^{\nu, \nu', \omega} \quad (2.57)$$

$$\Gamma_t^{\nu, \nu', \omega} = \Gamma_{pp, \uparrow\downarrow}^{\nu, \nu', \omega} + \Gamma_{pp, \downarrow\uparrow}^{\nu, \nu', \omega} \quad (2.58)$$

¹²by usage of the SU(2)-symmetry and so called crossing symmetry [52].

Here, σ, σ' and $\overline{\sigma, \sigma'}$ denote the spin channels for an arbitrary vertex \mathcal{V} determined by

$$\mathcal{V}_{\sigma, \sigma'} = \mathcal{V}_{\sigma, \sigma, \sigma', \sigma'} \quad (2.59)$$

$$\mathcal{V}_{\overline{\sigma, \sigma'}} = \mathcal{V}_{\sigma, \sigma', \sigma', \sigma} \quad (2.60)$$

Obviously, at the level of the fully irreducible vertex Λ and full vertex F only two of those channels are independent (e.g. $\uparrow\uparrow$ and $\uparrow\downarrow$).

2.4.5 Approximations at different vertex levels

Before discussing the new results obtained in this thesis, it is instructive to add some physical insight to the formal classification of the two-particle diagrams by analysing how some of the well-known approximation schemes of many-body theory can be obtained via approximating different two-particle quantities defined in the previous section. These approximations are summarized in table 2.1.

\mathcal{V}_r	Static ($\mathcal{V}_r = U$)	Dynamic, local ($\mathcal{V}_r = \mathcal{V}_r^{loc}$)
F	second order perturbation theory	
Γ_r	RPA, FLEX, pseudopotential parquet	Ladder D Γ A
Λ	parquet approximation (PA)	D Γ A

Table 2.1: Diagrammatic approximations at different vertex levels. $\mathcal{V}_r = F, \Gamma_r, \Lambda$ denotes the vertex which is replaced either with the static local interaction U or its corresponding dynamical but local counterpart $\mathcal{V}_r = \mathcal{V}_r^{loc}$.

Remaining at the shallow level of the full vertex F and replacing F with the static and local interaction U (e.g. in the Dyson-Schwinger equation of motion for the self-energy) one obviously obtains just the simple expressions of the second order perturbation theory.

Going one level deeper in the diagrammatics and replacing Γ_r with U in each channel, the calculated F will correspond to¹³ the random phase approximation (RPA) (see e.g. [25]), fluctuation exchange approximation (FLEX) [54, 55] and pseudopotential parquet approximation [5]. On the other hand, whereas substituting Γ_r with its (frequency dependent) local counterpart results in the ladder version of the D Γ A (also known as Moriyasque D Γ A [47, 56]), which has been used successfully for describing the pseudogap in the cuprates (2D) and determining the critical exponents of the Hubbard model in three dimensions [56].

¹³depending on how the substitution is technically done, see [52] for details

If, finally, one moves on to the deepest level of the diagrammatics, one can replace the fully irreducible vertex Λ by the bare interaction U : this corresponds to the so called parquet approximation [5, 57, 58]. Finally, if one substitutes the fully irreducible vertex with its (frequency-dependent) local counterpart, one arrives at the full non-perturbative description of the D Γ A [46].

Chapter 3

Results: Local two-particle vertex functions in DMFT

As discussed before, DMFT constitutes a very successful tool to analyse the local part of electronic correlation. For finite dimensional systems, however, the DMFT self-consistency is guaranteed at the one-particle level only (i.e. for the Green function and the self-energy). On the other hand, very important information is also enclosed in the two-particle local vertex functions of DMFT, as they are needed (i) for the calculation of momentum dependent response functions (i.e. susceptibilities $\chi(\vec{q})$) at the level of DMFT and (ii) for the diagrammatic extensions of DMFT. Only very recently (see [52]) the first systematic analysis of local two-particle vertex functions has been performed in DMFT. However, in that work the numerical restrictions of the exact diagonalization (ED) solver have prevented carrying out a complete physical interpretation of the two-particle vertex properties in relation to the phase-diagram of the Hubbard model and, hence, to the Mott metal-insulator transition. Here, by adopting a much more efficient impurity solver than ED, namely quantum Monte Carlo (QMC), those properties have been readily analysed in all interesting regions of the Hubbard model phase diagram. Furthermore, this algorithm is also extendible to (DCA) cluster calculations for the inclusion of (short-ranged) spatial correlations, which are necessary for the investigation of the momentum-dependence of the vertex quantities (see chapter 4). This chapter is structured in the following way: in section 3.1 the numerical results for the frequency dependence of the local vertex quantities are analysed. In section 3.2 the main structure of the irreducible vertex functions, i.e. their divergencies, are described for the first time along the whole phase diagram. Possible explanations and physical interpretations of these results are discussed in 3.3.

3.1 Frequency dependencies of the local two-particle quantities: DMFT results

Before illustrating the main outcome of the new QMC results for the frequency dependence of the local vertex functions in DMFT, a recapitulation of the results recently reported in [52] is carried out in subsection 3.1.1 and a compar-

ison with the results obtained here with the DMFT(QMC) algorithm is done in subsection 3.1.2.

3.1.1 Literature results in exact diagonalization

In the work by G. Rohringer et al. ([52]), the frequency structure calculations of the local two-particle quantities for the three-dimensional Hubbard model¹ have been mainly performed for an interaction strength of $U = 0.5$, which is small enough in order to compare those structures to perturbation theory, at an inverse temperature of $\beta = 26.0$ and at half-filling (i.e. the chemical potential is fixed to $\mu = \frac{U}{2}$). A selection of these results is displayed here in particle-hole notation and at zero bosonic frequency (though results for finite bosonic frequencies also exist). Note that, due to the particle-hole symmetry [52], at half-filling all local vertex quantities are purely real (see [52]).

Full vertex F

Fig. 3.1 shows the frequency dependence of the real parts of the local full vertex F , as defined in Eq. 2.49, in the density and magnetic channel respectively:

$$F_d^{\nu\nu'\omega} = F_{\uparrow\uparrow}^{\nu\nu'\omega} + F_{\uparrow\downarrow}^{\nu\nu'\omega} \quad (3.1)$$

$$F_m^{\nu\nu'\omega} = F_{\uparrow\uparrow}^{\nu\nu'\omega} - F_{\uparrow\downarrow}^{\nu\nu'\omega} \quad (3.2)$$

and the (trivial) lowest-order constant terms U or $-U$ respectively have been subtracted. Dark and light blue indicate negative values of this difference, whereas yellow, red and violet denotes positive ones and white is zero.

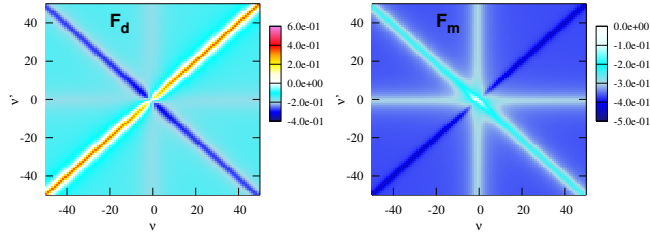
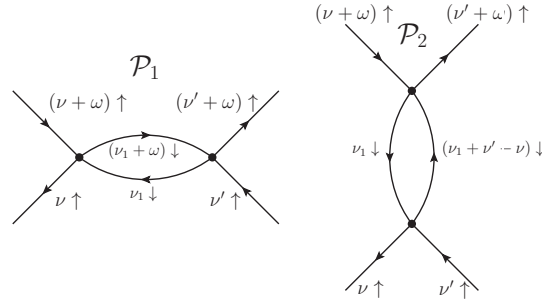
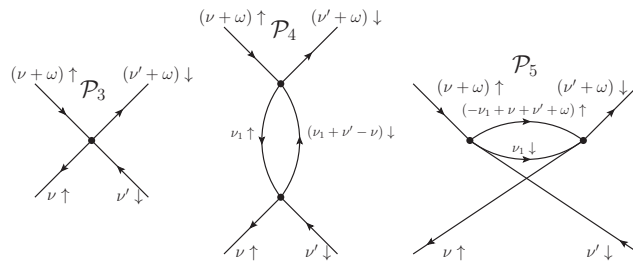


Figure 3.1: Frequency dependence on the fermionic Matsubara frequencies ν and ν' of the full vertex functions in the density (left, $F_d - U$) and magnetic (right, $F_m + U$) channel for vanishing bosonic frequency $\omega = 0$, $U = 0.5$, $\beta = 26.0$ and half filling (taken from [52]). Dark and light blue indicate negative values of this difference, whereas yellow, red and violet denotes positive ones and white is zero.

Following [52], one can easily trace the different features of the vertex functions by considering the lowest order perturbation diagrams which are shown in Fig. 3.2 for $F_{\uparrow\uparrow}$ and Fig. 3.3 for $F_{\uparrow\downarrow}$ respectively: From the analysis of Fig.

¹Note: Although the dimensionality of the Hubbard model used in [52] is not the same as the one of the implemented QMC algorithm in this work, the results can be still qualitatively compared, because the variances of the density of states, which is the essential parameter determining the kinetic energy scale in a DMFT calculation, have been adjusted to be equal. This corresponds to rescale all data with the energy scale $D = 4t$ for the two-dimensional and $D = 2\sqrt{6}t$ for the three-dimensional case.

Figure 3.2: Lowest order perturbation diagrams for $F_{\uparrow\uparrow}$ (taken from [52]).Figure 3.3: Lowest order perturbation diagrams for $F_{\uparrow\downarrow}$ (taken from [52]).

3.1 and the comparison with the lowest order perturbation diagrams of Fig. 3.2 and 3.3, one can easily identify and interpret the main frequency structures appearing in F :

- One observes a non-vanishing **constant background** present which stems from “bubble” diagrams which are independent from the two internal Matsubara frequencies ν and ν' like \mathcal{P}_1 in Fig. 3.2, i.e. from reducible contributions in the ph channel.
- The **main diagonal** (i.e. the enhanced scattering rate around $\nu = \nu'$) is the result of bubble diagrams which internally depend on the difference $\nu - \nu'$ like \mathcal{P}_2 in Fig. 3.2 or \mathcal{P}_4 in Fig. 3.3, i.e. from reducible contributions in the $\bar{p}\bar{h}$ channel.
- The **secondary diagonal** stems from enhanced scattering rates with total energies at the Fermi level, i.e. $\nu + \nu' = -\omega$, i.e. from reducible contributions in the pp channel. A corresponding diagram is \mathcal{P}_5 in Fig. 3.3.
- Finally one also observes a (less intense) **centred cross** structure that results from third-order perturbation diagrams [52].

While the identification of these principal structure in the vertex function F with the lowest-order perturbation theory diagram would be formally applicable in the weak-coupling limit only, quite remarkably it does not lose its validity even for larger values of U : In that case, of course, all the bubble contribution diagrams discussed here will be internally “corrected” by their corresponding vertex correction $\chi_{\text{bubble}} \rightarrow \chi$ [52]. Hence, even at larger values of U one can

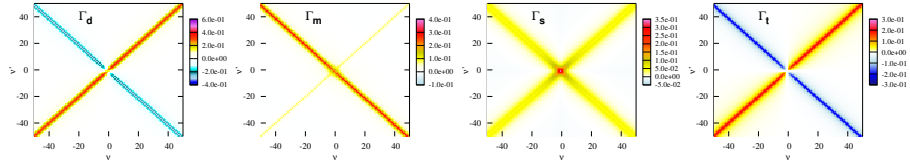


Figure 3.4: Frequency dependence on the fermionic Matsubara frequencies ν and ν' of the irreducible vertex functions in the density (first, $\Gamma_d - U$), magnetic (second, $\Gamma_m + U$), singlet (third, $\Gamma_s - 2U$) and triplet (fourth plot, Γ_t) channel for vanishing bosonic frequency $\omega = 0$, $U = 0.5$, $\beta = 26.0$ and half filling (taken from [52]). Dark and light blue indicate negative values of this difference, whereas yellow, red and violet denotes positive ones and white is zero.

understand that these principal structures are mainly generated by reducible processes in one of the different channels, as shown.

Irreducible vertices Γ in a given channel

Fig. 3.4 shows the frequency dependence of the real parts of the local irreducible vertices Γ in the density $\Gamma_d^{\nu\nu'\omega}$ and magnetic $\Gamma_m^{\nu\nu'\omega}$ (in particle-hole notation) and singlet $\Gamma_s^{\nu\nu'\omega}$ and triplet $\Gamma_t^{\nu\nu'\omega}$ channel in (particle-particle notation) respectively. Like for F the lowest-order constant terms U , $-U$ and $2U$ have been subtracted. Dark and light blue indicate negative values of this difference, whereas yellow, red and violet denote positive ones and white is zero.

On the basis of the observations in the case of the full vertex F , by repeating the same kind of analysis at a deeper level of the diagrammatics, one would expect that some of the features discussed for the full vertex F can be also found for the irreducible vertices, while others will be missing. In particular, by considering the frequency dependence of the irreducible vertex in each channel, one observes that the constant background and centred cross are missing in comparison to the full vertex in Fig. 3.1, because those structures are the result of contributions from reducible diagrams in the longitudinal channel, which are not included (per definition) in Γ_r . In contrast, the main and secondary diagonal survive², because for an irreducible vertex in channel r (Γ_r) these enhancements stem from reducible contributions of other channels than the selected one (r).

Fully irreducible vertex Λ

Finally, in Fig. 3.5 the frequency dependencies of the local fully irreducible vertex Λ in the density $\Lambda_d^{\nu\nu'\omega} = \Lambda_{\uparrow\uparrow}^{\nu\nu'\omega} + \Lambda_{\uparrow\downarrow}^{\nu\nu'\omega}$ and magnetic $\Lambda_m^{\nu\nu'\omega} = \Lambda_{\uparrow\uparrow}^{\nu\nu'\omega} - \Lambda_{\uparrow\downarrow}^{\nu\nu'\omega}$ channel are shown. The constant terms U and $-U$ have been subtracted. Also here, dark and light blue indicate negative values of this difference, whereas yellow, red and violet denotes positive ones and white is zero.

From the analysis of Fig. 3.5 one can note the following:

²As a side remark, one should note that the actual shapes of the “surviving” structures obviously depend on the notation adopted: for instance, in particle-particle notation one still retrieves the constant background and centred cross in the particle-particle channels, see [52].

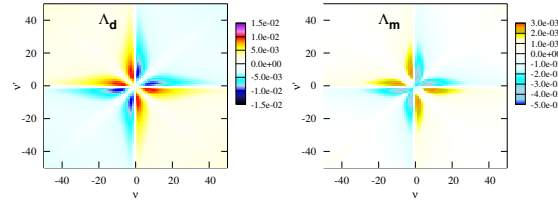


Figure 3.5: Frequency dependence on the fermionic Matsubara frequencies ν and ν' of the fully irreducible vertex functions in the density (left, $\Lambda_d - U$) and magnetic (right, $\Lambda_m + U$) channel for vanishing bosonic frequency $\omega = 0$, $U = 0.5$, $\beta = 26.0$ and half filling (taken from [52]). Dark and light blue indicate negative values of this difference, whereas yellow, red and violet denotes positive ones and white is zero.

1. All main frequency features discussed for F , which extended up to high frequencies, are missing as it should be, because Λ cannot contain any reducible contributions.
2. At low frequencies, however, one notes the formation of a significant frequency (butterfly-shaped) structure.
3. At high frequencies, Λ is always given by the constant contributions:

$$\Lambda_{d,m}^{\nu,\nu' \rightarrow \infty} \rightarrow \pm U.$$

These significant frequency features of the fully irreducible vertex Λ certainly influence also one-particle quantities derived from the fully irreducible vertex, e.g. the DMFT self-energy (see [52]), significantly. As discussed in section 2.3, the frequency structure of the fully irreducible vertex is of the utmost importance for one of the (non-cluster) diagrammatic extensions of DMFT, as it provides, e.g., the fundamental input for the D Γ A. As the low-frequency structure of Λ is not trivial and according to the (partial) analysis of [52] becomes quickly more pronounced as U increases, one also can pose the interesting question whether this fact also applies to the structure of the (non-local) quantity in momentum space. This important issue is discussed in chapter 4.

3.1.2 Comparison of ED and QMC results

The analysis of G. Rohringer and co-workers, whose results have been shown in subsection 3.1.1, is formally general, but numerically limited to selected cases due to the huge numerical effort by performing two-particle quantities in DMFT(ED). Much more efficient, as argued in subsection 2.2.2, is the usage of the (Hirsch-Fye) QMC method as impurity solver. Also, ED cannot be reasonably applied to cluster calculations as the DCA calculations, which had to be carried out for analysing the momentum dependence of the two-particle vertex functions in chapter 4. Considering these facts, the calculation of two-particle quantities has been implemented and integrated in an existing DCA-code of O. Gunnarsson, which uses Hirsch-Fye QMC as impurity solver. In this way, the calculations will not only allow for a more thorough investigation and interpretation of the frequency-dependence of the local vertex quantities of DMFT, but also (with a bigger effort) for analysing their non-local counterparts (in terms of their momentum-dependence, for instance) at the DCA level.

Before analysing in more detail the physics emerging from two-particle quantities, in this subsection the results obtained with DMFT(ED) presented in the previous section, are compared to the DMFT(QMC) results of this thesis at every diagrammatic level, in order to test the accuracy of the new QMC implementation and the numerics.

Fig. 3.6 shows the comparison of the general susceptibility χ in all four channels as results of DMFT(QMC) with DMFT(ED) used in [52] for the two-dimensional half-filled Hubbard model (with $D = 4t = 1$) in a significant case of intermediate coupling ($U = 1.5$, $\beta = 20.0$, $\omega = 0$ and $\nu' = \frac{\pi}{\beta}$).

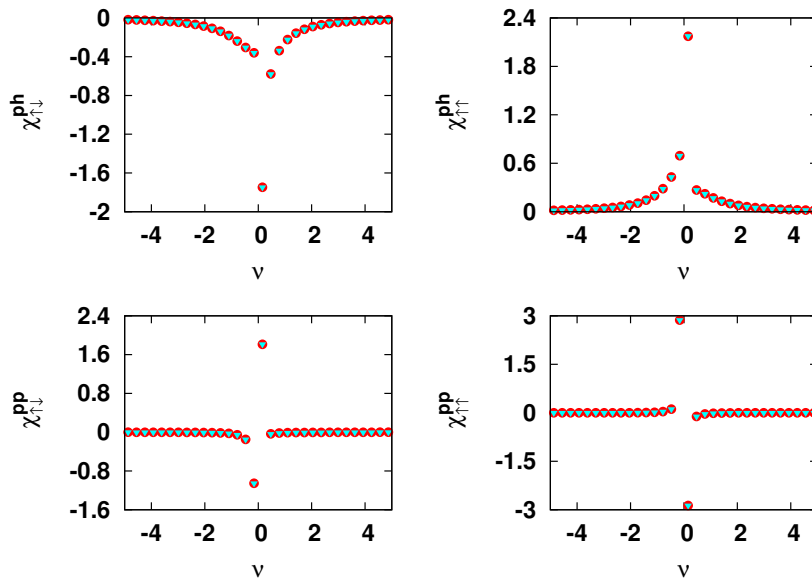


Figure 3.6: Comparison of the general susceptibility χ in all four channels as results of DMFT(QMC) (turquoise triangles) with DMFT(ED) (red points) as in [52] for $U = 1.5$, $\beta = 20.0$, $\omega = 0$ and $\nu' = \frac{\pi}{\beta}$.

Fig. 3.7 exhibits the comparison at the level of the irreducible vertex channels (i.e. after the inversion of the local Bethe-Salpeter equations) and Fig. 3.8 at the level of the fully irreducible vertex (i.e. after the inversion of the local parquet equations) for the same set of parameters. In all these figures, turquoise triangles indicate the DMFT(QMC) and red points the DMFT(ED) results. One can observe that the agreement of DMFT(QMC) with DMFT(ED) is very good at all levels of diagrammatics with the only exception of a slight deviation for a single low-energy point in the fully irreducible vertex. This behaviour is due to statistics of the QMC sampling scheme and the number of time slices in the Trotter discretization of Hirsch-Fye QMC and can be improved systematically acting on these two parameters of the QMC algorithm. Similar results have also been obtained for finite bosonic frequency and different fermionic frequency cuts, demonstrating the correctness of the DMFT(QMC) algorithm used in this thesis.

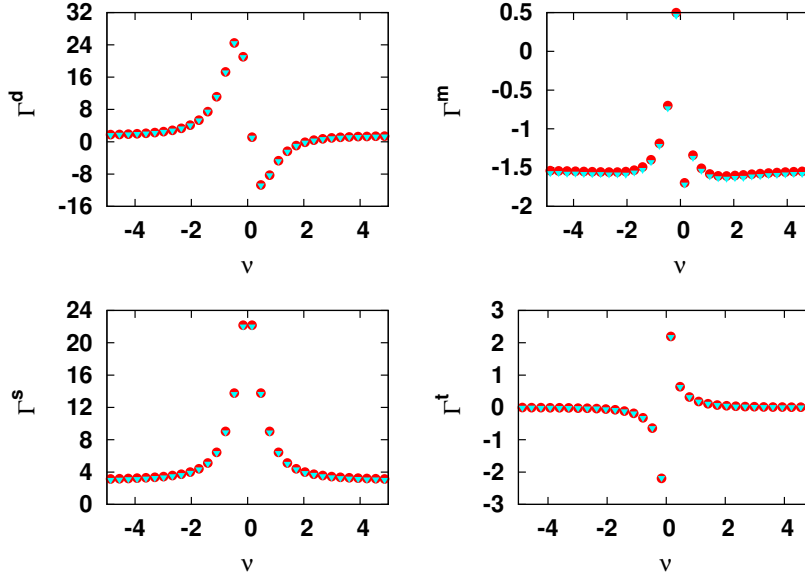


Figure 3.7: Comparison of irreducible vertices Γ in all four channels as results of DMFT(QMC) (turquoise triangles) with DMFT(ED) (red points) as in [52] for $U = 1.5$, $\beta = 20.0$, $\omega = 0$ and $\nu' = \frac{\pi}{\beta}$.

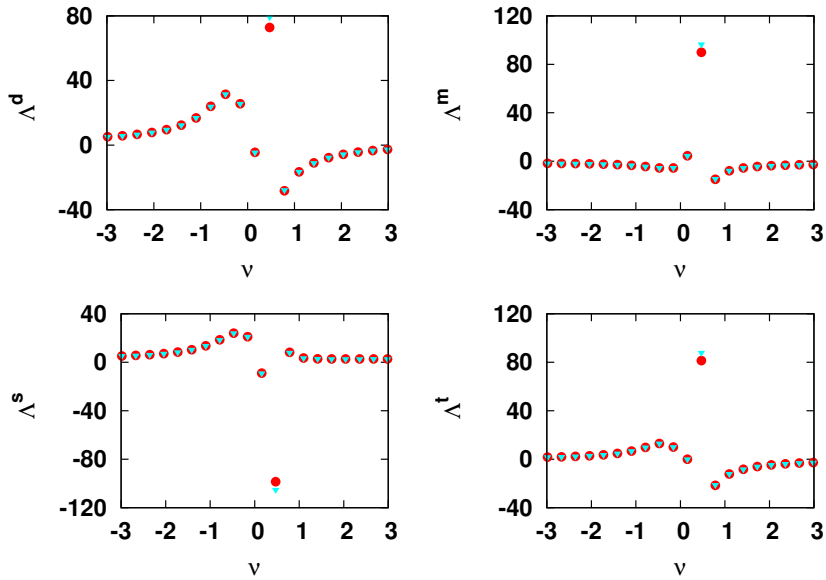


Figure 3.8: Comparison of the fully irreducible vertex Λ in all four channels as results of DMFT(QMC) (turquoise triangles) with DMFT(ED) (red points) as in [52] for $U = 1.5$, $\beta = 20.0$, $\omega = 0$ and $\nu' = \frac{\pi}{\beta}$.

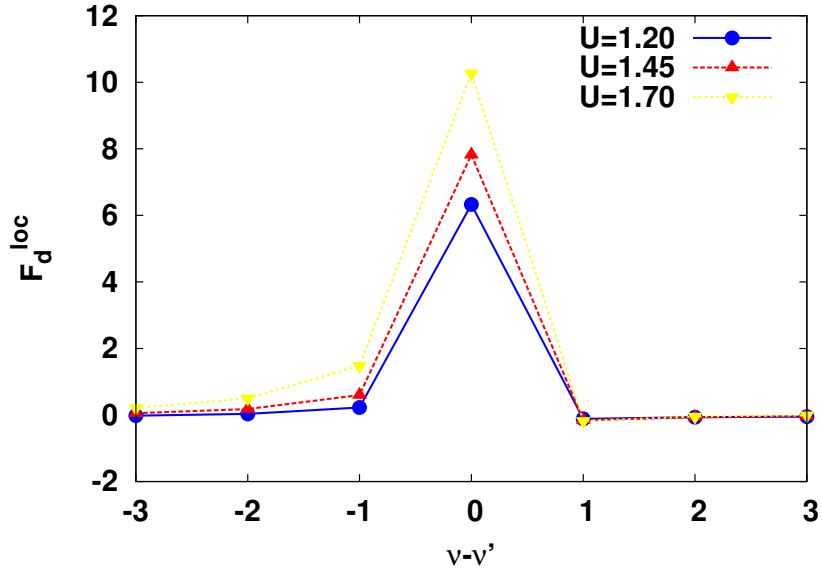


Figure 3.9: Enhancement of the main diagonal elements of the local density vertex F_d when approaching the MIT ($\beta = 10.0$, $\omega = 0$).

3.2 Divergencies of the local irreducible vertices and their physical interpretation

Going beyond the general observations of [52] reported in subsection 3.1.1 about the frequency dependence of the two-particle quantities in the weak-coupling regime of the phase diagram, one can pose the question, in which coupling region the strongest frequency dependence of the two-particle irreducible vertices is found. Considering the presence of a MIT in the centre of the phase diagram of the Hubbard model (and its intrinsic non-perturbative nature), it is quite logical to expect some hallmark of it also in the frequency structures of the vertex functions. In fact, in the following sections, data are presented, which clearly show that strong enhancements (or rather **divergencies**) of the frequency dependence of the vertex function exist, and that they are indeed related in several ways to the not perturbatively describable physics of the Mott metal-insulator transition.

3.2.1 Divergencies of the vertex at the Mott-transition

Analysing the evolution of the full vertex F at finite temperature with U , a progressive enhancement of the structure along the main diagonal at $\nu = \nu'$ can be observed in the metallic regime by increasing U , which becomes extremely pronounced approaching the MIT (see fig. 3.9 and also [52]). This behaviour indeed has to be expected for the full vertex F and partly also for the vertices Γ when approaching the MIT. As previously shown, in fact, the main diagonal structure (and also the constant background, not shown) is originated in scattering process reducible in the transverse particle-hole channel, contributing

at the most for processes on the Fermi surface, i.e. $\nu - \nu' = 0$. Specifically exploring the connection to perturbation theory, one can identify the following lowest order contributions to F_d and F_m (see [52] and Fig. 3.2 and 3.3):

$$\mathcal{P}_1 = +\frac{U^2}{\beta} \sum_{\nu_1} G(\nu_1)G(\nu_1 + \omega) = -U^2 \chi_{\text{bubble}}^{\text{ph},\uparrow\uparrow}(\omega) \quad (3.3)$$

$$\mathcal{P}_2 = -\frac{U^2}{\beta} \sum_{\nu_1} G(\nu_1)G(\nu_1 + \nu' - \nu) = U^2 \chi_{\text{bubble}}^{\text{ph},\uparrow\uparrow}(\nu' - \nu) \quad (3.4)$$

$$\mathcal{P}_3 = U \quad (3.5)$$

$$\mathcal{P}_4 = -\frac{U^2}{\beta} \sum_{\nu_1} G(\nu_1)G(\nu_1 + \nu' - \nu) = U^2 \chi_{\text{bubble}}^{\text{ph},\uparrow\downarrow}(\nu' - \nu) \quad (3.6)$$

$$\mathcal{P}_5 = -\frac{U^2}{\beta} \sum_{-\nu_1} G(-\nu_1)G(\nu_1 + \nu' + \nu + \omega) = U^2 \chi_{\text{bubble}}^{\text{pp},\uparrow\downarrow}(\omega + \nu' + \nu) \quad (3.7)$$

In these equations $\chi_{\text{bubble}}^{\text{ph}}(\omega)$ and $\chi_{\text{bubble}}^{\text{pp}}(\omega)$ denote the bubble parts of the generalized susceptibility, built with the DMFT Green functions but without vertex corrections in the particle-hole and particle-particle channel respectively, whereas $\chi^{\text{ph}}(\omega)$ and $\chi^{\text{pp}}(\omega)$ will be used to indicate the susceptibilities including vertex corrections.

Approaching the MIT, by increasing U one will correct all bubbles appearing (Eq. 3.3 to 3.7) with the corresponding vertex corrections ($\chi_{\text{bubble}} \rightarrow \chi$). Out of this it becomes clear, that all diagram contributions containing particle-hole susceptibilities (i.e. background and main diagonal) will be strongly enhanced³ in the proximity of the MIT, because, at $T = 0$, the (vertex corrected) spin-spin correlation function in the particle-hole channel (i.e. the **local magnetic susceptibility** $\chi_m(\omega = 0) = \chi_{\uparrow\uparrow}(\omega = 0) - \chi_{\uparrow\downarrow}(\omega = 0)$), see [59] and sec. VII/G of [30], which reveals a Fermi-liquid behaviour in the metallic phase and the formation of local moments in the insulating phase, **diverges at the MIT**, following Curie's law in the insulating phase (see Fig. 3.10). Hence, the enhancement of these frequency structures in F , which would even become divergent for $T \rightarrow 0$, can be easily understood as a direct hallmark of the MIT in the Hubbard-model. Note that, since the main diagonal structure is conserved (at least for specific channels, see subsection 3.1.1), also in the irreducible vertex Γ these specific structure will be strongly enhanced. This kind of "divergencies", instead, are not to be expected (and indeed are not found) in the fully irreducible vertex Λ as there no structure originating from reducible processes survives. Therefore, one can exclude a divergency of the fully irreducible vertex Λ as a reason of the enhancement of both the main diagonal and the constant background in F , because Λ is fully irreducible and thus does not contain those reducible contributions by definition.

3.2.2 Divergencies in the metallic phase

The divergencies of the vertex functions F and Γ (their background and main diagonal) are a direct manifest of the MIT, and, hence, their interpretation is

³Note: Obviously, these enhancement cannot stem from bubble terms $\chi_{\text{bubble}} \simeq GG$, because this product of two Green functions stays finite and would be even decreasing with U .

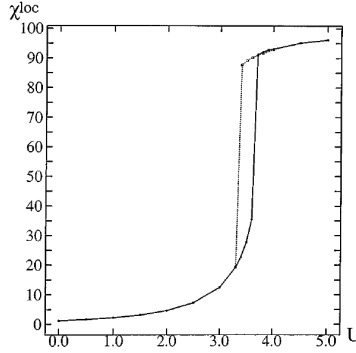


Figure 3.10: Divergency of the local spin susceptibility χ_{loc}^d as a function of $U\sqrt{2}/D$ for $\beta D/\sqrt{2} = 100$ at the first-order metal-insulator transition obtained by exact diagonalization (taken from [30]). In the limit $T \rightarrow 0$ one would observe a real divergence.

quite straightforward. However, quite surprisingly these divergencies are not the only ones. In fact, other, less expected, divergencies are found in one of the irreducible vertices Γ_r , namely for the one in the density channel. Specifically, following [60], the local irreducible density vertex $\Gamma_d^{\nu\nu'}(\omega)$ can be extracted via the inversion of the local Bethe-Salpeter equations:

$$\Gamma_d^{\nu\nu'}(\omega) = \left[\chi_d^{\nu\nu'} \right]_{\omega}^{-1} - \left[\chi_{\text{bubble}}^{\nu\nu'} \right]_{\omega}^{-1} \quad (3.8)$$

where the notation here emphasizes, that for every external (bosonic) frequency ω one obtains the value of the irreducible vertex $\Gamma_d^{\nu\nu'}(\omega)$ by inverting the corresponding generalized susceptibility as a matrix in the two fermionic Matsubara frequencies ν and ν' . By doing this, one observes that, while at small U one can perform the inversion without any particular problems, i.e. the eigenvalues of $\chi_d^{\nu\nu'}(\omega)$ have all the same (positive) sign, a **change of sign** of one of its eigenvalues is found for increasing U for the half-filled Hubbard model (see also the unpublished appendix of [58]). The situation evidently reflects itself in a corresponding enhancement (i.e. in a **divergence**) and a change of sign **of the low-frequency structures in $\Gamma_d^{\nu\nu'}(\omega)$** . In order to illustrate exactly how this happens, Fig. 3.11 shows the evolution of the irreducible density vertex (subtracted by the first order contribution of the perturbation series) with U at a constant inverse temperature of $\beta = 10.0$ and a bosonic Matsubara frequency of $\omega = 0$ with the same colour coding as in the previous sections.

Starting the analysis of Fig. 3.11 at $U = 1.20$, one can note that the “topology” of the structure of the irreducible vertex resembles in its shapes and colours (i.e. signs) the one of the weak-coupling structures discussed before (see also Fig. 3.4) and the very same main and secondary diagonal can be definitely identified in the density plot in the upper panel. Note also that this “topology” (including also the sign of the irreducible vertex) in the weak coupling regime can be accurately predicted by perturbation theory. In the lower panel, a cut of the density plot at $\nu' = \frac{\pi}{\beta}$ is presented (also marked by a dashed line in the density plot), from which one can recognize that the scale of the vertex in this

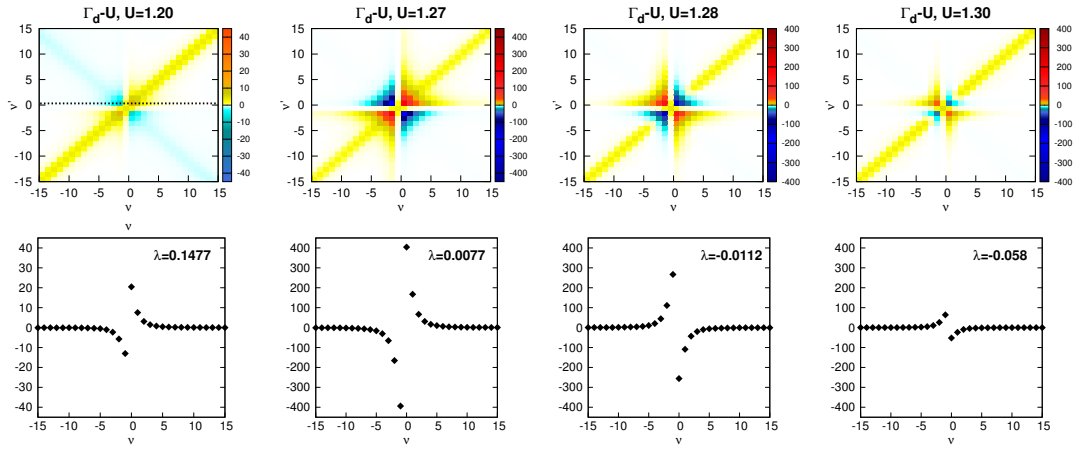


Figure 3.11: Density plots of the development of the local irreducible vertex in the density channel Γ_d with U for $\beta = 10.0$ and vanishing bosonic frequency $\omega = 0$ (upper row) and one-dimensional frequency cut at $\nu' = \frac{\pi}{\beta}$ of the corresponding data. The position of the cut is visualized by the black dashed line in the first plot at $U = 1.20$. One observes a change of sign of one of the eigenvalues of χ_d for a U value between $U = 1.27$ and $U = 1.28$. Note also the change of scale between the first and the other panels.

interaction region is about $\Gamma_d \approx 10 - 20$ at low fermionic Matsubara frequencies. Correspondingly, the minimum eigenvalue of the susceptibility in Eq. 3.8 divided by its (DMFT) bubble part⁴ ($\frac{\chi_d}{\chi_{\text{bubble}}}$), is positive: $\lambda = 0.1477$.

Increasing the interaction to $U = 1.27$ one immediately observes a huge enhancement of the vertex function Γ_d at low frequencies, where it can reach values of $\Gamma_d \approx 100 - 300$. Correspondingly, the magnitude of the lowest eigenvalue of χ_d decreases, while it still remains positive. The most abrupt change in the behaviour of Γ_d , however, happens at the passage to $U = 1.28$: one of the eigenvalues of χ_d changes sign between $U = 1.26$ and $U = 1.28$. This has the immediate consequence that the corresponding irreducible vertex Γ_d **“diverges”** at $U \approx 1.27$ (because the determinant of $\chi_d^{\nu, \nu'}$, which has to be inverted in order to retrieve Γ_d , vanishes, see Eq. 3.8). This behaviour can be directly visualized from the colour changes in the low-frequency regions of the density plot which turn over abruptly from red to blue and vice versa. Note that, despite of these dramatic changes of the vertex function Γ_d occurring at low frequencies, its “asymptotic” high frequency behaviour remains stable along this “transition”. The scale of the irreducible vertex and the magnitude (not its sign!) of the minimum eigenvector of $\frac{\chi_d}{\chi_{\text{bubble}}}$, however, is about the same as for $U = 1.27$.

Proceeding further to the higher value of $U = 1.30$ one can see that the frequency structure of the vertex function “calms down” in order to be alike the one before the “transition” (i.e. the absolute magnitudes of both irreducible ver-

⁴This quantity can be used for convenience instead of the “bare” eigenvalue of χ_d , because the bubble part always stays finite.

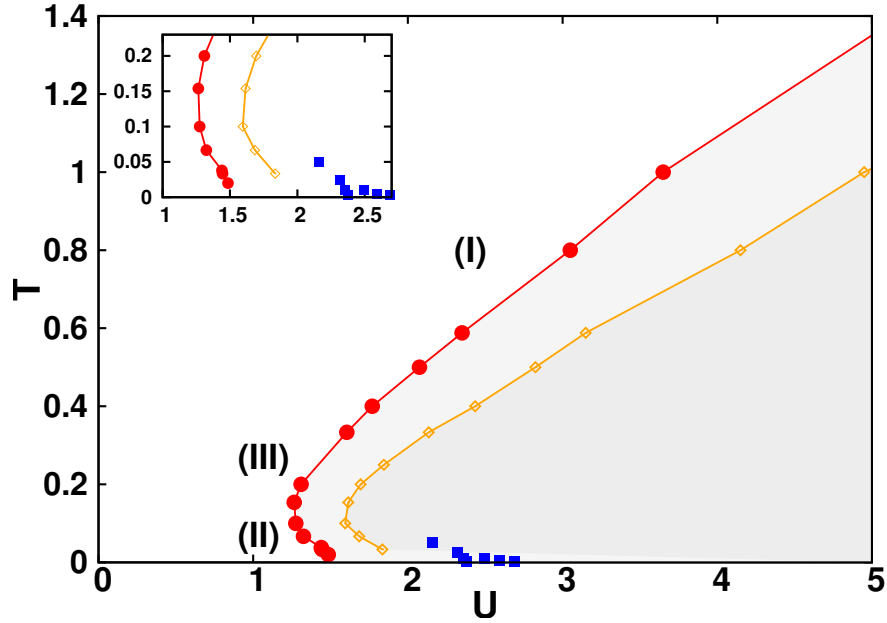


Figure 3.12: Phase diagram of the divergencies of the local irreducible vertices Γ_d (red solid line) and $\Gamma_{pp,\uparrow,\downarrow}$ (green solid line) in the two-dimensional Hubbard model. The Mott-Hubbard transition is indicated by blue points and taken, after proper units rescaling, from [17]. The inset shows a zoom of the low temperature region.

text and eigenvalue of $\frac{\chi_d}{\chi_{\text{bubble}}}$, although with opposite sign at low frequencies reflecting the fact that the sign of this eigenvalue keeps being negative.

To recapitulate, in addition to the standard divergencies of two-particle quantities **at the MIT** at $U_{c2} \approx 3$ as discussed in the previous section, also additional divergencies occur for the irreducible vertex function in the charge channel **before the MIT** is reached $\tilde{U} \approx 1.27 \ll U_{c2}$ (at least for this temperature $\beta = 10.0$) well in the metallic phase. The question, which immediately emerges and is therefore discussed in the following subsection, is, at which points of the $(T; U)$ plane (i.e. in the **phase diagram**) those divergencies can also be observed.

3.2.3 Phase diagram

According to the (unpublished) appendix of [61], the values of the interaction \tilde{U} where the divergence of the local irreducible charge vertex Γ_d happens should not depend on the temperature, i.e. that the **divergency line** should be a straight line in the phase diagram. However, according to the calculations in this thesis, seems not to be the case.

In the plot of the phase diagram in Fig. 3.12, the values of $(\tilde{T}; \tilde{U})$ for which a change of the sign of one of the eigenvalues of $\chi_d^{\nu\nu'}(\omega)$ occurs (red filled circles), are reported. For a better reference, the position of the MIT in the phase diagram is marked with blue dots (taken from [17]).

From the analysis of the $\tilde{T}(\tilde{U})$ curve, three different regions can be individuated:

- (I) For **high temperatures**, the value of U at which the divergency of Γ_d takes place, depends **linearly on the temperature**:

$$\tilde{U} \propto \tilde{T} \quad (3.9)$$

Because of Eq. 3.9 the high-temperature limit corresponds to a large interaction, i.e. to strong coupling. Hence, in region I one will have $U, T \gg t$ which would correspond, asymptotically, to the **atomic limit**. Therefore, the behaviour of this region can be verified and understood using analytical calculations (see subsection 3.3.1).

- (II) For **low temperatures** the curve bends towards the value $\tilde{U}(\tilde{T} \rightarrow 0) \simeq 1.5$, which is, however, a far lower value than the MIT transition interaction strengths of $U_{c1} \approx 2.35$ and $U_{c2} \approx 2.58$, while **“resembling” to some extent the shape of the MIT curve**.

- (III) In the **intermediate temperature** regime, the curve starts to bend, displaying a specific shape, which appears somehow to “avoid” the critical second-order endpoint of the MIT.

Considering the “peculiar” shape of the whole instability line, one would naturally be tempted to interpret it as a precursor of the MIT. However, for a precise and quantitative understanding, the following important points also have to be considered:

- While $\Gamma_d^{\nu\nu'}$ “diverges” at the instability line nothing happens to the corresponding thermodynamic local (charge) susceptibility.

$$\chi_d(\omega = 0) = \sum_{\nu, \nu'} \chi_d^{\nu\nu'}(\omega = 0) \quad (3.10)$$

which is simply smoothly decreasing with U for a fixed T in the whole phase diagram.

- At larger values of U , closer to the metal-insulator transition, one observes the occurrence of similar “instabilities” also in the particle-particle up-down channel (see again Fig. 3.12).
- The only irreducible vertex channel which seems to be unaffected is the particle-hole spin (i.e. the magnetic) channel.

In contrast to the divergencies directly related to the MIT via reducible processes of the local spin susceptibility discussed in the last section, the interpretation these new low-frequency features in the vertex functions is related to processes taking place at a deeper level of the diagrammatics and, therefore, not straightforward. Hence, in the next section, possible interpretations of these divergences are proposed and discussed in detail.

3.3 Possible interpretations of the divergencies of the local irreducible vertices

As the occurrence of vertex divergencies in the metallic phase has never been discussed in detail in previous works, and, in particular, no physical interpretation of these divergencies has been provided hitherto in the context of many body theory, a careful and step-by-step discussion of these new theoretical findings is needed here. Aiming on a structured analysis of the phase diagram of the divergencies of the local irreducible vertex Γ_d (i.e. the points (\tilde{T}, \tilde{U})), it is worth to start by recalling the three separate regions of the $\tilde{T}(\tilde{U})$ phase diagram:

- (I) For the high temperature region, \tilde{U} and \tilde{T} depend linearly on each other. This regime corresponds to the atomic limit ($t = 0$), which will be analysed in more detail in subsection 3.3.1.
- (II) For very low temperatures, where the $\tilde{T}(\tilde{U})$ curve bends and reaches a finite value at about $\tilde{U}(\tilde{T} = 0) \approx 1.5$. Here, quantum effects (grossly speaking, the interplay between potential and kinetic energy of the quantum system) prevails on temperature effects. For these effects one cannot rely on any analytical calculation, but some insight can be gained by considering the results of NRG calculations (see [34]) as well as analytical calculations within the coherent potential approximation (CPA), although not for the Hubbard model itself, but the Falicov-Kimball model. The physics of this region will be explored in subsections 3.3.2 and 3.3.3.
- (III) In the intermediate temperature regime, from the shape of the curve one can naturally suppose a gradual crossover taking place between the two regimes.

Furthermore, a suggestive link the vertex instability to non-equilibrium properties of the Hubbard model can be also examined, which is done in subsection 3.3.4.

3.3.1 The atomic limit

Starting point for the discussion of the vertex divergencies of the irreducible vertices is the study of the strong coupling/high temperature regime, i.e., large values of T and U . In this region of the phase diagram obviously only these two independent energy scales survive, and hence, the physics of this region will be governed by the ratio $\frac{U}{T}$. In fact, this corresponds in Fig. 3.13 to the region where the transition curve of Γ_d is simply a straight line for large values of U and T , i.e., the behaviour is given by a linear function $U = cT$.

Evidently, the exact value of the constant c can be obtained analytically from corresponding atomic limit calculations in the following way ([52, 62]): starting from the analytical expression for the full vertex F in the atomic limit (see appendix in [62]) one can show that the two column vectors $\chi_d^{\nu=\pi/\beta, \nu'(\omega=0)}$ and $\chi_d^{\nu=-\pi/\beta, \nu'(\omega=0)}$ of the $\chi_d^{\nu, \nu'(\omega=0)}$ -matrix become exactly equal (and hence the

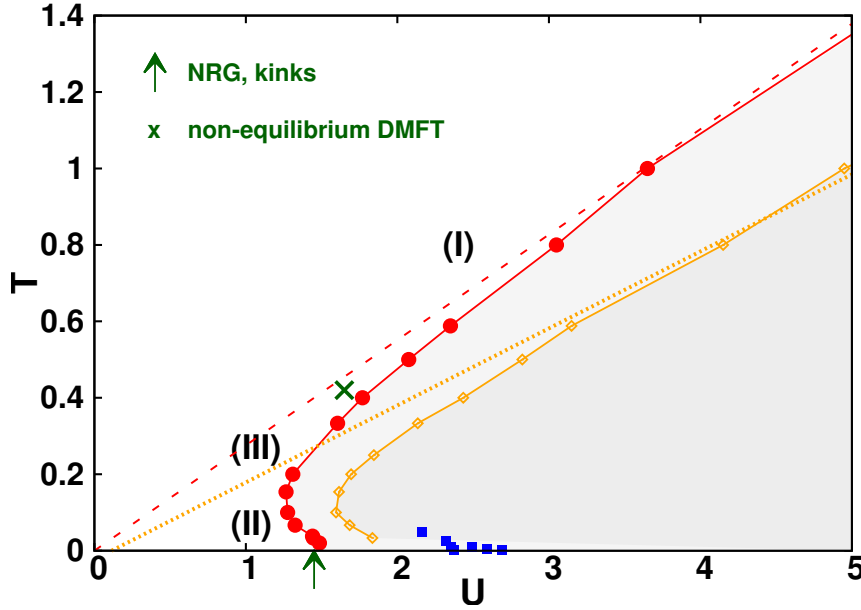


Figure 3.13: Phase diagram of the divergencies of the local irreducible vertices Γ_d (red solid line) and $\Gamma_{pp,\uparrow,\downarrow}$ (green solid line) in the two-dimensional Hubbard model. The Mott-Hubbard transition is indicated by blue points and taken from [17]. The high temperature (i.e. strong coupling or atomic) behaviour is extrapolated by a linear function (plotted with red and green dashed lines). The interaction value, where the shape of the DMFT(NRG) spectral function changes at $T = 0$ (see [64]) is indicated by a dark-green arrow. The point of the “dynamical transition” of the non-equilibrium DMFT calculations of the Hubbard model calculated by [65] is shown as a dark-green cross.

matrix $\chi_d^{\nu,\nu'(\omega=0)}$ becomes singular) for a value of

$$\frac{U}{T} = U\beta = \frac{2\pi}{\sqrt{3}} \quad (3.11)$$

[63]. More specifically, one can also note that the eigenvector which corresponds to the exactly vanishing eigenvalue $\lambda = 0$ of χ_d has a very peculiar structure, namely

$$E_{\lambda=0,d}^{\nu} = \frac{1}{\sqrt{2}}(\delta_{\nu,1} - \delta_{\nu,-1}). \quad (3.12)$$

Quite remarkably, the exact result of Eq. 3.11 can be directly connected to region (I) in the phase diagram of Fig. 3.13, as a (almost perfect) linear relation between \tilde{U} and \tilde{T} with the same proportionality coefficient $\frac{2\pi}{\sqrt{3}}$ can also be observed for the case of a finite bandwidth (see Fig. 3.13). In fact, the instability curve of Γ_d of Fig. 3.13 can be well described by the atomic limit result Eq. 3.11 in a quite large region of the phase diagram, e.g. down to values of $U \approx 2.0$ (i.e. U equals the bandwidth) and $T \approx 0.5$. Correspondingly, one also observes that the structure of the eigenvector $E_{\lambda=0,d}^{\nu}$ in this regime of the U/T -phase diagram resembles to a large extent that of the atomic limit (see Fig. 3.14): it consists mainly of two peaks at the lowest (positive and negative) Matsubara

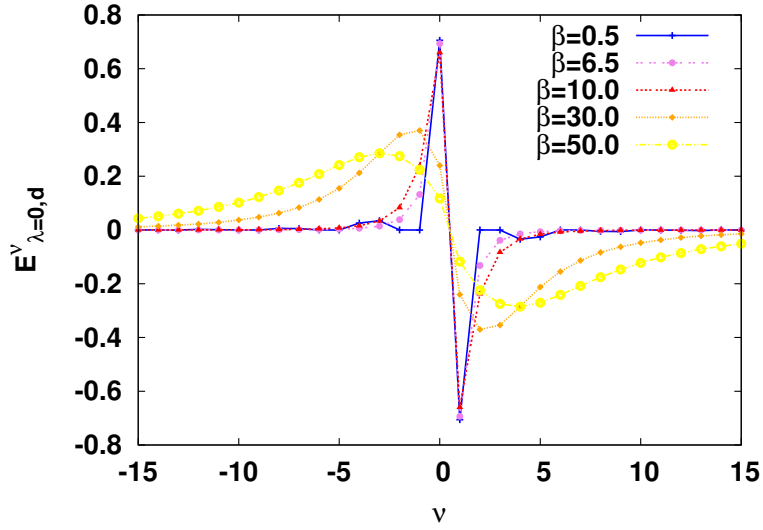


Figure 3.14: Evolution of the eigenvector $E_{\lambda=0,d}^{\nu}$ corresponding to the eigenvalue which changed sign, i.e. the closest to $\lambda = 0$ along the separation line of Γ_d in the phase diagram Fig. 3.13. This result can be directly compared to the analytic expression of the atomic limit in Eq. 3.12.

frequency.

However, one cannot expect that the physics of the atomic limit would also be sufficient to explain the observed results of the low-temperature metallic regions (II) and (III). And, indeed, the situation gradually changes when approaching lower values of U and T . At a value of $T \approx 0.5$ one observes deviations from the high- T linear behaviour of Eq. 3.11 with a bending of the curve towards higher U values in the phase diagram. The minimal \tilde{U} value is reached between $T \approx 0.15$ and $T \approx 0.10$. For even lower temperature ($T \lesssim 0.10$), as mentioned in section 3.2.3, the shape of the transition curve seems to be “affected” by the presence of the MIT, which is located, however, at much larger U .

Similarly, as for the transition curve itself, one observes a qualitative change in the structure of the eigenvector $E_{\lambda=0,d}^{\nu}$, when going from high to low U and T values. While in the atomic limit this eigenvector consists only of two delta-like peaks at the lowest (positive and negative) Matsubara frequencies, in the low-temperature regime this structure becomes much richer in the sense that the weight of the (normalized) eigenvectors corresponding to the zero eigenvalue $\lambda = 0$ is distributed among many Matsubara frequencies (see Fig. 3.14).

A possible interpretation of the interplay between these two energy scales is that in the high- U and high- T regime the physics is mainly controlled by $\frac{U}{T}$, while, when approaching lower temperatures such as $T \approx 0.10$, a third energy scale, i.e. the kinetic energy parameter t , also starts to play a crucial role. In this situation, quantum fluctuations will have very important effects, especially in the limit of $T \rightarrow 0$.

3.3.2 NRG calculations for zero temperature and kinks in the specific heat

The understanding of the region (II) of the phase diagram where quantum fluctuations are predominant is of course more challenging, because the relation with the analytical results of the atomic limit loses its validity. In particular, one can consider the results for inspecting the evolution of the spectral function of the half-filled Hubbard model with the interaction U (see for instance Fig. 3.15 from [64] for a hypercubic lattice⁵. The spectrum has been calculated with DMFT(NRG) for zero temperature. Note that the unit convention in this figure differs from that used in this thesis: $U_{\text{thesis}} = \frac{2.9}{4}U_{\text{NRG}}$). In agreement with the general DMFT description of the MIT (see subsection 3.2.1), the DMFT(NRG) data display three different shapes:

1. In the weak coupling regime (up to $U \approx 1.45$), a **quasiparticle peak** is present, which is accompanied by two plateaus or **shoulders** (as precursors of the Hubbard subbands).
2. At intermediate coupling (from $U \approx 1.45$ to $U \approx 2.9$), a **three-peak structure** with two local minima or **dips** is evident.
3. At strong coupling (from $U \approx 2.9$ on), only two well separated (and incoherent) **Hubbard bands** contribute to the spectrum.

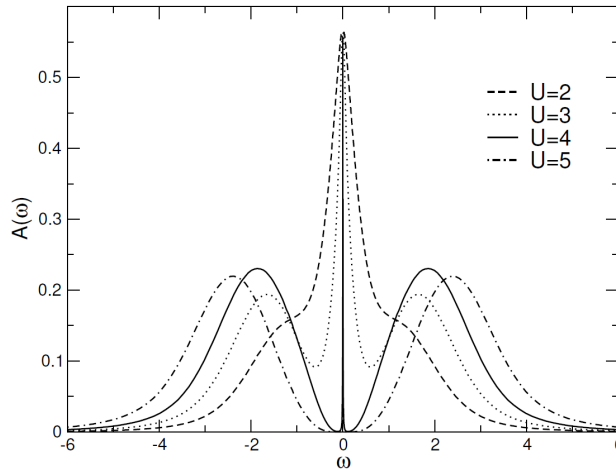


Figure 3.15: Spectral functions calculated DMFT(NRG) for the hypercubic Hubbard model for $U = 2, 3, 4, 5$ which corresponds to $U = 1.45, 2.18, 2.9, 3.63$ in units of this thesis (taken from [64]).

The physical importance of the change of the shape of the spectral function lies in the fact, that it is possible to demonstrate analytically, that the occurrence of dips immediately leads to **kinks in the electronic self-energy** [66] and, as a natural byproduct, also in the electronic specific heat [67]. Now, if one records

⁵These results can be quantitatively compared by fixing the scale D . However, small deviations may occur.

the interaction values U^* for which the $T = 0$ DMFT(NRG) spectral function starts to display the peculiar three peak structure, this point lies in the region of the most plausible extrapolation of the vertex divergency line to $T = 0$ (see Fig. 3.13). This suggests, that the separation of the Hubbard subbands from the quasiparticle peak (as well as the related appearance of the kinks) and the divergency of the irreducible charge vertex may be related and supports the interpretation of the vertex divergencies as first precursors of the MIT in the DMFT phase diagrams of the Hubbard model.

3.3.3 Coherent potential approximation for the Falicov-Kimball model

While the comparison with other numerical data is often very suggestive, it is important, whenever possible, to support it by analytical results. While this is not possible within the Hubbard model in this regime, significant insight can be gained by considering a simplified version of it, namely the Falicov-Kimball model, as a divergent precursor of the Mott-Hubbard transition can also be observed in this model, which includes itinerant and localized spins and can be solved in a semi-analytical way [68, 69, 63]. The coherent potential approximation (CPA) becomes exact within the Falicov-Kimball model and the self-energy at strong coupling approaches the one of the Hubbard model. However, this is not true for vertex functions. According to a recent work performed in collaboration with Prof. S. Ciuchi (Università degli Studi de l'Aquila) [63], in the Falicov-Kimball model the irreducible vertex in the density channel for $\omega \neq 0$ can be represented by

$$\Gamma_d^{\nu\nu'\omega} = \delta_{\nu,\nu'}\beta \frac{\Sigma(\nu) - \Sigma(\nu + \omega)}{G(\nu) - G(\nu + \omega)} \quad (3.13)$$

which is equal to the derivative $\frac{d\Sigma}{dG}$ for $\omega \rightarrow 0$ and the Bethe lattice

$$\Gamma_d^{\nu\nu'\omega \rightarrow 0} = \delta_{\nu,\nu'}\beta \frac{1}{2\text{Im}(G)^2(\nu)} \left(\frac{1}{\sqrt{1 - U^2\text{Im}(G)^2(\nu)}} - 1 \right) \quad (3.14)$$

so that a divergency occurs at

$$U^2\text{Im}(G)^2(\nu) = 1.$$

At low temperature $\text{Im}(\Sigma)(\nu) \simeq -\frac{U}{2}$, so that the condition for the appearance of a divergency reads

$$\frac{|U|}{D} = \frac{1}{\sqrt{2}},$$

where D is the bandwidth of the Falicov-Kimball model. While this result cannot be directly quantitatively compared to the the Hubbard model (and, hence, directly inserted in its phase diagram), from a qualitative point of view this analytical finding strongly supports the interpretation of the low-frequency divergence of Γ_d as a precursor of the MIT, if one also considers that the MIT in the Falicov-Kimball model corresponds to the complete separations of the Hubbard bands and is achieved much "later" at $\frac{U}{D} = 1$.

3.3.4 A link to non-equilibrium properties of the Hubbard model

Even more difficult than the interpretation of the low-frequency divergencies of Γ_d in the extreme regions of $T \rightarrow \infty$ (I) and $T \rightarrow 0$ (II) is the one of the intermediate region (III), which appears as a smooth connection between the physics of (I) and (II). However, quite remarkably, precisely in this region one of the most intriguing connection between the instability line and the underlying physics of the Hubbard model is found. Specifically, the suggestive "link" is provided by the comparison with the results of **non-equilibrium DMFT** [70, 65]. The authors of [70, 65] applied an interaction quench in non-equilibrium DMFT treatment⁶ for the half-filled Hubbard model at $T = 0$: This means that at time $t = 0$ they abruptly switched on the interaction U in the former non-interacting system, which is then left isolated and free to relax. As the system is isolated, one can assign an "effective temperature" T_{eff} to the system via its total energy E_{tot} :

$$E_{\text{tot}}(t) = E_{\text{tot}}(0) = \frac{\text{Tr}(H e^{-H/T_{\text{eff}}})}{\text{Tr}(e^{-H/T_{\text{eff}}})}, \quad (3.15)$$

where H is the system's Hamiltonian. Afterwards, the system's one-particle quantities are calculated.

Considering the example of the evolution with time t of the momentum distribution $n(\epsilon, t)$ in Fig. 3.16 (note that the units of interaction and temperature used in [65] differ from the ones used in this thesis: $U_{\text{thesis}} = \frac{1}{2}U_{\text{non-eq.}}$, analogously for the temperature), one can immediately separate three different kinds of behaviour of the thermalization process (for a detailed discussion see [65]):

- a) In the **weak-coupling** regime, the momentum distribution evolves towards a non-thermalised distribution, which slowly changes in time, so that a "prethermalization plateau" builds up.
- b) For an interaction of $U = 3.3$ and $T_{\text{eff}} = 0.84$ (which corresponds to $U = 1.65$ and $T_{\text{eff}} = 0.42$ in the units used in this thesis), a **rapid thermalization** takes place, without a prethermalization plateau or collapse-and-revival oscillations (see c)). Calculations in [65] show, that a finite width of this crossover cannot be observed, what suggests that there is a single "dynamical transition point" in the Hubbard model.
- c) In the **strong-coupling** regime, the relaxation is characterised by revival oscillations with periodicity of $\frac{2\pi}{U}$ and a damped collapse ("collapse-and-revival oscillations"). The momentum distribution oscillates around a non-thermal distribution.

Now, the interesting fact regarding the link between the divergence of the irreducible charge vertex and this non-equilibrium behaviour of the Hubbard model is, that the transition from weak to strong coupling (with respect to the qualitative change of behaviour of the system under an interaction quench) takes place nearly exactly at the divergency line of the irreducible charge vertex, see Fig. 3.13 for the single choice of temperature $T_{\text{eff}} = 0.84$ ($T_{\text{eff}} = 0.42$ in

⁶The method used therein is called Keldysh formalism (see e.g. [18]).

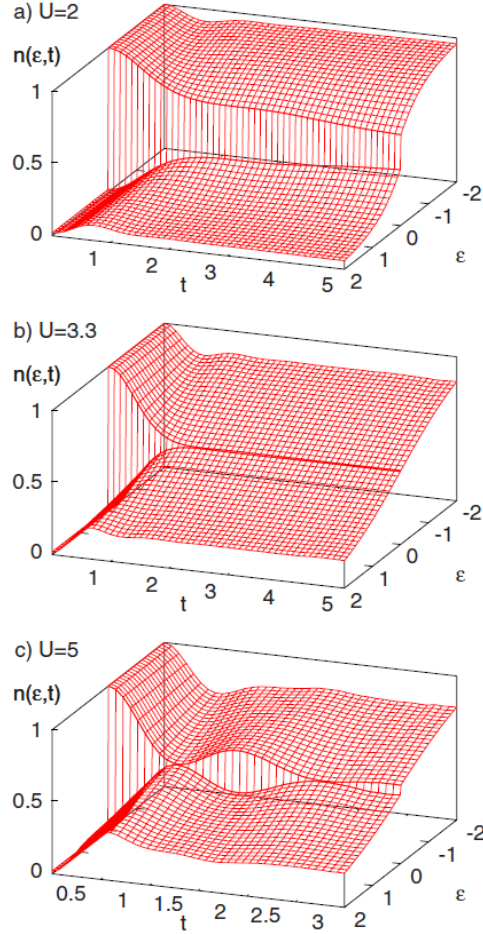


Figure 3.16: Momentum distribution after an interaction quench in the half-filled Hubbard model from the non-interacting ground state to interaction $U = 2$ (a), $U = 3.3$ (b) and $U = 5$ (c) (taken from [65]). The interaction values of [65] correspond to $U = 1.0$ (a), $U = 1.65$ (b) and $U = 2.5$ in units of this thesis.

units of this thesis) in [65]. This could indicate a connection between the divergency of the low-frequency structure of the local irreducible vertex and the non-equilibrium dynamics of the Hubbard model. However, to be sure that such a link really is present, further equilibrium and non-equilibrium calculations and investigations have to be performed for a broader range of parameters.

3.4 Summary of the local results

To recapitulate, strong frequency dependencies of both the full and the irreducible local vertices have been found in the DMFT(QMC) analysis: the ver-

tices F and Γ present evident enhancements for the background (F) and along the main diagonal ($\nu = \nu'$ for F and Γ), which become largest at the MIT and are directly related to the divergency of the local spin susceptibility $\chi_m^{loc}(\omega = 0)$ at $T = 0$ at the MIT. Moreover, and quite more surprisingly, other divergencies occur at low frequency for the irreducible vertex in the density channel much before the MIT is reached, i.e. in the metallic phase. While the physical understanding of these divergencies is still an open issue, many indications support the interpretation of such a low frequency divergency as a first non-perturbative precursor of the MIT at the two-particle level. If this is true, the inclusion of these enhanced frequency dependencies at the two-particle level (as in D Γ A and DF) would be essential for including the local physics beyond DMFT in a correct and fully non-perturbative way. Related to this, but from a more theoretical point of view, one can also observe that from the structure of the parquet equations 2.51, it is evident that, if only one of the irreducible vertices diverges, also the fully irreducible vertex Λ has to be divergent.

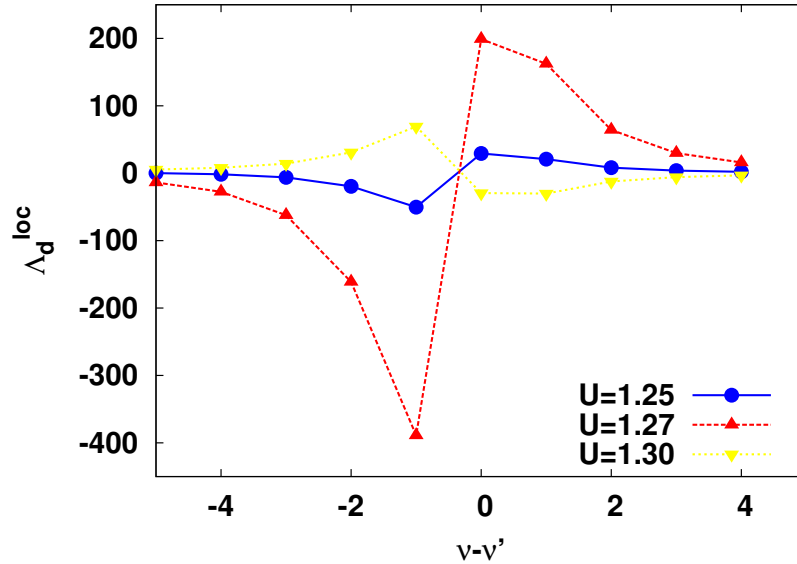


Figure 3.17: Enhancement of the local fully irreducible vertex Λ_d^{loc} when approaching the divergence of Γ_d^{loc} at an inverse temperature of $\beta = 10.0$.

In fact, one indeed observes that also Λ presents a significant (non-trivial) low-frequency dependence as can be seen in Fig. 3.17, where a specific frequency cut of the local fully irreducible vertex Λ_d^{loc} is shown at $\beta = 10.0$ when approaching the divergence of Γ_d^{loc} . This, evidently, might result as very important for the D Γ A, for which the fully local irreducible vertex in the intermediate interaction region serves as fundamental input parameter.

The strong frequency dependence of the fully irreducible vertex quite naturally raises the question whether an analogously strong **momentum dependence** of this fundamental quantity can be observed when including non-local spatial correlations beyond DMFT, which is studied in the following chapter by means

of the dynamical cluster approximation.

Chapter 4

Results: Dynamical cluster approximation for the vertex functions

Up to this point of the thesis, only local two-particle quantities have been analysed by means of DMFT calculations. However, because of the significant frequency dependence of these quantities, one can immediately raise the question, whether equally strong dependencies also appear in momentum-space, i.e. up to what extent these vertex functions depend on an internal momentum vector \vec{k} , when going beyond the DMFT approximation. This question is of the utmost relevance for diagrammatic extensions of DMFT such as the $D\Gamma A^1$, as well as for comparison between theory and experiment. This chapter is, hence, devoted to the analysis of the momentum dependence of vertex functions at every diagrammatic level. This is done by means of the dynamical cluster approximation (DCA), which allows to include systematically short-range spatial correlations within the size of the cluster considered (see subsection 2.3.1). The chapter is structured as follows: in section 4.1 existing DCA results for the momentum dependence of vertex functions for one specific set of parameters are presented, in section 4.2 perturbation theory calculations of the two-particle quantities for the case of weak coupling are reported and, finally, in section 4.3 DCA results for the vertex functions at all diagrammatic levels are presented and compared to perturbation theory in the weak-coupling regime and to DMFT in the intermediate coupling regime.

While results for the two-particle local vertices of DMFT have been reported sporadically in the literature (see e.g. [52] and references therein), when analysing the momentum dependence of the vertex functions beyond DMFT, one moves onto an almost unexplored ground (see, mainly for the generalized susceptibilities, [71]). Hence, it is much more difficult here to benchmark the new results of this chapter with previous existing ones. Therefore, after having briefly illustrated one of the (almost unique) exceptions of existing DCA results for the fully irreducible two-particle vertex functions in the next section, in Sec.

¹since the $D\Gamma A$ relies on the assumption, that the fully irreducible vertex Λ is purely local and, hence, independent of the momentum.

4.2 also perturbations theory results for all kind of vertices are presented and discussed. This preliminary analysis will provide a first benchmark to test and understand the calculations within the full DCA scheme presented, eventually, in Sec. 4.3.

4.1 An existing DCA calculation of vertex quantities

As mentioned above, hitherto a structured set of calculations of the momentum-dependence of two-particle quantities up to the level of the fully irreducible vertex Λ has not been performed. In this respect, however, one of the (almost unique) exceptions is represented by a specific DCA calculation, which has been performed in the parameter regime most important for the high- T_C superconductors of the cuprate family by [72]. Getting more specific, this calculation has been done for the two-dimensional Hubbard model on a DCA cluster with 24 sites for an average site occupancy of $\langle n_i \rangle = 0.85$ (i.e. a hole-doping of 15%) and a Hubbard interaction to hopping amplitude ratio of $\frac{U}{t} = 4$ (i.e. $U = 1.0$ in the units of this thesis). The two internal fermionic Matsubara frequencies are set to $\nu = \nu' = \frac{\pi}{\beta}$ and the first internal momentum is fixed to $k = (\pi, 0)$. According to the plot of the fully irreducible vertex function $\Lambda_{\uparrow\downarrow}$ from

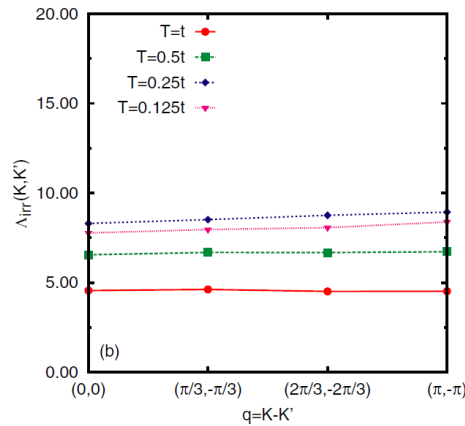


Figure 4.1: Momentum dependence of the fully irreducible vertex Λ for the two-dimensional Hubbard model with $\langle n_i \rangle = 0.85$ and an Hubbard interaction to hopping amplitude ratio of $\frac{U}{t} = 4$ for several temperature values as a function of the momentum transfer $q = k - k'$ (taken from [72]). In this calculation, Λ seems to be almost independent of the momentum.

[72] shown in Fig. 4.1, the fully irreducible vertex seems to be independent of the momentum transfer, which is indicated by a flat distribution in momentum space. This specific shape of the distribution of Λ in momentum space would represent a strong support of the dynamical vertex approximation D Γ A, which assumes that exactly this quantity is purely local (i.e. momentum independent). Furthermore, in perfect agreement with the D Γ A assumptions, the corresponding two-particle vertex functions with a less degree of irreducibility

(e.g. Γ) are found [72] to be strongly dependent on the momentum.

However, the studies in [72], while suggesting that the D Γ A would represent a very accurate approximation in the parameter regime of the cuprates, does not allow to draw general conclusions about the overall magnitude of the \vec{k} -dependence of the fully irreducible vertex, e.g. in two dimensions. More specifically, aiming at a systematic analysis of this problem (at least in two dimensions), it makes sense to start considering the case in which the strongest spatial correlations are expected (i.e. the most problematic case for D Γ A), which corresponds to the half-filling condition $\langle n_i \rangle = 1.00$. This should be examined in more detail as well as a general dependence of the vertex quantities on U should be investigated. Therefore, in this chapter DCA calculations for a two-dimensional 4-site cluster at half-filling are presented and discussed.

As, at the best of the knowledge of the author, no previous calculation (at least for the fully irreducible vertex) to compare with is available in the literature, in the following section perturbation theory calculations at lowest orders for the (non-local) vertex functions F , Γ and Λ are performed. These will represent an important benchmark for the DCA results discussed in the last section.

4.2 Perturbation theory of non-local two-particle quantities

In order to set up a reference for checking the validity of the implemented calculation scheme of non-local two-particle quantities, an approximation of those can be obtained (in the case of weak-coupling) by performing standard perturbation theory [26, 73].

Considering two-particle quantities, **generalized indices** that combine frequency and momentum indices are useful. For the fermionic case, they are defined as

$$\nu, k \rightarrow K = (\nu, k), \quad (4.1)$$

whereas for the bosonic case one has

$$\omega, q \rightarrow Q = (\omega, q) \quad (4.2)$$

so that e.g. the full dependence of the full vertex in the density channel on the internal and external frequencies and momenta can be compactly written as

$$F_{d;k,k',q}^{\nu,\nu',\omega} \rightarrow F_d^{K,K',Q} \quad (4.3)$$

One should also note, that the perturbation series at the level of cluster quantities (e.g. in a DCA calculation) has to be performed in terms of a **cluster-renormalized interaction** $\frac{U}{N_c}$ [73] rather than the bare interaction U in order to be able to compare those perturbation theory results to the ones obtained via the Bethe-Salpeter equations and the normalization typically adopted in DCA. In the following, low order perturbation theory results are presented, obtained by inserting an input Green function of a DCA calculation parametrized

by $N_c = 4$, $\beta = 10.0$ and $U = 0.5$ (i.e. weak-coupling) in the lowest-order Feynman diagram for each vertex. The cluster sites used in momentum space are shown in table 4.1.

index	$k = (k_x, k_y)$
1	(π, π)
2	$(\pi, 0)$
3	$(0, \pi)$
4	$(0, 0)$

Table 4.1: Coarse graining of the Brillouin zone used in the DCA $N_c = 4$ cluster of this thesis.

4.2.1 Perturbation theory for the full vertex

For the full vertex function, the lowest contributions in perturbation theory stem from the first and second order diagrams (“bubble diagrams”), which have already been introduced and discussed in subsection 3.1.1 in figures 3.2 and 3.3. The only difference is that the \vec{k} -dependent DCA Green function is used as input rather than its local counterpart and $U \rightarrow \frac{U}{N_c}$ as discussed in the previous section. For instance, one may consider the magnetic channel of the irreducible vertex² in DMFT for the case of zero bosonic frequency:

$$\Gamma_m^{\nu, \nu', \omega=0} = -U + \frac{U^2}{\beta} \sum_{\nu_1} G(\nu_1 + \nu - \nu') G(\nu_1), \quad (4.4)$$

which “translates” for the DCA case (with vanishing external momentum $q = (0, 0)$) into

$$\Gamma_m^{K, K', Q=0} = -\frac{U}{N_C} + \frac{U^2}{N_C^2 \beta} \sum_{K_1} G(K_1 + K - K') G(K_1), \quad (4.5)$$

Fig. 4.2 shows the dependence of the full vertex F up to second order perturbation theory on the generalized index K' introduced in the previous section. The external frequency and momentum is fixed to $Q = (\omega = 0, q = (0, 0))$, the first internal one is set to $K = (\nu = \frac{\pi}{\beta}, k = (0, 0))$. For the sake of readability each four points that belong to the same Matsubara frequency ν' are plotted with the same colour (alternating cyan or black). The numbers in the upper plot refer to the k -points of table 4.1 within one block, whereas the numbers in the lower one refer to the Matsubara frequencies of the blocks.

²just for an illustration due to its few contributing terms

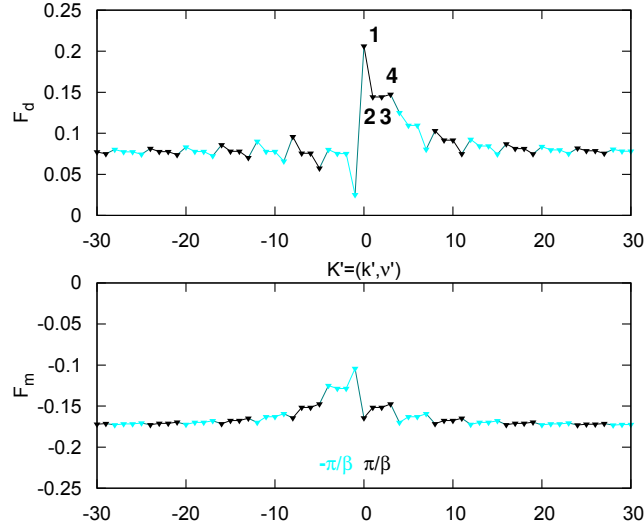


Figure 4.2: Perturbation theory up to second order (bubble diagrams) of the full vertex F at an inverse temperature of $\beta = 10.0$ and $U = 0.5$. The external frequency and momentum is fixed to $Q = (\omega = 0, q = (0, 0))$, the first internal one is set to $K = (\nu = \frac{\pi}{\beta}, k = (0, 0))$. For the sake of readability each four points that belong to the same Matsubara frequency ν' are plotted with the same colour (alternating cyan or black). The numbers 1, 2, 3 and 4 in the upper panel refer to the index of the momentum patch considered (see table 4.1) and the frequencies $\pm\pi/\beta$ in the lower panel denote the two lowest Matsubara frequencies.

One can note that despite the relatively small value of U considered, in F sizeable frequency and momentum dependent structures are present. They are more visible in the region of the two lowest Matsubara frequencies (i.e. $\nu' = \frac{\pi}{\beta}$ and $\nu' = -\frac{\pi}{\beta}$), where one observes changes also by a factor of 3 by moving from a momentum or frequency point to the next one.

4.2.2 Perturbation theory for the irreducible vertices

For the irreducible vertex function Γ_r , depending on the channel r , not all bubble diagrams shown in the figures 3.2 and 3.3 contribute, depending on their two-particle reducibility (see subsection 2.4.2). For example, if one considers Γ_d , no constant background (diagram \mathcal{P}_1 in Fig. 3.2) is present.

Fig. 4.3 shows the dependence of the four irreducible vertex channels computed in second order perturbation theory as a function of the generalized index K' . The external frequency and momentum is fixed to $Q = (\omega = 0, q = (0, 0))$, the first internal one is set to $K = (\nu = \frac{\pi}{\beta}, k = (0, 0))$. The colour conventions are chosen equally to the ones in Fig. 4.2.

Like in the case of the full vertex, one can note that there are both frequency and momentum dependence present. As in the case of the full vertex such dependencies are stronger especially in the region of the two lowest Matsubara frequencies (i.e. $\nu' = \frac{\pi}{\beta}$ and $\nu' = -\frac{\pi}{\beta}$). Quantitatively one observes that in three of the four channels ($r = m, s, t$) the overall magnitudes of the frequency

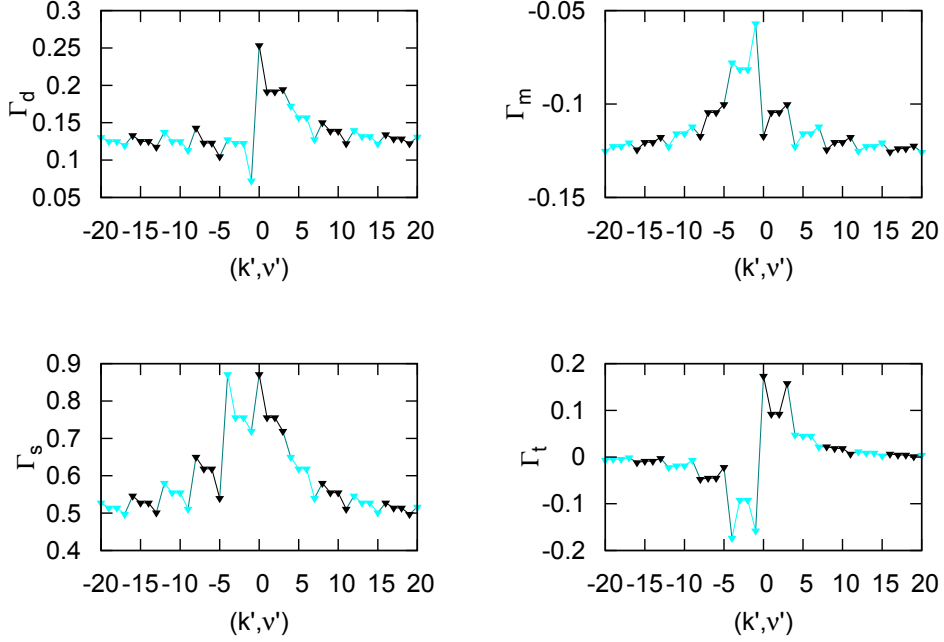


Figure 4.3: Perturbation theory up to second order (bubble diagrams) of the irreducible vertices Γ at an inverse temperature of $\beta = 10.0$ and $U = 0.5$.

and momentum dependencies are reduced with respect to the F case. Only Γ_d presents changes as a function of the frequency and momentum of the same size as those of F .

4.2.3 Perturbation theory for the fully irreducible vertex

Arriving at the deepest level of the diagrammatics and considering the fully irreducible vertex, the lowest non-vanishing diagrams of the perturbation theory (except for the pure Hubbard interaction) are of fourth order (“envelope diagrams”). Those diagrams are given for the case of the (local) $\uparrow\uparrow$ - and $\uparrow\downarrow$ -fully irreducible vertex in Fig. 4.4 (see the figure’s caption for the proper index convention for the cluster case). Fig. 4.5 shows the dependence of the fully irreducible vertex up to fourth order perturbation theory on the generalized index K' . The external frequency and momentum is fixed to $Q = (\omega = 0, q = (0, 0))$, the first internal one is set to $K = (\nu = \frac{\pi}{\beta}, k = (0, 0))$. The colour conventions are chosen equally to the ones in Fig. 4.2. One can immediately observe that the results for Λ differ significantly from those for F and Γ :

1. The overall dependencies in k and ν are strongly weakened with respect to the previous cases (e.g. Λ_d varies of about 1% in the range considered).
2. In this context, moreover, the frequency dependence evidently dominates the momentum dependence, even on the fine scale used in Fig. 4.5.

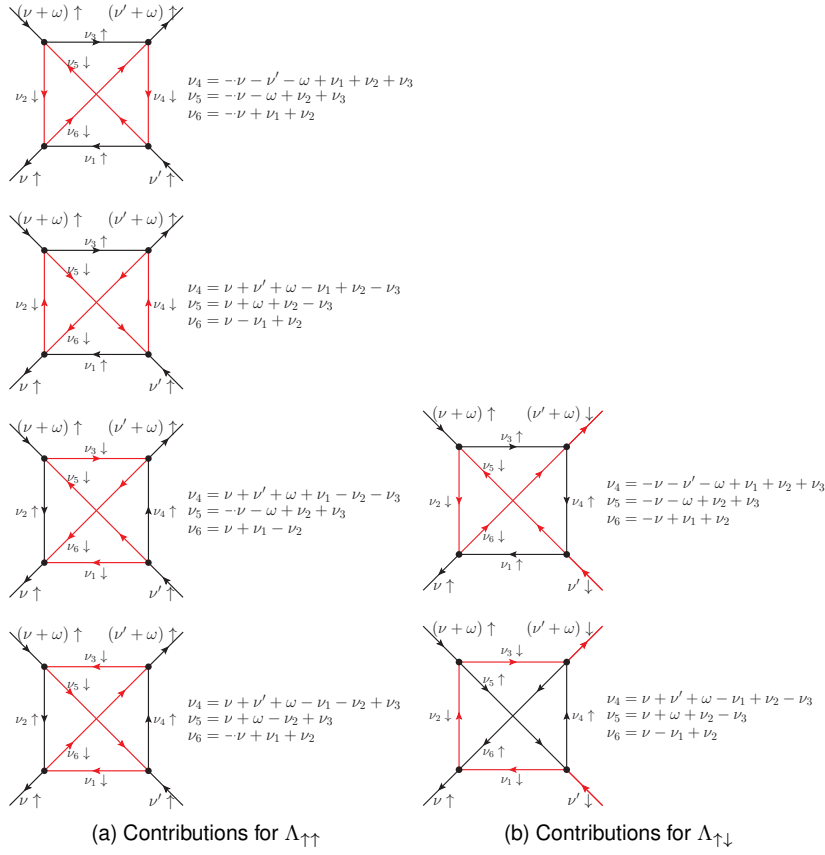


Figure 4.4: $\left(\frac{U}{N_c}\right)^4$ contributions to the perturbative expansion of the (local) fully irreducible vertex $\Lambda_{loc;\uparrow\uparrow}^{\omega,\nu,\nu'}$ (a) and $\Lambda_{loc;\uparrow\downarrow}^{\omega,\nu,\nu'}$ (b) in particle-hole notation (taken from [52]). One can transform these local quantities to momentum-dependent ones by simply applying the substitution $\nu \rightarrow K$ and $\omega \rightarrow Q$.

3. For the magnetic channel Λ_m the structure is even “softer” in comparison with the density case.

Fig. 4.5 seems to be well-behaved and considering the whole hierarchy of diagrams from F to Λ , the $D\Gamma A$ assumptions appear fully consistent with the result of perturbation theory. However, this thesis aims to understand the structure emerging also by non-perturbative calculations. These, obtained by means of the DCA, will be discussed in the following section.

4.3 Momentum dependence of two-particle quantities in DCA

The current section lies at the very heart of the $D\Gamma A$ (and, hence, of this thesis), because here, the momentum dependencies of the two-particle quantities are analysed including short-range correlations non-perturbatively using the DCA.

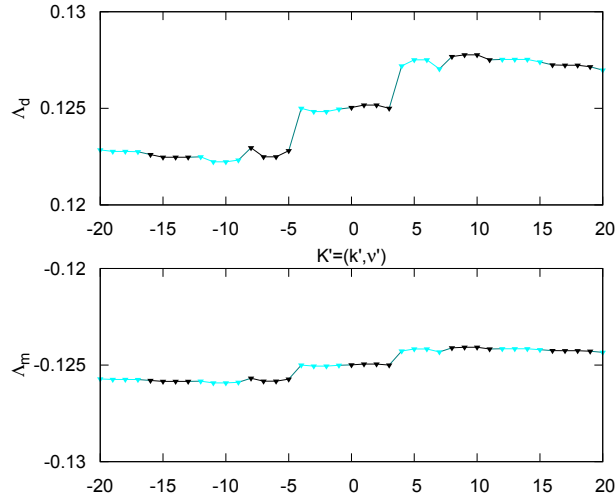


Figure 4.5: Perturbation theory of to fourth order (envelope diagrams) of the fully irreducible vertices Λ_d and Λ_m at an inverse temperature of $\beta = 10.0$ and $U = 0.5$.

In subsection 4.3.1 the weak coupling regime (i.e. $U = 0.5$) is investigated and compared to the perturbation theory results developed in section 4.2, whereas in subsection 4.3.2 results for intermediate coupling ($U = 1.0$) are presented and compared to the corresponding DMFT results. For all DCA calculations the number of cluster sites $N_c = 4$ and the points of the Brillouin zone are listed in table 4.1.

4.3.1 Weak coupling regime and comparison with perturbation theory

Full vertex F

Fig. 4.6 shows the dependences of the full vertex F in the density and magnetic channel on the combined index $K' = (k', \nu')$ obtained in DCA and the comparison to perturbation theory up to second order, at an inverse temperature of $\beta = 10.0$, $U = 0.5$ and $N_c = 4$. The bosonic combined index is fixed to $Q = (\omega = 0, q = (0, 0))$ and the first fermionic combined index is set to $K = (\nu = \frac{\pi}{\beta}, k = (0, 0))$. The solid lines with triangular points are the perturbation theory results, while the dashed lines with diamonds indicate the DCA results. For increasing the readability, the points are grouped for constant Matsubara frequencies in groups of four k -points each with alternating colours (black and cyan for the perturbation theory and magenta and green for the DCA).

Like in the perturbation theory case, also in DCA the frequency dependence of the full vertex is stronger in the low-frequency regime. The overall shapes of the DCA curves mainly agree with the perturbation theory results, which is not that surprising for the chosen weak coupling of $U = 0.5$. For high Matsubara frequencies the agreement of DCA with perturbation theory becomes

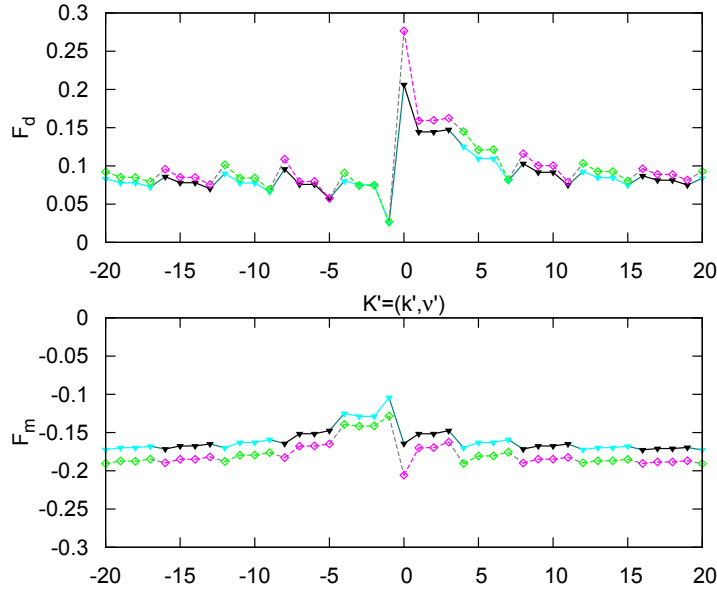


Figure 4.6: Dependences of the full vertex F in the density and magnetic channel on the combined index $K' = (k', \nu')$ respectively and the comparison to perturbation theory up to second order at an inverse temperature of $\beta = 10.0$, $U = 0.5$ and $N_c = 4$. The bosonic combined index is fixed to $Q = (\omega = 0, q = (0, 0))$ and the first fermionic combined index is set to $K = (\nu = \frac{\pi}{\beta}, k = (0, 0))$. The solid lines with triangular points are the perturbation theory results, while the dashed lines with diamonds indicate the DCA results. For increasing the readability, the points are grouped for constant Matsubara frequencies in groups of four k -points each with alternating colours (black and cyan for the perturbation theory and magenta and green for the DCA).

even more accurate than in the case of low Matsubara frequencies, a trend already observed at the DMFT level (see chapter 3 and [52]). However, here the stronger deviation from perturbation theory at low frequencies seems to affect more the frequency dependence than the momentum dependence. Finally, one can also note, that there seems to be a nearly constant shift of the magnetic channel in the DCA compared to perturbation theory, which might be understood by considering third order diagrams.

Irreducible vertices Γ

Fig. 4.7 shows the dependences of the irreducible vertices Γ on the combined index $K' = (k', \nu')$ and the comparison to perturbation theory up to second order, at an inverse temperature of $\beta = 10.0$, $U = 0.5$ and $N_c = 4$. The bosonic combined index is fixed to $Q = (\omega = 0, q = (0, 0))$ and the first fermionic combined index is set to $K = (\nu = \frac{\pi}{\beta}, k = (0, 0))$. The colour and line conventions are chosen equally to the ones in Fig. 4.6.

The overall shapes of all DCA curves mainly agree with the perturbation theory results. However, one can note that the agreement for low Matsubara frequencies of the irreducible vertex in the singlet Γ_s and in the density channel Γ_d is not as good as for the other channels. Also, the asymptotic behaviour of Γ_s is

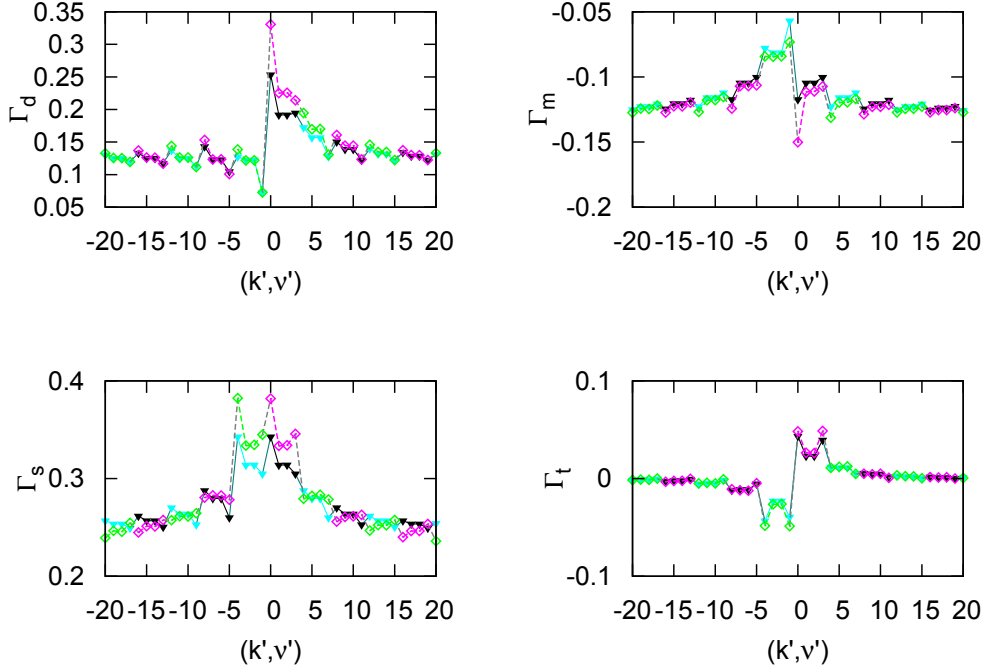


Figure 4.7: Dependences of the irreducible vertices Γ on the combined index $K' = (k', \nu')$ and the comparison to perturbation theory up to second order, for the same set of parameters as before ($\beta = 10.0$, $U = 0.5$ and $N_c = 4$). The bosonic combined index is fixed to $Q = (\omega = 0, q = (0, 0))$ and the first fermionic combined index is set to $K = (\nu = \frac{\pi}{\beta}, k = (0, 0))$. The colour and line conventions are chosen equally to the ones in Fig. 4.6.

on top of that of perturbation theory as it is for the other channels.

Fully irreducible vertex Λ

Finally, going at the deepest diagrammatic level, in fig. 4.8 the dependence of the fully irreducible vertex Λ on the combined index $K' = (k', \nu')$ and the comparison to perturbation theory up to fourth order at an inverse temperature of $\beta = 10.0$, $U = 0.5$ and $N_c = 4$ is shown. The bosonic combined index is fixed to $Q = (\omega = 0, q = (0, 0))$ and the first fermionic combined index is set to $K = (\nu = \frac{\pi}{\beta}, k = (0, 0))$. The colour and line conventions are chosen equally to the ones in Fig. 4.6. Due to the enormous numerical effort for calculating the two-particle vertices in DCA and due to the loss of frequencies when performing the frequency shifts necessary to invert the parquet equations 2.51 (see also the appendix in [52]), only the two lowest Matsubara frequencies are shown in the DCA case.

One can note that as in perturbation theory, the overall changes in the fully irreducible vertex as a function of ν and k are quite small, though one can already observe a slight enhancement with respect to perturbation theory, which is more visible in the frequency dependence. However, in contrast to the vertex

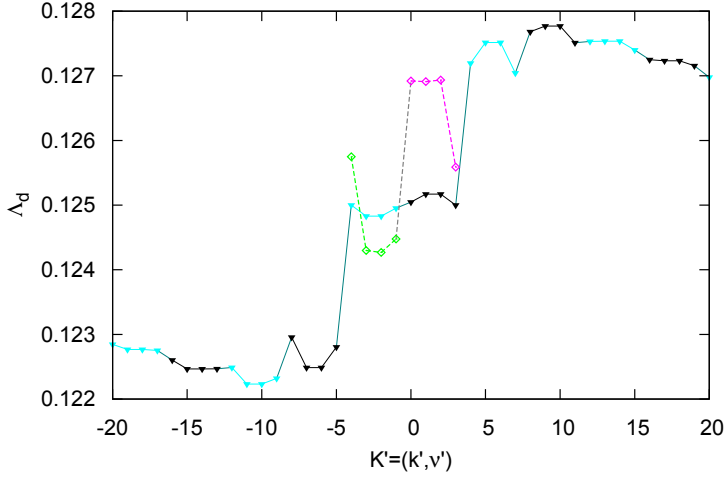


Figure 4.8: Dependence of the fully irreducible vertex Λ on the combined index $K' = (k', \nu')$ and the comparison to perturbation theory up to fourth order, at an inverse temperature of $\beta = 10.0$, $U = 0.5$ and $N_c = 4$. The bosonic combined index is fixed to $Q = (\omega = 0, q = (0, 0))$ and the first fermionic combined index is set to $K = (\nu = \frac{\pi}{\beta}, k = (0, 0))$. The colour and line conventions are chosen equally to the ones in Fig. 4.6.

quantities F and Γ , Λ additionally to its frequency dependence seems also to depend on the internal momentum to a higher extent than the other two-particle quantities do, relatively to their own frequency dependences.

4.3.2 Intermediate coupling regime and comparison with DMFT

In this subsection, the intermediate coupling $U = 1.0$ which corresponds to the same interaction level previously considered for the DCA cuprate studies [72], but now for half-filling, is presented and compared to DMFT calculations. However, for several reasons these results have to be understood as **preliminary results**:

1. The case of cluster size $N_c = 4$ is kind of a “pathological” one, because only two points of the cluster (see table 4.1) correspond to patches which include points near the Fermi surface. Furthermore, these two points are equivalent, thus not providing additional information. Clearly, this would not be the case for a cluster (like, e.g. $N_c = 8$).
2. As it turned out, the Hirsch-Fye Monte Carlo sampling especially for the Γ_s case has to be done more accurately (i.e. a finer time discretization and more frequencies) in order to achieve better asymptotics for this channel, have to be used. Due to the nature of the Bethe-Salpeter and parquet equations (Eq. 2.52 and 2.51) each channel of the irreducible vertex influences the value of the fully irreducible vertex, so that it is of

the utmost importance that **the accuracy in each channel is very high** in order to get accurate results for Λ .

3. For a better comparison of the asymptotics of the fully irreducible vertex Λ with DMFT, the amount of calculated internal frequencies has to be increased dramatically.

Keeping these facts in mind, preliminary results for $U = 1.0$ are presented here and are compared to the corresponding DMFT calculations.

Full vertex F

Fig. 4.9 shows the dependence of the full vertex F on the combined index $K' = (k', \nu')$ and the comparison to the corresponding DMFT results, at an inverse temperature of $\beta = 10.0$, $U = 1.0$ and $N_c = 4$. The bosonic combined index is fixed to $Q = (\omega = 0, q = (0, 0))$ and the first fermionic combined index is set to $K = (\nu = \frac{\pi}{\beta}, k = (0, 0))$. The solid lines with triangular points are the DMFT results, while the dashed lines with diamonds indicate the DCA data. For increasing the readability, the points are grouped for constant Matsubara frequencies in groups of four k -points each with alternating colours (red and violet for the DMFT and magenta and green for the DCA data).

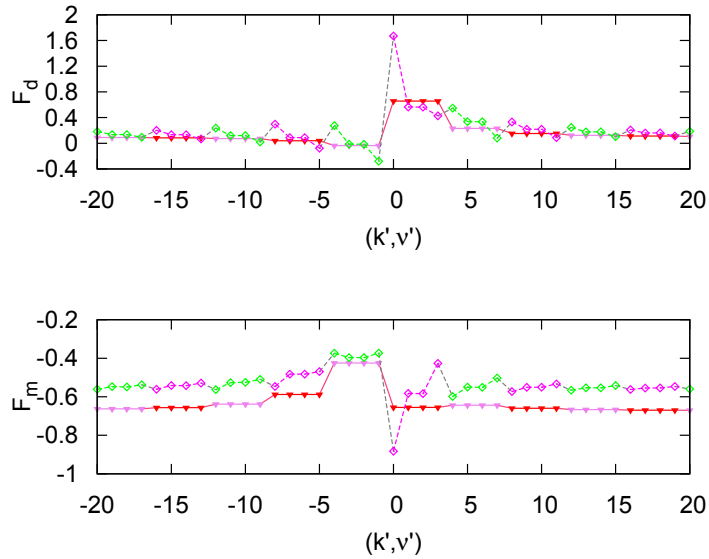


Figure 4.9: Dependence of the full vertex F on the combined index $K' = (k', \nu')$ and the comparison to the corresponding DMFT results, at an inverse temperature of $\beta = 10.0$, $U = 1.0$ and $N_c = 4$. The bosonic combined index is fixed to $Q = (\omega = 0, q = (0, 0))$ and the first fermionic combined index is set to $K = (\nu = \frac{\pi}{\beta}, k = (0, 0))$. The solid lines with triangular points are the DMFT results, while the dashed lines with diamonds indicate the DCA results. For increasing the readability, the points are grouped for constant Matsubara frequencies in groups of four k -points each with alternating colours (red and violet for the DMFT and magenta and green for the DCA data).

One can observe that the momentum dependence of the density channel compared to the frequency dependence is quite pronounced in the DCA case for low frequencies, so that big deviations from the DMFT results occur for the lowest Matsubara frequencies. On the other hand the asymptotics of DMFT and DCA results agree for the density channel. In the magnetic channel, the situation is different: for low Matsubara frequencies the DCA results do not deviate much from the DMFT results, whereas the asymptotics are less similar.

Irreducible vertices Γ

Fig. 4.10 shows the dependences of the irreducible vertices Γ on the combined index $K' = (k', \nu')$ and the comparison to the corresponding DMFT results, at an inverse temperature of $\beta = 10.0$, $U = 1.0$ and $N_c = 4$. The bosonic combined index is fixed to $Q = (\omega = 0, q = (0, 0))$ and the first fermionic combined index is set to $K = (\nu = \frac{\pi}{\beta}, k = (0, 0))$. The colour and line conventions are chosen equally to the ones in Fig. 4.9.

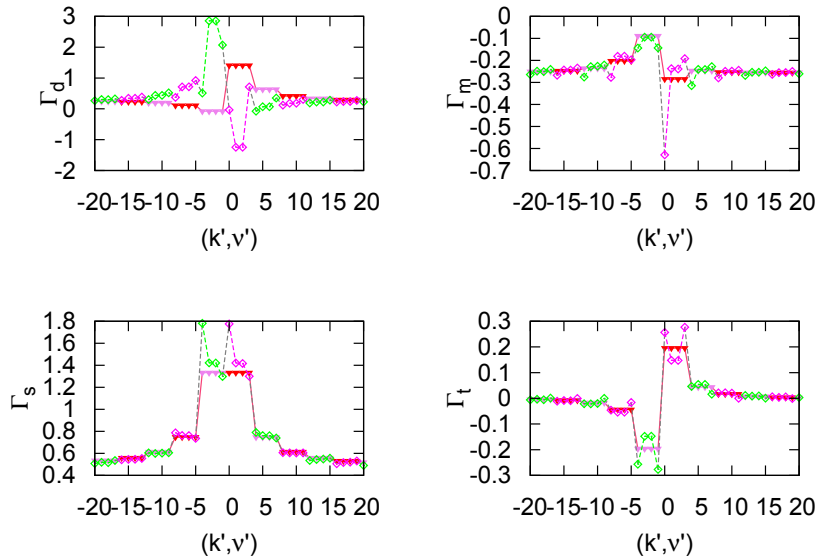


Figure 4.10: Dependences of the irreducible vertices Γ on the combined index $K' = (k', \nu')$ and the comparison to the corresponding DMFT results, at an inverse temperature of $\beta = 10.0$, $U = 1.0$ and $N_c = 4$. The bosonic combined index is fixed to $Q = (\omega = 0, q = (0, 0))$ and the first fermionic combined index is set to $K = (\nu = \frac{\pi}{\beta}, k = (0, 0))$. The colour and line conventions are chosen equally to the ones in Fig. 4.9.

Like in the case of the full vertex, when comparing DCA and DMFT results for the irreducible vertex, one has to distinguish between the different channels. While in the particle-particle channels Γ_s and Γ_t and the magnetic channel Γ_m only quantitative deviations of the dependencies on the combined index occur for the lowest Matsubara frequencies, for the density channel Γ_d also exists a qualitative difference between DMFT and DCA results for low frequencies. In fact, one observes a **change of sign** of the irreducible vertex in the density

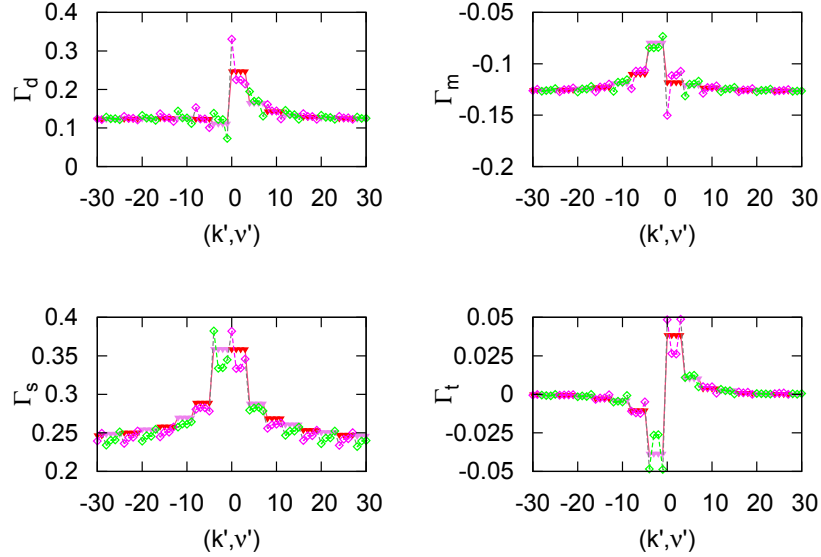


Figure 4.11: Same plot as in fig. 4.10, but for $U = 0.5$. One can see that the irreducible vertex in the density channel Γ_d has the same sign in DCA like in DMFT for this interaction value.

channel in DCA compared to DMFT. As for the interpretation, then, it is quite natural to make a connection to the discussion in subsection 3.2.2, where it has been shown that the low-frequency structures of the local irreducible vertex in the density channel changed their signs for an inverse temperature of $\beta = 10.0$ and $U = 1.275$. One may hence plausibly suppose that the inclusion of non-local correlations via the DCA can shift the instability line for the vertex Γ_d (shown in the phase diagram 3.13) towards the weakly correlated side. This idea is well-grounded, because if one calculates the eigenvalues of the corresponding susceptibility χ_d one can see that for $U = 0.5$ all eigenvalues are positive, whereas one of them (exactly as it happened in DMFT for larger U , see Fig. 3.12) changed sign until arriving at $U = 1.0$. For illustrating this behaviour, fig. 4.11 shows the same plots as fig. 4.10, but now for an interaction value of $U = 0.5$. One can see that at this U value, the structure of the DCA results still qualitatively resembles that of the DMFT ones in every channel (including the density one).

Fully irreducible vertex Λ

As one can easily imagine from the data for the irreducible vertices Γ , if only one Γ (in this case Γ_d), becomes strongly frequency- and momentum-dependent, this will also affect the results for the fully irreducible vertex Λ . Fig. 4.12 shows that this is indeed the case (here the same set of parameters is used as for the full vertex F). The colour and line conventions are chosen equally to the ones in Fig. 4.9.

Due to the structure of the Bethe-Salpeter and parquet equations (2.52 and

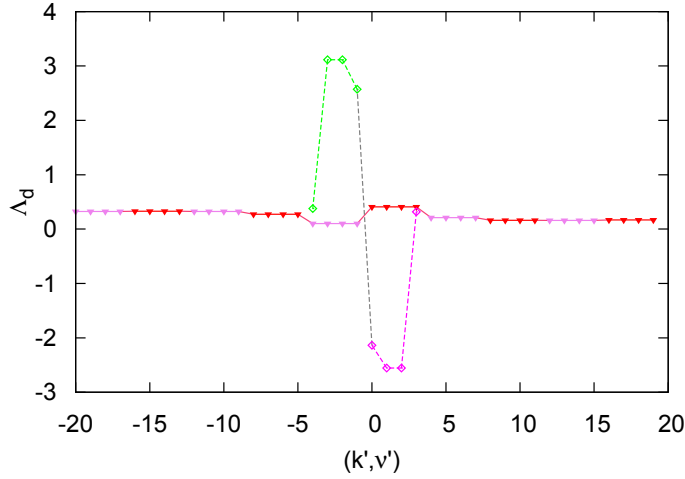


Figure 4.12: Dependence of the fully irreducible vertex Λ on the combined index $K' = (k', \nu')$ and the comparison to the corresponding DMFT results, at an inverse temperature of $\beta = 10.0$, $U = 1.0$ and $N_c = 4$. The bosonic combined index is fixed to $Q = (\omega = 0, q = (0, 0))$ and the first fermionic combined index is set to $K = (\nu = \frac{\pi}{\beta}, k = (0, 0))$. The colour and line conventions are chosen equally to the ones in Fig. 4.9.

2.51), the enhancement of Γ_d stemming from the transition discussed in subsection 3.2.2 immediately affects the fully irreducible vertex Λ , so that this quantity in DCA heavily differs from the corresponding local one in DMFT. Especially, the sign of the two lowest Matsubara frequencies in the DCA results shown Fig. 4.9 differ from the DMFT ones. While strong enhancement of the frequency dependence of the fully irreducible vertex calculated in DCA (Λ_{DCA}) would still be compatible with the D Γ A hypothesis, the equally strong k -dependence appearing in Fig. 4.12 would limit the applicability of D Γ A in the exactly half-filled region. Further calculations and tests, however, are needed to verify this, especially with larger N_c as mentioned in the beginning of this subsection.

4.4 Summary of the non-local results

To recapitulate, in this chapter DCA calculations have been performed for both the weak and the intermediate coupling regime. For the weak coupling regime, the qualitative behaviour of the vertex quantities at every vertex level can, in principle, be predicted by perturbation theory, although slight deviations already occur for the magnetic channel of the full vertex F and the singlet channel of the irreducible vertex Γ . When analysing the fully irreducible vertex Λ , the DCA data display a negligible momentum dependence (in any case smaller than the frequency dependence) in full accordance with the D Γ A assumptions.

By considering the intermediate coupling regime, however, one can note that

the low-frequency structures of the irreducible vertex Γ_d are strongly enhanced analogously to those for its corresponding local quantity (described in subsection 3.2.2), even at a lower value of the interaction U . These enhanced low-frequency and momentum dependences of Γ_d , via the Bethe-Salpeter equations, reflect themselves in an enhanced frequency and momentum dependent structure of Λ . The comparison to DMFT has been performed at this coupling level, also revealed a qualitatively similar behaviour to the DCA results, except for Γ_d and, consequently, the fully irreducible vertex.

Chapter 5

Conclusions and outlook

The theoretical investigation of two-particle vertex functions of correlated electrons is a very challenging but valuable task. The computation of these quantities not only allows for a much more complete comparison between theory and experiments, but those quantities also serve as an essential input for diagrammatic extensions of the well-known DMFT, such as D Γ A and the dual fermion approach. Hitherto, the vertex quantities have been investigated rather sporadically in the literature, and therefore, a systematic analysis has been provided by this thesis, in which the analysis of both local and non-local vertices has been conducted and has led to quite interesting and, to some extent, surprising results.

Concerning the local physics of the Hubbard model, our DMFT calculations of two-particle quantities have shown the occurrence of first precursors of the Mott-Hubbard transition well inside the metallic phase in the form of low-frequency divergences of the irreducible vertex in the density channel Γ_d and, correspondingly, of the fully irreducible vertex Λ . Those divergencies seem very puzzling, because at the instability line the corresponding thermodynamic local (charge) susceptibility remains finite. Future research has to resolve the physical interpretation of this robust numerical result, on which this thesis started to shed light. Especially, those investigations have to clarify how these divergences can be related to non-equilibrium phenomena in the Hubbard model or kinks in the electronic self-energy and specific heat, which are observed in the very same parameter region in the low and intermediate temperature regime.

Finally, including the effect of non-local spatial correlations, at least within the cluster size of the DCA, in the last part of this thesis preliminary results for the non-local two-particle quantities on a four-site cluster for the two-dimensional half-filled Hubbard model have been presented. In the case of weak coupling, all vertex functions seem to be well-behaved and their frequency dependences dominates their momentum dependences, which also means, that the assumption of D Γ A is well fulfilled for this interaction region. On the other hand, the first data available for the intermediate coupling regime seem to indicate that significant and equally important effects of local and non-local spatial correlation may occur even in the fully irreducible vertex, which would be problematic for the standard D Γ A assumptions in this parameter regime. While further numer-

ical testing is necessary, because the case of a four-site cluster is a somehow “pathological” one, and its size has to be increased (e.g. at least to an eight-site cluster), the algorithm for calculating the irreducible vertex in the singlet channel Γ_s requires further improvement, and more Matsubara frequencies have to be included, in general, one can note here, that this strong momentum dependencies seem to be associated to a similar instability line of Γ_d , observed already at the DMFT level: This instability line, however, is probably shifted towards the region of weak coupling by the inclusion of non-local spatial correlations.

The present results evidently call for further precise numerical investigations of the effects of non-local spatial correlations on (divergent) precursors of the Mott transition present in the phase diagram of the Hubbard model in two and three dimensions.

List of Figures

1.1	Correlation in every day's life	4
1.2	MIT in V_2O_3	5
1.3	DMFT phase diagram showing the MIT of the two-dimensional half-filled Hubbard model	6
1.4	Hubbard model	8
2.1	Physical interpretation of the one-particle Green function	13
2.2	Feynman diagram of the non-interacting Green function	14
2.3	One-particle irreducibility	14
2.4	Diagrammatic representation of the Dyson equation	14
2.5	Geometry and spectral function of an ARPES experiment	15
2.6	Diagrammatic content of the DMFT	18
2.7	Self-consistency cycle of the DMFT	20
2.8	Illustration of the MIT in DMFT	23
2.9	Coarse graining cells in DCA	24
2.10	Diagrammatic content of the DCA	25
2.11	Particle-hole and particle-particle notation convention	27
2.12	General susceptibility	28
2.13	Parquet equation	29
3.1	Frequency dependence of the local full vertex function	34
3.2	Lowest order perturbation diagrams for $F_{\uparrow\uparrow}$	35
3.3	Lowest order perturbation diagrams for $F_{\uparrow\downarrow}$	35
3.4	Frequency dependence of the local irreducible vertex functions	36
3.5	Frequency dependence of the local fully irreducible vertex functions	37
3.6	ED-QMC comparison of the local general susceptibility	38
3.7	ED-QMC comparison of the local irreducible vertices	39
3.8	ED-QMC comparison of the local fully irreducible vertices	39
3.9	Enhancement of the main diagonal elements of the local density vertex F_d when approaching the MIT	40
3.10	Enhancement of the local spin susceptibility	42
3.11	Density plots of the development of the local irreducible vertex in the density channel	43
3.12	Phase diagram of the divergencies of the local irreducible vertices	44
3.13	Phase diagram of the divergencies of the local irreducible vertices with extrapolation into the atomic limit	47
3.14	Evolution of the eigenvector $E_{\lambda=0,d}^\nu$	48

3.15	Spectral functions for the hypercubic Hubbard model in NRG . . .	49
3.16	Momentum distribution $n(\epsilon, t)$ after an interaction quench in the half-filled Hubbard model	52
3.17	Enhancement of the local fully irreducible vertex Λ_d^{loc} when approaching the divergence of Γ_d^{loc}	53
4.1	Momentum dependence of the fully irreducible vertex Λ as a function of the momentum transfer taken from [72]	56
4.2	Perturbation theory up to second order of the full vertex F at an inverse temperature of $\beta = 10.0$ and $U = 0.5$	59
4.3	Perturbation theory up to second order of the irreducible vertices Γ at an inverse temperature of $\beta = 10.0$ and $U = 0.5$	60
4.4	$\left(\frac{U}{N_c}\right)^4$ contributions to the perturbative expansion of the (local) fully irreducible vertex $\Lambda_{loc;\uparrow\uparrow}^{\omega,\nu,\nu'}$ (a) and $\Lambda_{loc;\uparrow\uparrow}^{\omega,\nu,\nu'}$ (b) in particle-hole notation (taken from [52]).	61
4.5	Perturbation theory up to fourth order of the fully irreducible vertices Λ_d and Λ_m at an inverse temperature of $\beta = 10.0$ and $U = 0.5$	62
4.6	Full vertex F at an inverse temperature of $\beta = 10.0$ and $U = 0.5$ and $N_c = 4$	63
4.7	Irreducible vertices Γ at an inverse temperature of $\beta = 10.0$ and $U = 0.5$ and $N_c = 4$	64
4.8	Fully irreducible vertex Λ at an inverse temperature of $\beta = 10.0$ and $U = 0.5$ and $N_c = 4$	65
4.9	Full vertex F at an inverse temperature of $\beta = 10.0$ and $U = 1.0$ and $N_c = 4$	66
4.10	Irreducible vertices Γ at an inverse temperature of $\beta = 10.0$ and $U = 1.0$ and $N_c = 4$	67
4.11	Irreducible vertices Γ at an inverse temperature of $\beta = 10.0$ and $U = 0.5$ and $N_c = 4$	68
4.12	Fully irreducible vertex Λ at an inverse temperature of $\beta = 10.0$ and $U = 1.0$ and $N_c = 4$	69

List of Tables

2.1	Diagrammatic approximations at different vertex levels	30
4.1	Coarse graining of the Brillouin zone used in the DCA $N_c = 4$ cluster of this thesis.	58

Bibliography

- [1] H.D. Zeh. *The Physical Basis of the Direction of Time*. The Frontiers Collection. Springer London, Limited, 2007.
- [2] P. Coleman. *Introduction to Many Body Physics*. Cambridge University Press, 2008.
- [3] P. W. Anderson. More is different. *Science*, 177(4047):393–396, 1972.
- [4] N. F. Mott. Metal-insulator transition. *Rev. Mod. Phys.*, 40:677–683, Oct 1968.
- [5] D. B. McWhan, A. Menth, J. P. Remeika, W. F. Brinkman, and T. M. Rice. Metal-insulator transitions in pure and doped v_2O_3 . *Phys. Rev. B*, 7:1920–1931, Mar 1973.
- [6] D. B. McWhan, T. M. Rice, and J. P. Remeika. Mott transition in cr-doped v_2O_3 . *Phys. Rev. Lett.*, 23:1384–1387, Dec 1969.
- [7] J. G. Bednorz and K. A. Müller. Untitled. *Z. Phys. B*, 64:189, 1986.
- [8] Hironari Okada, Yuki Takahashi, Kazumi Igawa, Kazunobu Arii, Hiroki Takahashi, Takumi Watanabe, Hiroshi Yanagi, Yoichi Kamihara, Toshio Kamiya, Masahiro Hirano, Hideo Hosono, Satoshi Nakano, and Takumi Kikegawa. Pressure effects on superconducting and structural properties for nickel-based superconductors $lanixO$ ($x = p$ and as). *Journal of the Physical Society of Japan*, 77SC(Supplement C):119–120, 2008.
- [9] S. Paschen, T. Luhmann, S. Wirth, P. Gegenwart, O. Trovarelli, C. Geibel, F. Steglich, P. Coleman, and Qimiao Si. Hall-effect evolution across a heavy-fermion quantum critical point. 2004.
- [10] J. Custers, P. Gegenwart, H. Wilhelm, K. Neumaier, Y. Tokiwa, O. Trovarelli, C. Geibel, F. Steglich, C. Pepin, and P. Coleman. The break-up of heavy electrons at a quantum critical point. *Nature*, 424(6948):524–527, July 2003.
- [11] R. von Helmolt, J. Wecker, B. Holzapfel, L. Schultz, and K. Samwer. Giant negative magnetoresistance in perovskitelike $la_{2/3}ba_{1/3}mno_x$ ferromagnetic films. *Phys. Rev. Lett.*, 71:2331–2333, Oct 1993.
- [12] R.M. Kusters, J. Singleton, D.A. Keen, R. McGreevy, and W. Hayes. Magnetoresistance measurements on the magnetic semiconductor $nd_{0.5}pb_{0.5}mno_3$. *Physica B: Condensed Matter*, 155:362 – 365, 1989.

- [13] © HTU / Martin Borer. Dancefloor of the hofburg, tu-ball 2009.
- [14] Antoine Georges. Strongly correlated electron materials: Dynamical mean-field theory and electronic structure. *AIP Conference Proceedings*, 715(1):3–74, 2004.
- [15] A. Toschi. *Strong Electronic Correlation in Dynamical Mean Filed Theory and beyond*. Habilitationsschrift, Vienna University of Technology, 2012.
- [16] Masatoshi Imada, Atsushi Fujimori, and Yoshinori Tokura. Metal-insulator transitions. *Rev. Mod. Phys.*, 70:1039–1263, Oct 1998.
- [17] N. Bluemer. *Mott-Hubbard Metal-Insulator Transition and Optical Conductivity in High Dimensions*. PhD thesis, 2002.
- [18] A. Altland and B. Simons. *Condensed Matter Field Theory*. Cambridge University Press, 2006.
- [19] J. Hubbard. Electron correlations in narrow energy bands. *Proc. R. Soc. London, Ser. A*, 276(1365):238–257, 1963.
- [20] Martin C. Gutzwiller. Effect of correlation on the ferromagnetism of transition metals. *Phys. Rev. Lett.*, 10:159–162, Mar 1963.
- [21] Junjiro Kanamori. Electron correlation and ferromagnetism of transition metals. *Progress of Theoretical Physics*, 30(3):275–289, 1963.
- [22] A. Toschi: Mastering the electronic correlations: a challenge for the contemporary physics. Tenure Track Talk. Vienna 2012.
- [23] R. O. Jones and O. Gunnarsson. The density functional formalism, its applications and prospects. *Rev. Mod. Phys.*, 61:689–746, Jul 1989.
- [24] A.M. Zagoskin. *Quantum Theory of Many-Body Systems: Techniques and Applications*. Graduate Texts in Contemporary Physics Series. Springer-Verlag GmbH, 1998.
- [25] G.D. Mahan. *Many Particle Physics*. Physics of Solids and Liquids. Springer, 2000.
- [26] A.A. Abrikosov, L.P. Gorkov, I.E. Dzyaloshinski, and R.A. Silverman. *Methods of Quantum Field Theory in Statistical Physics*. Dover Books on Physics. Dover Publications, 1975.
- [27] Andrea Damascelli, Zahid Hussain, and Zhi-Xun Shen. Angle-resolved photoemission studies of the cuprate superconductors. *Rev. Mod. Phys.*, 75:473–541, Apr 2003.
- [28] F. Mandl and G. Shaw. *Quantum Field Theory*. A Wiley-Interscience publication. John Wiley & Sons, 2010.
- [29] Lode Pollet, Nikolay V. Prokof'ev, and Boris V. Svistunov. Regularization of diagrammatic series with zero convergence radius. *Phys. Rev. Lett.*, 105:210601, Nov 2010.

- [30] Antoine Georges and Gabriel Kotliar. Hubbard model in infinite dimensions. *Phys. Rev. B*, 45:6479–6483, Mar 1992.
- [31] Walter Metzner and Dieter Vollhardt. Correlated lattice fermions in $d=\infty$ dimensions. *Phys. Rev. Lett.*, 62:324–327, Jan 1989.
- [32] K. Held. Electronic structure calculations using dynamical mean field theory. *Advances in Physics*, 56(6):829–926, 2007.
- [33] Thomas Schaefer and Georg Rohringer et al. Electronic correlation at the two-particle level, DPG conference poster, 2012.
- [34] Ralf Bulla, Theo A. Costi, and Thomas Pruschke. Numerical renormalization group method for quantum impurity systems. *Rev. Mod. Phys.*, 80:395–450, Apr 2008.
- [35] E. Müller-Hartmann. The hubbard model at high dimensions: some exact results and weak coupling theory. *Zeitschrift für Physik B Condensed Matter*, 76:211–217, 1989.
- [36] J. E. Hirsch and R. M. Fye. Monte carlo method for magnetic impurities in metals. *Phys. Rev. Lett.*, 56:2521–2524, Jun 1986.
- [37] R. M. Fye and J. E. Hirsch. Monte carlo study of the symmetric anderson-impurity model. *Phys. Rev. B*, 38:433–441, Jul 1988.
- [38] M. Jarrell, Th. Maier, C. Huscroft, and S. Moukouri. Quantum monte carlo algorithm for nonlocal corrections to the dynamical mean-field approximation. *Phys. Rev. B*, 64:195130, Oct 2001.
- [39] Masuo Suzuki. Relationship between d -dimensional quantal spin systems and $(d + 1)$ -dimensional ising systems. *Progress of Theoretical Physics*, 56(5):1454–1469, 1976.
- [40] Emanuel Gull, Andrew J. Millis, Alexander I. Lichtenstein, Alexey N. Rubtsov, Matthias Troyer, and Philipp Werner. Continuous-time monte carlo methods for quantum impurity models. *Rev. Mod. Phys.*, 83:349–404, May 2011.
- [41] Nicolaus Parragh, Alessandro Toschi, Karsten Held, and Giorgio Sangiovanni. Conserved quantities of $su(2)$ -invariant interactions for correlated fermions and the advantages for quantum monte carlo simulations. *Phys. Rev. B*, 86:155158, Oct 2012.
- [42] P. W. Anderson. *The future lies ahead*, chapter 4, pages 27–30.
- [43] G. Kotliar and D. Vollhardt. Strongly correlated materials: Insights from dynamical mean-field theory. *Physics Today*, 57:53, Mar 2004.
- [44] Thomas Maier, Mark Jarrell, Thomas Pruschke, and Matthias H. Hettler. Quantum cluster theories. *Rev. Mod. Phys.*, 77:1027–1080, Oct 2005.
- [45] M. Jarrell and A. Macridin. Dynamical mean field and dynamical cluster approximation, 2011.

- [46] A. Toschi, A. A. Katanin, and K. Held. Dynamical vertex approximation: A step beyond dynamical mean-field theory. *Phys. Rev. B*, 75:045118, Jan 2007.
- [47] A. A. Katanin, A. Toschi, and K. Held. Comparing pertinent effects of antiferromagnetic fluctuations in the two- and three-dimensional hubbard model. *Phys. Rev. B*, 80:075104, Aug 2009.
- [48] A. N. Rubtsov, M. I. Katsnelson, and A. I. Lichtenstein. Dual fermion approach to nonlocal correlations in the hubbard model. *Phys. Rev. B*, 77:033101, Janf 2008.
- [49] A. N. Rubtsov, M. I. Katsnelson, A. I. Lichtenstein, and A. Georges. Dual fermion approach to the two-dimensional hubbard model: Antiferromagnetic fluctuations and fermi arcs. *Phys. Rev. B*, 79:045133, Jan 2009.
- [50] H. Park. *The study of two-particle response functions in strongly correlated electron systems within the dynamical mean field theory*. PhD thesis, 2011.
- [51] Nan Lin, Emanuel Gull, and Andrew J. Millis. Two-particle response in cluster dynamical mean-field theory: Formalism and application to the raman response of high-temperature superconductors. *Phys. Rev. Lett.*, 109:106401, Sep 2012.
- [52] G. Rohringer, A. Valli, and A. Toschi. Local electronic correlation at the two-particle level. *Phys. Rev. B*, 86:125114, Sep 2012.
- [53] G. Rohringer. *in preparation*. PhD thesis, 2013.
- [54] N. E. Bickers, D. J. Scalapino, and S. R. White. Conserving approximations for strongly correlated electron systems: Bethe-salpeter equation and dynamics for the two-dimensional hubbard model. *Phys. Rev. Lett.*, 62:961–964, Feb 1989.
- [55] J. J. Deisz, D. W. Hess, and J. W. Serene. Incipient antiferromagnetism and low-energy excitations in the half-filled two-dimensional hubbard model. *Phys. Rev. Lett.*, 76:1312–1315, Feb 1996.
- [56] G. Rohringer, A. Toschi, A. Katanin, and K. Held. Critical properties of the half-filled hubbard model in three dimensions. *Phys. Rev. Lett.*, 107:256402, Dec 2011.
- [57] V. Janiš. Stability of self-consistent solutions for the hubbard model at intermediate and strong coupling. *Phys. Rev. B*, 60:11345–11360, Oct 1999.
- [58] S. X. Yang, H. Fotsos, J. Liu, T. A. Maier, K. Tomko, E. F. D’Azevedo, R. T. Scalettar, T. Pruschke, and M. Jarrell. Parquet approximation for the 4×4 hubbard cluster. *Phys. Rev. E*, 80:046706, Oct 2009.
- [59] M. J. Rozenberg, G. Kotliar, and X. Y. Zhang. Mott-hubbard transition in infinite dimensions. ii. *Phys. Rev. B*, 49:10181–10193, Apr 1994.

- [60] Antoine Georges, Gabriel Kotliar, Werner Krauth, and Marcelo J. Rozenberg. Dynamical mean-field theory of strongly correlated fermion systems and the limit of infinite dimensions. *Rev. Mod. Phys.*, 68:13–125, Jan 1996.
- [61] S. X. Yang, H. Fotso, H. Hafermann, K. M. Tam, J. Moreno, T. Pruschke, and M. Jarrell. Dual fermion dynamical cluster approach for strongly correlated systems. *arXiv*, 1104.3854v1, 2011.
- [62] H. Hafermann, C. Jung, S. Brener, M. I. Katsnelson, A. N. Rubtsov, and A. I. Lichtenstein. Superperturbation solver for quantum impurity models. *EPL (Europhysics Letters)*, 85(2):27007, 2009.
- [63] T. Schaefer, G. Rohringer, K. Held, O. Gunnarsson, S. Ciuchi, G. Sangiovanni, and A. Toschi. Divergent precursors of the mott-hubbard transition at the two-particle level, in preparation.
- [64] R. Zitzler. *Magnetic properties of the one-band Hubbard model*. PhD thesis, 2004.
- [65] Martin Eckstein, Marcus Kollar, and Philipp Werner. Interaction quench in the hubbard model: Relaxation of the spectral function and the optical conductivity. *Phys. Rev. B*, 81:115131, Mar 2010.
- [66] K. Held Y.-F. Yang I.A. Nekrasov Th. Pruschke K. Byczuk, M. Kollar and D. Vollhardt. Kinks in the dispersion of strongly correlated electrons. *Nat. Phys.*, 3:168.
- [67] A. Toschi, M. Capone, C. Castellani, and K. Held. Kinks in the electronic specific heat. *Phys. Rev. Lett.*, 102:076402, Feb 2009.
- [68] L. M. Falicov and J. C. Kimball. Simple model for semiconductor-metal transitions: Smb_6 and transition-metal oxides. *Phys. Rev. Lett.*, 22:997–999, May 1969.
- [69] J. K. Freericks and V. Zlatić. Exact dynamical mean-field theory of the falicov-kimball model. *Rev. Mod. Phys.*, 75:1333–1382, Oct 2003.
- [70] Martin Eckstein, Marcus Kollar, and Philipp Werner. Thermalization after an interaction quench in the hubbard model. *Phys. Rev. Lett.*, 103:056403, Jul 2009.
- [71] D. Luitz. PhD thesis, submitted in November 2012.
- [72] T. A. Maier, M. S. Jarrell, and D. J. Scalapino. Structure of the pairing interaction in the two-dimensional hubbard model. *Phys. Rev. Lett.*, 96:047005, Feb 2006.
- [73] D. Sénéchal, A.M. Tremblay, and C. Bourbonnais. *Theoretical Methods for Strongly Correlated Electrons*. CRM Series in Mathematical Physics. Springer, 2003.

Index

- Anderson impurity model, 17
- Bethe-Salpeter equation, 28
- bubble term, 27
- channels
 - of two-particle quantities, 29
- correlation, 3
 - spatial correlation, 3
 - time correlation, 3
- DΓA, 25
- DCA, 24
- divergency
 - irreducible vertex, 41
 - phase diagram for irreducible vertex, 44
 - spin susceptibility, 40
- DMFT, 17
 - CTQMC, 22
 - DCA, 24
 - ED, 19
 - extensions, 25
 - Hirsch-Fye QMC, 20
 - limitations, 22
 - non-equilibrium, 51
 - self-consistency cycle, 19
- Dual fermion approach, 26
- emergent phenomena, 2
- Feynman diagrams, 14
- Full vertex
 - DCA(QMC) results, 62
 - definition, 27
 - DMFT(ED) results, 34
 - DMFT(QMC) results, 38
 - non-local perturbation theory, 58
- Fully irreducible vertex
 - DCA(QMC) results, 64
 - definition, 28
 - DMFT(ED) results, 36
 - DMFT(QMC) results, 38
 - non-local perturbation theory, 60
- Green function
 - interacting, 15
 - non-interacting, 13
 - one-particle, 12
 - two-particle, 26
- hopping amplitude, 7
- Hubbard interaction, 8
- Hubbard model, 7
- imaginary times, 12
- Irreducible vertex
 - DCA(QMC) results, 63
 - definition, 29
 - DMFT(ED) results, 36
 - DMFT(QMC) results, 38
 - non-local perturbation theory, 59
- model Hamiltonians, 7
- Mott-Hubbard transition, 5
 - V_2O_3 , 4
 - phase diagram, 5
- parquet equation, 28
- quasiparticles, 16
- reducibility
 - one-particle, 14
 - two-particle, 28
- self-energy, 14
- spectral function, 15
- spin-dependence, 29
- susceptibility, 26
- tight binding approximation, 7
- vertex approximations, 30
- vertex corrections, 27
- Wannier states, 7